Development of Pseudopotential-Based LBM Solver to Explore the Microdynamics of Liquid-Vapor Phase Change Processes

A thesis submitted in partial fulfillment of the requirements for the degree of

Doctor of Philosophy

by

Aritra Mukherjee

Under the supervision of

Dr. Dipankar N. Basu

and

Dr. Pranab K. Mondal

Department of Mechanical Engineering
Indian Institute of Technology Guwahati
August 2022


Indian Institute of Technology Guwahati

CERTIFICATE

It is certified that the work contained in this thesis entitled "*Development of Pseudopotential-Based LBM Solver to Explore the Microdynamics of Liquid-Vapor Phase Change Processes*" by Aritra Mukherjee, has been carried out under our supervision and this work has not been submitted elsewhere for a degree.

August, 2022

(Dr. Dipankar N.Basu)

Associate Professor

Department of Mechanical Engineering

Indian Institute of Technology Guwahati

(Dr. Pranab K.Mondal)

Associate Professor

Department of Mechanical Engineering

Indian Institute of Technology Guwahati

Signature of Thesis Examiner

(Dr. B. S. V. Prasad Patnaik)

Professor

Department of Applied Mechanics

Indian Institute of Technology Madras

Abstract

The pseudopotential-based LB multiphase model has enormous potential in the simulation of phase-change heat transfer problems. It facilitates the natural development and migration of interfaces during the multiphase simulation as well as saves a lot of computational time. Along with these, this model enjoys several advantages like simple implementation procedure, excellent parallelizability, and easy applicability in complex domains. Due to these superiorities, it is becoming increasingly popular among researchers working on numerical simulation of multiphase flow. A pseudopotential model based thermal multiphase flow solver is developed as this thesis work, which is employed in several phase change heat transfer problems related to boiling and condensation.

The first problem successfully explores the capability of the pseudopotential-based thermal lattice Boltzmann model in emulating the underlying thermohydrodynamics of subcooled flow boiling in a narrow fluidic horizontal channel in detail. A two-dimensional rectangular channel with specified inlet temperature and flow rate, and exit pressure, housing a microheater at the bottom wall, is considered as the computational domain of interest. Adopted boundary conditions ensure subcooled flow boiling through the channel. The complete dynamics of bubble ebullition at the nucleation site, and subsequent flow regimes are adequately reproduced. Both bubbly and slug flow patterns are illustrated through the temporal evolution of the interface, and associated pressure drop and heat transport characteristics. Dependence of the departure characteristics on the flow rate, wall superheat and surface wettability is found to be consistent with available literature, which substantiates the competence of the present algorithm.

The next study uses the multiple-relaxation time based LB model to explore the role of surface morphology and cold spot temperature in determining the visual state of the condensate droplet, mode of nucleation and associated rates of energy and mass interactions in temperature controlled condensation process. Such a study is scarcely found in the available literature. A rectangular domain filled with saturated vapor, housing a cold spot on the bottom rough surface is considered, where the bottom surface has rectangular nanopillars to mimic a rough surface. Gradual increase in the spacing modifies the nucleation mode from top through side to bottom, while the droplet changes from Cassie to Wenzel state. A couple of phase diagrams have been developed to study the combined effect of pillar dimensions on Cassie and Wenzel drop formation. One important novelty of the present study is the consideration is non-

isothermal condition within LB structure. Enhancement in the degree of subcooling at the cold spot encourages greater condensation and Cassie-to-Wenzel transition.

The same numerical framework is employed to study condensate droplet formation and movement on a microstructured surface, which has not yet been studied using LBM. Two vertical surfaces protruded with rectangular micropillars with disparate dimensions are considered for this purpose. The rectangular domain is assumed to be filled with saturated vapor initially and three separate cold spots are assumed on the cold bottom wall as nucleation sites. Condensate droplet, growth, coalescence, and movement is studied in detail through sequential temporal snapshots. It is observed that closely packed taller columns promote dropwise condensation having high heat transfer rate. Six different surface inclinations are considered to study the effect of gravitational force on condensation, which shows that a vertical surface has highest mass condensation rate and heat transfer rate due to maximum downward gravitational force.

Being motivated by the prime weakness of the pseudopotential based thermal LB model about its incapability of simulating boiling problems with a large density ratio, the last work of this thesis focuses on augmentation of the basic pseudopotential based thermal multiphase algorithm by enhancing the isotropy of the discrete equation and thermodynamic consistency of the overall formulation, to expedite simulation of pool boiling at higher-density ratios. Accordingly, modification is suggested in the discrete form of the updated interparticle interaction term, by expanding the discretization to the eighth order. The proposed amendment is successful in substantially reducing the spurious velocity in the vicinity of a static droplet, while allowing stable simulation at a much higher-density ratio under identical conditions, which is a noteworthy improvement over existing Single Relaxation Time (SRT)-LBM algorithms. Various pool boiling scenarios have been explored for a reduced temperature of 0.75, which itself is significantly lower than reported in comparable literature, in both rectangular and cylindrical domains, and also with micro- and distributed heaters. All three regimes of pool boiling have aptly been captured with both plain and structured heaters, allowing the development of the boiling curve. The predicted value of critical heat flux for the plain heater agrees with Zuber correlation within 10%, illustrating both quantitative and qualitative capability of the proposed algorithm.

Dedicated to My Parents

Acknowledgments

Firstly, I would like to express my gratitude to my supervisor Dr. Dipankar N. Basu for his expert guidance throughout the course of my Ph.D. His research attitude and insightful feedback pushed me to sharpen my thinking and brought my work to a higher level. I wish to thank my co-supervisor Dr. Pranab K. Modal, whose continuous encouragement and knowledge sharing helped me complete my work.

I would like to express my appreciation to my doctoral committee members, Dr. Amaresh Dalal, Dr. Vinayak N. Kulkarni, Dr. K. A. Reddy, and Dr. Pankaj Mishra for their suggestions and judicious comments on my work. My special thanks goes to Dr. Amaresh Dalal and Dr. Arnab K. De for making me understand the concepts of CFD and getting me thinking to pursue a research career in CFD. I would like to pay respect to my thesis supervisor late Dr. Subhash C. Mishra for encouraging me to choose research as career path.

This acknowledgment would never be complete without mentioning my labmates Nitesh, Sambit, Sudip, Harshad and Rajkumar for personal and professional discussion on various topics. I would like to mention Sambit here especially, who is also working on LBM. Continuous discussion with him on our research area enriched me a lot.

I must also take this opportunity to thank my parents whose continuous support were worth more than I can express here. Their continuous motivation helped me throughout my academic career and made me what I am today. Finally, I must mention my wife Trina here, whose continuous encouragement helped me cruise through my tough times and land where I am today.

Aritra Mukherjee

Contents

Nomenclature

f - the particle distribution function for momentum equation

x - coordinate direction

y - coordinate direction

z - coordinate direction

c - velocity of the distribution functions

t - time

u - x-direction velocity

v - y direction velocity

E - total energy

T - temperature

R - universal gas constant

w - weight factors

c_s - lattice sound speed

P - macroscopic pressure

M - orthogonal transformation matrix for the MRT scheme

C - specific heat

p - pressure (Pa)

F - body force (N)

q - heat flux (w/m^2)

g - particle distribution function for energy equation

G - constant for calculating pseudopotential function

S - source term

S_m - matrix containing different relaxation time parameters (momentum equation)

S_T - matrix containing different relaxation time parameters (energy equation)

S_{ind} - indicator function for calculating surface wettability force

Greek symbols

ρ - density

Ω - collision operator

τ - relaxation time for momentum equation

υ - kinematic viscosity

ψ - pseudopotential function

ϕ - tensor notation

μ - viscosity $\left(Pa.s\right)$

υ - kinematic viscosity $\left(m^2 / s\right)$

τ - Relaxation time for LBM

σ - Surface tension

σ_m - Tuning parameter for multiphase MRT model

β - Tuning parameter for pseudopotential force calculation

Subscript

r - relative

b - bulk

l - liquid

v - vapor

g - gas

w - wall

i - lattice direction number

R - reduced properties

C - critical properties

bo - boundary

lu - lattice unit

Superscript

eq - equilibrium

$*$ - dimensional parameters

SC - Shan-Chen

wet - wettability

ext - external

Abbreviations

BGK - Bhatnagar-Gross-Krook

CFD - Computational Fluid dynamics

DDF - Double Distribution Function

DWC - Dropwise Condensation

EOS - Equation of State

FDM - Finite Difference Method

FVM - Finite Volume Method

FWC - Filmwise Condensation

LB - Lattice Boltzmann

LGCA - Lattice Gas Cellular Automata

MD - Molecular Dynamics

MRT - Multiple Relaxation Time

NSE - Navier-Stokes Equation

PDE - Partial Differential Equation

PR - Peng Robinson

SC - Shan-Chen

SRT - Single Relaxation Time

VdW - Van der Waals

List of Figures

List of Table

Chapter 1

Introduction

1.1 Introduction

Phase Change heat transfer is a comprehensive research field as it finds applications in various engineering and natural phenomena. The phase change process happens when the matter is changed from one state to another (solid, liquid, or gas), as one phase releases or gains adequate energy to change into the other phase. Among all phase change processes, boiling and condensation play cardinal roles in various engineering applications as they are associated with very high heat transfer rates. Pool boiling is one of the most effective modes of heat transfer as it involves the exchange of both sensible and latent heat, and offers its contribution from simple domestic cooking to industrial processes such as power generation, electronic cooling, and more. Flow boiling, involving the forced bulk motion of multiphase mixture, has greater relevance to numerous commercial appliances, encompassing gigantic power boilers to micro heat sinks. While the boiling process depends on the supply of sufficient energy to the liquid phase, the condensation process involves the release of a high amount of energy, which is very useful for industrial cooling applications.

Due to their widespread applications, scientists have spent decades researching the topic of boiling and condensation heat transfer processes[2,6]. Systematic investigation of boiling and condensation processes is imperative for a better understanding of intricate thermal hydraulics of different natural and engineering phenomena. Experiments and theoretical analyses were the only way to study the boiling and condensation processes up to the late twentieth century. Though experiments can predict the basic phase change behavior and provide several empirical relations corresponding to specified experimental arrangements, they are unable to illustrate the complex thermal-hydraulics behind the bubble generation process in boiling, or the drop and film generation in the condensation process. Towards the late twentieth century, with the advancement in computer technology and the development of different numerical techniques, researchers started simulating various boiling and condensation related problems using different CFD methods to analyze the underlying thermohydrodynamics of these processes.

There are two primary approaches for simulating the governing equations of fluid dynamics and heat transfer - continuum and discrete. In the continuum approach, macroscopic transport equations are obtained by applying mass, momentum, and energy conservation principles. These differential equations are discretized using different numerical methods (FVM, FDM) and converted into algebraic equations. Also, the whole solution domain is discretized into small volumes or separate grids points. The system of equations is solved at each gridpoint, or volume for the physical parameters (pressure, velocity, temperature). Though these conventional numerical techniques have been used extensively for simulating different boiling and condensation problems over the years, they are up against formidable odds in some aspects. In all these methods, phase change can not start naturally, and hence, phase change simulations following these methods require either a nucleus to be placed at the nucleation site or ingraining of pseudo boiling approach in the model itself. The employment of the aforementioned schemes can not simulate the primary nucleation process and seems to be inefficient in capturing significant information during the initial stage. Also, these methods require too much computational time, even days, to complete a single simulation.

The discrete approach is based on the microscopic description of the simulation domain, i. e. the fluid medium is made of microparticles (atoms, molecules), which collide with each other and with the container walls. The movement of these particles is tracked with the fundamental momentum conservation equation (Newton’s law of motion). Once the velocity and position of each particle are determined, macroscopic pressure and temperature are related to the kinetic energy of the particles. This method is known as molecular dynamics simulation. MD simulation method is simple and it can easily handle multiphase systems and complex geometries. The main disadvantage of using MD simulation is that it needs an enormous amount of computer resources and simulation time, as the method involves solving a large number of equations simultaneously due to a large number of microparticles present in the medium.

Lattice Boltzmann method has emerged as an alternative numerical simulation technique in recent years which bridges the gap between the macroscopic and microscopic approaches by considering the behavior of collection of particles as a unit instead of tracking the individual particles. This collection of particles is known as the particle distribution function. The Boltzmann equation is the fundamental equation governing the behavior of the distribution function and it is obtained from the kinetic theory of gas and statistical mechanics. The continuous Boltzmann equation is discretized in velocity space, physical space, and time to obtain the discretized Boltzmann equation and solved over discrete lattices inside the domain using suitable schemes. Macroscopic variables like density, velocity, and temperature are related to the moments of the distribution functions. This method is advantageous over the conventional approaches in many aspects. It is much faster than the other conventional approaches and is highly suitable for parallel computing. Also, it can handle complex domains and multiphase flows very easily.

1.2 Historical Development of the Lattice Boltzmann Method

The modern LB method is originated from the lattice gas cellular automata (LGCA) model introduced by Hardy, Pomeau and de Pazzis[7] in 1973 and known as HPP model based on the name of the original authors. This model uses the concept of cellular automata proposed by Von Neumann[8] in the 1940s. A cellular automata model consists of a group of colored cells of a certain shape, and each cell evolves through discrete time steps according to a set of rules defined initially depending on the state of neighboring cells. Hardy et al.[7] used the concept of cellular automata on d-dimensional regular lattices in a discrete domain, where the gas is represented by boolean variables (0 or 1) and moves on the lattices according to the specified set of instructions depending on the neighboring lattices. This set of rules is generated from the collision and propagation of gas particles from one cell to another through discrete time steps. Though this model allowed complex fluid flow analyses, it had some major drawbacks, like intrinsic statistical noise generation, lack of isotropy of the lattices, absence of Galilean invariance property, unphysical velocity-dependent pressure, and large numerical viscosities.

Frisch et al.[9] resolved the main drawbacks of the HPP model and obtained the Navier-Stokes equation correctly by using a two-dimensional hexagonal lattice structure in 1986. Their model is generally known as the FHP model, where the lattice Boltzmann equation was used in their LGCA model to calculate the physical viscosity. D’Humires[10] et al. extended the FHP model for three dimensional calculations. Upto this point, the basic solution variables were the boolean populations whose evolutions are governed by a set of collision and streaming rules depending on suitable conservation laws. The microscopic nature of the LGCA method possessed intrinsic statistical noise and required huge computational memory and time. Macnamara and Zanetti[11] were the first to replace the boolean population with a probabilistic particle distribution function obtained from the kinetic theory of gas, originally proposed by Ludwig Boltzmann in the late nineteenth century[5]. This probabilistic distribution function is an ensemble average of discrete particles in the domain, whose smooth nature helped in removing the statistical noise present in the LGCA model. This method is computationally much more efficient than the older LGCA models, as they use the collective behavior of particles instead of considering and tracking individual particles at each cell. The introduction of the averaged distribution function in the place of individual particles and boolean operations of LGCA has given rise to the basic lattice Boltzmann method. Though this model used the distribution functions, it followed the basic LGCA rules for evolution of the distribution functions. As a result, the use of this model is restricted to low Reynolds number fluid dynamics problems, and change of viscosity is not possible.

Higuera et al.[12] simplified the LBM by incorporating a linearized collision operator in the Boltzmann equation, which argues that the particle distribution functions assume a certain value at the local equilibrium state of the domain. The concept of this equilibrium distribution function was already present in the kinetic theory of gas and statistical mechanics, proposed by Boltzamn and Maxwell separately and known as the Maxwell-Boltzmann distribution function[5]. This collision operator was originally proposed by Bhatnagar, Gross, and Krook[13] in 1954 and is known as BGK collision operator. Eventually, several authors[14,15] used this BGK approximation in LBM to recover the accurate behavior of macroscopic NS equations.

A major drawback of the BGK relaxation parameter based on a single relaxation time is that all the populations are forced to relax at the same rate in the domain, which introduces numerical inaccuracy and instability in the simulation[16]. To cope up with this issue, another collision model is introduced by Lallemand et al.[16] which transforms the population to moment space from velocity space using a transformation matrix. In the moment space, the collision occurs at different relaxation rates, and then the populations are transformed back to the velocity space using the inverse of the transformation matrix. This model is known as multiple relaxation time lattice Boltzmann model, and the use of this model enhances the stability and accuracy of the numerical simulation, though it increases the simulation computational time moderately.

LBM can be used to solve the energy conservation equation as well as the momentum conservation equation. Three separate approaches are available in the literature for simulation of the energy equation – the multispeed approach, the double distribution function approach, and the hybrid approach[17]. Alexander et al.[18] proposed the multispeed approach back in 1993, which was an extension of the isothermal LB approach. They have considered higher-ordered lattices for the simulation, where additional discrete velocities are necessary, and the equilibrium particle distribution functions consist of higher-order velocity terms so that the macroscopic energy equation can be recovered. However, the multispeed approach suffers from several limitations – numerical instability, narrow temperature variation range, and an unalterable value of the Prandtl number. Due to these drwabacks, this approach is not very popular in the LB community.

The double distribution function approach, proposed back in 1993[19], uses two different distribution functions; one for the momentum equation and another for the energy equation. The macroscopic velocities are taken from the flow field solution and used for the calculation of distribution functions for the temperature field. The DDf-LB model can be divided into three basic models, where the distribution functions represent different field properties – the temperature-based model[19,20], the internal energy-based model[21,22], and the total energy-based model[23]. This approach has gained popularity over the years among the LB researchers due to its' excellent numerical stability, and the capability to adjust the Prandtl number.

Filippova et al.[24,25] used a completely different approach to simulate the thermal field, which was formally established by Lallemand et al.[26] later. In this scheme, the flow field is solved by LB equations, while the energy equation is numerically simulated using the finite difference method or any other conventional approach. Among these three approaches, the DDF approach and the hybrid approach are popular and frequently used by the LB community for different heat transfer problems.

1.3 Comparison between Conventional CFD Methods and LBM

The basic numerical framework stemming from conventional CFD approaches has many differences from the LB numerical approach.

- The fundamental governing equation of the LB method is the mesoscopic Boltzmann equation, while the conventional approaches use the macroscopic transport equations for fluid dynamics and heat transfer – the continuity equation, the momentum equation (Navier-Stokes equation), and the energy equation.
- The LB method tracks the evolution of particle distribution functions through time and calculates the macroscopic parameters like velocity, pressure, temperature, and density from the particle distribution functions at each timestep using the discretized Boltzmann equation. The macroscopic transport equations are discretized in conventional approaches to form a system of linear equations, where the physical flow parameters are the basic variables. The system of linear

equations is solved using different numerical iterative techniques to obtain the parameters like velocity, pressure, density, and temperature directly.

- The macroscopic pressure is calculated from density via the equation of state in LBM, while the pressure Poisson equation is needed to be solved in conventional approaches. Solving the Poisson equation is time-consuming, which makes the conventional approaches computationally expensive.
- From the implementation point of view, all the operations in LBM are local algebraic operations, which bring straightforwardness to the solution procedure. In comparison to that, solving a system of linear equations obtained from the PDE can be very challenging and introduce too much complexity in the solution procedure.
- All the algebraic operations in the LBM are local to the lattice nodes, which renders it highly parallelizable in comparison to the conventional NSE solvers.

Despite having several advantages over the conventional CFD approaches, LBM still suffers from some serious disadvantages. Its applicability is still limited in the turbulent flow region, and it suffers from numerical instabilities and inaccuracies in high-density ration multiphase simulations. LB researchers are trying to overcome these restrictions gradually by incorporating several new numerical schemes, which is very promising to make it capable of solving all kinds of fluid dynamics and heat transfer problems in the future.

1.4 Literature Survey

Applicability of the lattice Boltzmann model in multiphase fluid dynamics and heat transfer problems has become a widespread research topic in recent years. Accordingly, a detailed literature survey is presented in this section.

1.4.1 Different LB multiphase models

The earliest multiphase model was developed by Rothman et al.[27] in 1988 using the lattice gas model. Gunstensen et al.[28] modified this model using the LBM structure in 1991, which is commonly known as the color gradient model. In this model, two-fluid component populations are denoted by two colors - blue and red. Two separate distribution functions are defined to represent the two fluids. Gradually, several authors[29–31] worked towards the improvement of the basic color gradient model and published their research works. The main disadvantage of this model is that it can’t handle high-density ratio multiphase situations. Researchers have been using it to simulate multiphase flows with fluids having almost identical densities, such as droplet deformation and breakup in simple shear flow[32], two-phase flow in porous media[33], droplet formation in a cross-junction microchannel[34], and high viscosity ratio two-phase parallel flow in a channel[35]. Though some authors have simulated high-density ratio problems related to static droplets and bubbles[29,36], the situation deteriorates when one phase starts moving[37]. There are very few situations in multiphase flow problems, where the density ratio is too low, which can be handled accurately by the color gradient model. Due to this reason, the color gradient model is not very popular in the LB community.

One of the most popular LB multiphase models, commonly known as the Shan-Chen model was originated in 1993, just after the color gradient model. The model is named after two of its original authors Shan and Chen[38], who proposed the calculation of a local interaction force between the populations of neighboring nodes, based on the intermolecular forces between pairs of populations, which depends on their density and distance. The interparticle interaction force can be expanded in two terms. After some mathematical rearrangement of the terms, it can be found that one of the terms modifies the ideal equation of state used in single phase LBM and adds an extra term, which allows the coexistence of liquid and vapor phases simultaneously in a medium. This non-ideal equation of state is known as Shan-Chen equation of state The other term acts like the surface tension term of the multiphase Navier-Stokes equation. If the macroscopic pressure tensor is calculated from the pseudopotential force, it can be found that it is not exactly the same as the macroscopic NSE pressure tensor, though they look almost identical[5,39]. Despite this anomaly, the behavior of the bulk phases, i. e., different density profiles, and surface tension calculation behavior remains in an acceptable accuracy range.

Due to the computational efficiency and simple implementation procedure, the SCLB model has become very popular among the LB multiphase community. However, the basic pseudopotential model proposed by Shan and Chen[38] has several shortcomings[40]. One of the major problems with this model is the generation of spurious currents in the vicinity of the interfacial region. These false velocity currents increase with increasing density ratio and simulation becomes numerically unstable and inaccurate. The original SC model can simulate multiphase problems only upto density ratios of the order of O(10), which is far away for most of the practical multiphase scenarios. Also, the original model is thermodynamically inconsistent. A thermodynamically consistent multiphase model should follow the Maxwell area construction rule strictly. Maxwell area rule depicts that at a particular temperature, two unique liquid and vapor densities should exist, which also fixes the bulk pressure value. Liquid and vapor densities obtained from the numerical solution must match the analytical values obtained from the Maxwell area construction rule. The SC non-ideal equation of state lacks a proper definition of temperature. A temprature like consatnt parameter exists, which controls the phase seperation process. Thus, obtaining proper coexisting liquid and vapor density values are impossible within the framework of basic SC model. As a consequence, this model can never be applied to thermal multiphase flow problems.

Numerous modifications are proposed over the years to counter the challenges faced by the basic pseudopotential model. Shan[39] and Sbragaglia et al.[41] suggested the inclusion of more neighboring lattice nodes other than the immediate neighboring nodes of the lattice node where the interaction force is calculated. This increases the order of isotropy of the discretized interparticle interaction force, which in turn helps in the reduction of the spurious current making the simulation numerically stable at high-density ratios. Yuan et al.[4] introduced a modification in the calculation of the pseudopotential, where they offered a way to incorporate any realistic equation of state in place of the original SC equation of state. These realistic equations of states have proper definitions of temperature, and thus it is possible to calculate liquid and vapor coexisting density values at specified temperatures. They presented results for coexisting liquid-vapor densities at specified temperatures for different equations of states – Vanderwaal's equation, Peng-Robinson equation, Redlich-Kwong equation, and Carnahan-Stirling equation. They concluded that the use of the PR equation ensures that the simulation can go upto density ratio in the order of O(1000), though the results agree with the analytical liquid and vapor densities till reduced temperature $T_R = 0.9$. Beyond that, the vapor branch starts deviating from the analytical value. Zhang and Tian[42] found another way of incorporating different equations of states into the model by modifying the equilibrium distribution function, but their model generates relatively large spurious currents and fails to work at a high-density ratio.

Kupershtokh et al.[43]worked on the original SC force term, introduced a general approximation of the gradient of the potential function, and incorporated realistic equations of states in it. They used a new force scheme proposed in 2006[44], known as the exact difference method. They could achieve a very high-density ratio in their simulation for the planar interface between two phases. Gong et al.[45] modified the original SC force structure and incorporated it with the Yuan et al.[4] model to present a new model. They analyzed the effect of forcing schemes on the simulation of static droplet problem and showed that the exact difference method[44] works best along with the PR equation of state, and they were able to simulate static multiphase flow problems up to $T_R = 0.6$ where density ratio is in the order of O(1000). They simulated the movement of a three-dimensinal droplet on a surface with variable wettability due to wettabilty gradient.

McCracken et al.[46] first used MRT-based collision operator in place of BGK collision operator for simulating multiphase flows with the pseudopotential model. They simulated two-dimensional static droplet problems, capillary waves, and oscillating liquid cylinder problems. They concluded that MRT based pseudopotential model is numerically more stable than the SRT-based model. Yu et al.[47] showed that proper tuning of the free parameters of the MRT scheme can significantly reduce the false velocity current in the vicinity of the two-phase interface. Li et al.[48] introduced a modified MRT-based pseudopotential multiphase model with an improved forcing scheme. With their new scheme, they were able to simulate the splashing of a droplet on a thin liquid film at a density ratio of 500 and Reynolds' no. ranging from 40 to 1000. Albeit the basic SC model confronted several restraints in multiphase flow simulation, these improvements over the years rendered it capable for simulation of many practical multiphase problems like droplet/bubble behaviors in different environments, contact line movement, slippage phenomenon, viscous fingering, fuel cell applications to name a few[40].

The third kind of LB multiphase model is the free energy based LB multiphase model which was developed by Swift et al.[49,50] in 1995. In this model, the non-monotonic equation of state is assimilated into the pressure tensor term in the momentum conservation equation, and the equilibrium particle distribution function is changed accordingly. Luo et al.[51] argued that the original free energy multiphase LB model lacks Galilean invariance for the viscous term in the NS equation. Holdych et al.[52] proposed an alteration to make the model Galilean invariant by redefining the stress tensor. This model has been applied to simulate several multiphase flow problems involving droplet and bubble dynamics[53,54], spinoidal decomposition[55,56], phase seperation[57], bubble migration[58], flow in porous media[59], and more. Inamuro et al.[60] improved Swift's original model and was able to solve high-density ratio multiphase problems accurately, but their scheme needs to solve the pressure Poisson equation, which takes excessive computational time and contradicts the basic LB philosophy of omittance of the Poisson equation. Zheng et al.[61] proposed another modification which simpler than Inamuro's model, but works for density-matched problems[62].

In this model, a free energy functional is defined at first containing the thermodynamics of the systems, and due to this reason, this model is always thermodynamically consistent. The predefined thermodynamically consistent free energy functional of this model is actually beneficial over the pseudopotential model, which is thermodynamically inconsistent without major modifications[5]. The major drawbacks of the free energy model are the generation of spurious currents, complexity in implementation, and higher computation cost in comparison to the pseudopotential model. Also, the basic pseudopotential model inherently maintains Galilean invariance, while the basic free energy model lacks it.

Another type of LB multiphase model is developed based on the interface tracking approach following the conventional multiphase models. This model is developed by He et al.[63] in 1999 and commonly known as HCZ based on the name of the original authors. Two separate distribution functions and their corresponding LBEs are solved in this scheme, and the Cahn-Hilliard interface tracking equation with NSE can be recovered macroscopically from his model. The drawback of this model is that this model can't simulate high density ratio problems. The maximum density ratio for multiphase problem simulations achieved with this model is in the order of O(10)[37]. Eventually, several modifications are proposed to increase the capacity of the basic model to simulate high density ratio problems[64–67]. Lee et al.[64] proposed use of directional derivatives to increase the density ratio. Later Lee et al.[65], [67] and Amaya-Bower et al.[66] proposed the use of discretization schemes with higher isotropy along with the directional derivatives. These improved models can simulate problems with density ratio in the order of O(1000).

A few publications are there which compare the basic LB multiphase models theoretically[49,51,68] and numerically[69,70]. General comparison between all these four models[37] indicates that the SC pseudopotential model is very efficient and can be used for high-density ratio multiphase problem simulations, but the basic pseudopotential model is less accurate than the other models. Proposed modifications over the years improved the model and rendered it capable of accurate simulations of high-density ratio problems, which made the model very popular among LB multiphase researchers.

Along with the development of isothermal multiphase models, researchers stated extending those models incorporating the energy equation to solve the phase change heat transfer problems. Dong et al.[71] proposed a thermal phase-field LB model based on Zheng et al.'s[61] binary fluid model where they added a source term to the Cahn-Hilliard equation to define the phase change. They applied this model to simulate bubble growth and departure from a superheated wall in a two-dimensional wall[71,72]. Sun et al.[73] extended this model in three-dimensions to simulate the nucleate boiling phenomenon. Safari et al.[74,75] extended Lee et al.'s[67] isothermal phase-field multiphase LB model by redefining the divergence of velocity field to incorporate liquid vapor phase change. They validated the one-dimensional Stefan problem and the two-dimensional droplet evaporation problem. Begmohammadi et al.[76] used this model to simulate pool boiling from a superheated wall. The main problem with these two models is that they need an initial interface to start the liquid-vapor phase change phenomenon, i.e. the phase change can't occur naturally in the domain. One has to place a small bubble on the superheated wall to start the phase change phenomenon, like the conventional FVM based models.

Tanaka et al.[77] reported a very interesting effort of simulating phase-change problems within the LB framework based on Inamuro et al.'s[60] phase-field model. In the isothermal phase-field model, they introduced a new velocity distribution function to develop an evolution equation for pressure. While they were able to attain numerical stability at higher density ratios, the solution of the pressure Poisson equation is very much in contradiction to the LB philosophy. Tanaka et al.[77] acknowledged their algorithm to be computationally expensive, which restricted their exploration only to nucleate boiling.

The use of the pseudopotential model to simulate phase change heat transfer started back in 2003 when Zhang et al.[78] reported their work on nucleate boiling. They modified the force term to accommodate the liquid-vapor phase change phenomenon. They considered a standard Rayleigh-Benard setup, where upper and lower walls are no-slip solid boundary walls, and side walls are periodic. To generate thermal perturbation for boiling, they added small temperature fluctuations at the equation of state in the near-wall grid points. The formation of two separate nucleation sites, eventual bubble rise, and collapse can be observed from their simulation results.

The modern thermal pseudopotential model uses a different technique from Zhang et al.'s[78] force modification approach. Hazi et al[79] first used the entropy balance equation to simulate the liquid-vapor phase change phenomenon, and simulated nucleate boiling from a cavity placed on a superheated wall using constant heat flux boundary condition. However, they could not obtain the macroscopic energy equation correctly, and some numerical inaccuracies are found in their results. Gong et al.[80] later improved their model to simulate the nucleate boiling correctly and validated Fritz's[6] analytical correlation of bubble departure diameter vs. gravity correctly. They simulated nucleate boiling in a rectangular domain, placing a microheater on the bottom wall which was used for the thermal perturbation. Vapor bubble was generated from the saturated liquid on the heater under constant temperature boundary condition, without the requirement of any initial interface. This is the most popular model used nowadays for the simulation of different kinds of phase change heat transfer problems. Li et al.[81] used a hybrid pseudopotential-based model where they used the conventional FV approach to solve the energy conservation equation. They simulated three boiling regimes – nucleate, transition, and film regime and were able to generate a boiling curve. The pseudopotential-based thermal LB model has also been used in other thermal multiphase flow problems besides boiling like condensation[82], droplet evaporation[83], supercritical fluid flow[84] to name a few.

A comparison[85] between all the phase change heat transfer models reveals that the pseudopotential based thermal multiphase model is very efficient computationally, and does not require an initial interface to start the phase change process, while other models require a bubble or droplet to be placed in the domain initially. As a consequence, simulating nucleation phenomenon or boiling regimes is only possible with the pseudopotential-based thermal multiphase model. The only disadvantage of this model is that it can't simulate phase change problems with a very high-density ratio yet, which is a requirement for many practical scenarios. However, researchers are trying to improve the model to simulate high-density ratio phase change problems.

1.4.2 Flow boiling in narrow fluidic channel

Precise numerical simulation of multiphase flow is one of the most arduous tasks in the purview of computational fluid dynamics, the primary contributor towards such intricacy being the discontinuous property variation across a dynamic and malleable interface of infinitesimal thickness. The scenario is particularly delicate with liquid-vapor mixtures, owing to the involvement of high density and viscosity ratios. Such flow situations, however, are very much ubiquitous both in nature and industrial processes, encompassing large-scale power boilers, cooling towers and airconditioners, to the microarteries of cardiovascular system. Rapidly-increasing focus on miniaturization and effort to mimic biological systems in heat transport devices have projected flow boiling through a narrow fluidic channel as a very lucrative application, particularly with its potential of offering high heat flux with large area-to-volume ratio and small temperature differential that has envisioned a new paradigm of experimental and numerical research with multiphase thermohydrodynamics in the present millennium, a comprehensive perspective of which is available in Li et al.[86]. Possible involvement of multiple length and time scales, the dependence of the phenomenon on the distribution of nucleation sites, the enhanced role of surface topology and wettability, and lesser reliance on gravity are some of the additional factors that can have pivotal influence in mini- and microscales, thereby demanding dedicated approach for appraisal. The incompetence of common measuring tools at smaller scales and hindrance in optical assessment due to refractive interface imposes enhanced reliance on numerical procedures, stimulating the development of several relevant techniques[87,88].

One major challenge in multiphase modeling is the identification of suitable forms of macroscopic governing equations. For a boiling channel experiencing a flow of liquid-vapor mixture, both phases can notionally be regarded as distinct fluids, characterized by individual velocity and temperature fields, and separated by multiple, deformable, and moving interfaces, with mass, momentum and energy interactions across the same. Realization of a phase as continuous or dispersed differs widely with the flow regimes[2,6], proclaiming for the adoption of some averaging procedure to derive effective conservation equations and incorporation of appropriate, often empirical, closure relations. A multitude of averaging approaches has been proposed over the years[89–92], with one common frailty being the uncertainty in exactly locating a constituent at a particular instant, consequently limiting the predictions mostly to gross thermalhydraulic characterization. On the contrary, the local instant formulation[93], despite theoretically being an excellent option for separated flows, involves added mathematical difficulty and greater computational resource requirement, while also necessitating the validity of continuum within each sub-region. That, however, can act as the base for developing the macroscopic conservation equations following suitable averaging approaches. The Eulerian-Lagrangian description is especially amenable to particulate flows[94–97], but is commonly not favored for diffusion-dominated or phase-change problems. The Eulerian-Eulerian averaging is more popular, owing to its direct relevance to human observation in terms of the time-space description of the physical phenomenon, yielding numerous relevant research efforts. Conventional multiphase computation, however, requires a precise algorithm for coupling the interfacial information with the conservation equations, which can either be a surface-based interface tracking or volume-based interface capturing approach. While the classical MAC/SMAC/SMMC-based algorithms[98] belong to the former category, techniques like level-set[99], volume-of-fluid[100,101], and phase-field[102] are popular examples of the latter. Several logical combinations of these methods are also available in the literature[103,104], allowing a gradual development in associated concepts. Quite a few recent efforts to apply similar methodology for analyzing boiling in smaller dimensions are also available[105–110]. However, as was observed by Kharangate et al.[111], most of the reported multiphase computational efforts are restricted either to pool boiling or simplified flow boiling, consequently limiting themselves mostly to validation studies. A major impediment for Euler-averaged algorithms is the requirement of pre-defined vapor embryo, to initialize the interface, which makes them vulnerable for realistic flow boiling situations.

A possible remedy to the above conundrum can be contrived through the use of LB methods, which has emerged as a strong contender for large-scale multiphase simulation over the last couple of decades, with its linear convection operator in velocity-space and second-order numerical accuracy in space and time through multiscale expansion being particularly alluring[5,37]. The discrete-particle-based approach allows natural phase separation, assuaging the need for any interface tracking or empirical relations. Following the pioneering attempt of Rothamn et al.[27], several multiphase-LB algorithms have been proposed, which have already been described in the previous section.

The pseudopotential-based approach, originally formulated by Shan et al.[38], and modified for the simulation of thermal flows by Yuan et al.[4] and Gong et al.[45,80] has found particular favor from the boiling community, as can be substantiated through the large volume of available literature[80,81,112–114]. It employs a nearest-neighbor interaction model, which is a close approximate to the Lennard-Jones potential, allowing efficient computation and relatively-smooth representation of the interface.

Despite reasonable success with pool boiling simulations, the application of the Shan-Chen-LB model (SC-LBM) for flow boiling is quite scarce to date. Gong et al.[115] were probably the first ones to simulate saturated flow boiling at low Reynolds number through a horizontal microchannel in the absence of gravity, extending their dual-distribution-LB methodology[80]. Bubbly and slug flow regimes were detected by varying inlet velocity and Jacob number, and other logical parametric effects were observed. Sun et al.[116] employed the same philosophy in a vertical channel of 7.5 aspect ratio, designed with several discrete nucleation sites on both walls, with subcooled inlet temperature, and were able to reproduce the associated physics. They applied constant heat flux and wall temperature boundary conditions on the nucleation sites and simulated the bubble generation, coalescence and subsequent Taylor bubble flow under the effect of liquid inertia and buoyancy. The effect of contact angle on bubble generation behavior and heat transfer rate using the same simulation setup was considered in the follow-up study by Sun et al.[117]. Recently, Zhang et al.[118] used the MRT-LB model for simulating flow boiling in a vertical channel using single or multiple nucleation sites and studied the effect of inlet velocity and thermal perturbation effect on boiling regimes and heat transfer rate.

The microdynamics of subcooled boiling involves intricate momentum and energy transports across the vapor-liquid interface, with the possible presence of a superheated liquid layer at the heated surface and subcooled liquid away from it. Such thermal non-equilibrium can enforce the vapor embryo to experience substantial temperature gradient immediately on its initiation. Energy added to the fluid needs to be simultaneously utilized for single-phase liquid heating and evaporation, which is noticeably different compared to a saturated mixture. Finite-volume algorithms often adopt the wall-heat-flux-partitioning approach to counter the same, which involves the use of numerous empirical relations[119] . The mesoscopic SC-LBM framework has the potential of making substantial contribution in this precise context. Though the above studies are testimony towards suitability of SC-LBM for flow boiling, intricate thermalhydraulics of flow boiling in a narrow fluidic horizontal channel in presence of the gravity force is yet not explored properly.

1.4.3 Condensate droplet formation on nanostructured surfaces

Condensation is a widespread heat transfer process found in both nature and engineering applications[2,6], occurring through nucleation from vapor followed by the subsequent growth of the nucleus in a condensate droplet. It may transpire as homogeneous or heterogeneous nucleation depending on whether the nucleus is formed from a bulk vapor phase or in contact with a foreign object[6]. Heterogeneous nucleation is more likely to happen due to the lowered activation energy in comparison to homogeneous nucleation[6,120]. Vapor condensation on a solid substrate has been an active area of research due to its innumerable importance in industrial applications[111,121–124].

Superhydrophobic surfaces patterned with nano or microscale structures have gained much attention in both industry and scientific community in recent years considering their distinctive wetting properties and various applications such as heat transfer enhancement, quick droplet removal, self-cleaning, defrosting, anti-icing, and many more[125–128]. The geometric morphology of structured surfaces influences condensate droplet nucleation and growth significantly. A liquid droplet deposited on a solid surface can display two different nucleation patterns depending on the toughness topology of the surface structure – Cassie state or Wenzel state. Depending on the height, width, and spacing of the pillars, a liquid droplet can propagate inside the grooves and wet the whole solid, or it can sit at the top of the posts and does not conform to the solid surface[129]. The first state of the droplet is known as Wenzel state, and the second one is known as Cassie state. If a liquid droplet attains Cassie state on a solid substrate with an apparent contact angle larger than 150^0 and a roll-off angle less than 10^0, the surface is mentioned as superhydrophobic. A hydrophobic surface protruded with nanostructures might present excellent superhydrophobicity, which has many potential applications in micro and nano engineering[130].

Proper understanding of the effect of surface roughness topology on droplet condensation is essential for the optimized design of structure on a solid substrate, which will be helpful for the control of the condensation process in industrial applications. Several research groups have devoted their effort to the study of condensation on rough surfaces in the previous years[3,131–135]. Though experiments and theoretical analyses can predict the basic behavior of condensate droplets on rough surfaces, they can't provide the detailed underlying thermohydrodynamic analysis due to the limitation in proper experimental and visualization techniques. In recent years, the lattice Boltzmann method (LBM) has emerged as an excellent numerical approach to address this issue.

Liu et al.[82,136] extended the applicability of Gong et al.'s[80] model for the condensation problem. They simulated condensate film generation on a hydrophilic flat surface[136] from saturated vapor using constant wall temperature boundary condition. They validated their numerical results against Nusselt's analytical solution[2] of laminar film thickness and heat transfer coefficient to establish their model. In another work[82], they simulated dropwise condensation from a single nucleation site on a vertical hydrophobic flat plate in a three dimensional domain filled with saturated vapor. They discussed the movement of the condensate droplet under the influence of the buoyancy force along with corresponding velocity and temperature fields. Also, they elaborated the heat transfer rate on the nucleation site for periodic droplet nucleation and departure. Since then, several authors have published their work [136–139] studying condensation on smooth surfaces having different kinds of surface wettability patterns.

Works on condensation on a rough surface with micro/nano-textures are rather limited to very few numbers of publications. Zhang et al.[130] studied isothermal droplet condensation on superhydrophobic nanoarrays and showed the formation of Cassie and Wenzel droplets depending on the topology of the nanopillars. They explained the intricate hydrodynamics of the formation of a Cassie droplet through their numerical results. They plotted the Laplace pressure differential at top and bottom surface on condensate droplet, from nucleation point to growth and merger of multiple nuclei, and elaborated the situations favorable for the formation of a Cassie or Wenzel droplet. In a similar kind of work, Fu et al.[140] studied the effect of the topology of the microstructures on droplet condensation. Vasyliv et al.[141] studied droplet nucleation and growth mechanism on cold solitary surface pillars without focussing on the growth of the droplet into Cassie or Wenzel state and wetting behavior of the surface. They analyzed the patterns of droplet formation, coalescence, and corresponding mass condensation rate using different kinds of structure geometries – rectangular, triangular, and semi-circular. Li et al.[142] used thermal multiphase LB model to study the growth of Cassie and Wenzel droplets on a rough surface with variable wettability and fixed surface roughness in a gravity-free environment. They concluded that the surface wettability governs the ultimate droplet generation pattern; i.e., superhydrophobic surfaces generate Cassie droplet, and with the gradual reduction in the contact angle, Wenzel droplet starts growing conforming with the solid surface.

The above literature survey indicates that none of these works studied the effect of roughness topology and cold surface temperature effect on the condensation behavior in temperature-controlled condensation process numerically, i. e. the formation of the droplet into Cassie or Wenzel state and their subsequent behavior, which is paramount for designing an optimal rough surface for condensation.

1.4.4 Condensate flow dynamics on microstructured surface

Condensation on a cold surface may happen in two forms[6]. For a hydrophobic surface, condensate liquid can't wet the surface, and hence the liquid remains as separate drops instead of forming a liquid film. This type of condensation process is named as dropwise condensation (DWC). Another form of the condensation process is called filmwise condensation (FWC), where the liquid wets a hydrophilic surface and forms a stable film on it. The liquid has a strong affinity to hydrophilic surfaces. Accordingly, the vapor condenses quickly on them in comparison to hydrophobic surfaces. The liquid condenses as a film on a surface, and it breaks the contact of the condensing vapor with the cold spot. Though initially, the condensation rate is higher for hydrophilic surfaces, later it reduces due to the loss of contact between vapor and the cold wall. Various experimental and numerical studies[111,123,133,143] over decades suggest that DWC is preferable to FWC in the purview of heat transfer rate.

Scientists have spent decades researching condensation heat transfer enhancement. Numerous publications[131,133,144] in this field suggest that tuned micro or nano-scale structures can promote hydrophobicity of a surface, which in turn promotes DWC. Depending on the morphology of a rough surface, a droplet can grow into Cassie or Wenzel state, which is described in the previous section. It is quite reasonable to assume that a surface where a droplet remains at Cassie state will have a higher contact angle and promote DWC, as the condensate liquid will always prevail in drop shape.

Several research groups studied the dynamic behavior of DWC and FWC on rough surfaces and the removal of the condensate liquid under different body forces[122,145,146]. The use of LBM for condensation-related problems has gained momentum after Liu et al.[82,136] published their works on condensation. Since then, several authors have published their work[82,136–139] studying condensate droplet movement on smooth surfaces. The works of Li et al.[82,136] on laminar film condensation on a hydrophilic surface and dropwise condensation on a vertical hydrophobic surface are already discussed in the previous section. Li et al.[137] simulated condensation and freezing of dry saturated vapor on a hydrophobic surface. They assumed a cryogenic spot on the wall and analyzed the condensation of vapor into water or ice and their downward movement due to the gravitational force. They analyzed the influence of cold spot temperature and surface wettability on condensate droplet formation and corresponding heat flux. Li et al.[138] simulated condensation on downward facing horizontal hydrophilic surface having single or multiple hydrophobic spots. They showed that if a surface has several nucleation spots close to one another, drops growing on them merges and generate a stable film on the surface. Heat transfer rate also decreases due to this transition of dropwise condensation to filmwise condensation. Zheng et al.[139] used MRT-based hybrid thermal pseudopotential approach, to simulate condensation under the effect of gravity force. They presented several temperature contours and vector plots to discuss the detailed thermalhydraulics of droplet formation and movement.

Zhang et al.[130] studied isothermal droplet condensation on superhydrophobic nanoarrays and showed the formation of Cassie and Wenzel droplets depending on the topology of the nanopillars. Li et al.[142] used thermal multiphase LB model to study the growth of Cassie and Wenzel droplets on a rough surface with variable wettability in a gravity-free environment. Cheng et al.[147] also studied the nucleation positions and growth of Cassie and Wenzel droplets on surfaces with rough structures and mixed wettability without body force. Some other notable works are also present in the literature which deals with condensation on surfaces with roughness pillars[140,148].

All of the above research works mentioned here primarily deal with the nucleation and growth of the droplets on rough surfaces. Proper numerical analysis of the removal of the condensate liquid from structured surfaces under the influence of any kind of body force using LBM is rare, while the analysis of the droplet removal procedure is paramount in the complete understanding process of condensation heat transfer[111,122,123] .

1.4.5 Pool boiling with SRT multiphase model

The phenomenon of boiling, while being ubiquitous in nature, offers a pivotal contribution in numerous industrial and domestic activities. It facilitates substantially enhanced heat transfer rate, alongside rather a uniform temperature distribution over the heated surface with lesser fluid volume. The pool boiling, characterized by buoyancy-induced bubble motion in an initially quiescent liquid column, has enticed researchers more by the rich hydrodynamics involved. The wide disparity in thermalhydraulic characteristics across various flow regimes[6] and considerable variation in the strength of thermal communication along the heated surface has fascinated scientists across generations right from the conceptualization of the boiling curve by Nukiyama[149]. While the role of experimentation remains paramount in visual appraisal and global evaluation of pool boiling, a comprehensive local depiction solely through experiments remains elusive owing to the limitations of measuring tools, involvement of broad parametric ranges, and transitory nature of the event itself. Accordingly, the intricate process of bubble nucleation and post-departure interfacial interactions endures being confined only to empirical-level based on the experimental database. That provides an excellent opportunity for numerical exploration and consequently, several computational methods have been proposed, in the field of multiphase flow in general and boiling in particular[111,150,151], over the last few decades, with varying degree of success, ranging from macroscopic to molecular scales.

Son and Dhir[99] were apparently the first ones to propose a level-set method for simulating boiling, whereas Welch and Wilson[101] introduced Volume-of-Fluid approach. Multiple efforts are available in the literature to design a favorable amalgamation of the above two[152,153]. All such endeavors, however, suffer from one common constraint regarding the requirement of pre-existing vapor embryo or film for initiating any phase change procedure, thereby limiting their applicability while simulating the onset of nucleate boiling or transition to film boiling. That necessitates the adoption of a computational framework unrestrained by the continuum hypothesis, and the mesoscopic approach gains prominence in this particular context.

Use of SC-LBM to simulate phase change heat transfer problems has already been discussed in the previous sections. Hazi et al.[79] proposed the employment of entropy balance equation to solve the momentum-energy coupling for phase change heat transfer. Gong et al.[80] improved their model to simulate nucleate pool boiling correctly and validated the Fritz's correlationship[6]. In a follow-up work, Gong et al.[112] simulated periodic bubble nucleation, growth, and departure placing a microheater on the bottom wall in a periodic domain. They elaborated on the effect of wall superheat on heat transfer rate and bubble departure frequency. In another work[113], they studied the role of surface wettability in bubble departure and boiling regimes. They were able to procure a boiling curve for all the boiling regimes and discussed the effect of wettability on boiling curves. Li et al.[81] published their work on boiling regimes and curves where they also studied the effect of surface wettability using a hybrid approach for solving the thermal field. Ma et al.[154] also published a numerical study on boiling curves, where they described the effect of buoyancy force on boiling curves. Research works on heat transfer enhancement using structured surfaces with mixed wettability have also been reported in the literature by several authors[155–157].

All these quoted studies, however, are severely restricted in terms of the employed density ratios (around 10), renouncing the extension of the concerned conclusions to practical systems. Spurious velocity currents in the vicinity of the curved interface swell significantly with the increment of density ratio in such models, inducing oscillations in temperature profile, forcing the simulation to be unstable and unreliable. Some efforts were reported to enhance the limit of density ratio suitable to SC-LBM, such as the modified discretization scheme of Shan[39], which again is restricted to isothermal flows owing to thermodynamic inconsistencies. It is, therefore, quite evident that, despite enormous potential, the SC-LBM has primarily been restricted to low density-ratio scenarios, limiting the application in the vicinity of the critical point for any fluid. Nearly all the SRT-based algorithms are restricted to $0.85T_c$ or higher. MRT-centered approaches have breached that temperature barrier[114], albeit at the expense of substantially greater computational resources and added intricacy. That provides the necessary impetus for an endeavor, where the sole focus is on augmenting the SRT-SC-LBM algorithm to enhance the span of density ratio for pool boiling predictions.

1.5 Motivation and Research Objectives

An extensive literature survey reveals that the interparticle interaction force based phase-change heat transfer LB model has a great prospective in the simulation of boiling and condensation-related problems, yet its' potentiality is not fully utilized. Also, this method suffers from a limitation in simulating high-density ratio phase change problems due to the numerical instability stemming from the generation of spurious velocity currents in the vicinity of the two-phase interface. There are some remedies to overcome the restriction, though most of the simulations available in the literature explore problems with density ratio around the order of O(10).

Based on the literature review and identification of the research gaps, the rudimentary motivation of this work is to develop a robust in-house-code using the pseudopotential LB multiphase model, and to extend its applicability to different phase change heat transfer related problems like flow boiling, condensation, and pool boiling phenomena. With this motivation in mind, the following research objectives are specified,

- To investigate the complex thermal hydraulics of the subcooled flow boiling phenomenon keeping the primary focus on the bubble dynamics, and the characterization of the flow regimes in terms of the departure diameter and frequency as functions of input parameters, such as inlet mass flux, wall superheat and surface wettability.
- To investigate the formation of Cassie and Wenzel droplets through a temperature-controlled condensation procedure on nanostructured rough surfaces with different geometric morphology, and to study the influences of surface roughness parameters and cold spot temperature variation on the droplet growth dynamics.
- To investigate the complete growth and removal process of condensate liquid on microtextured rough surfaces with the different topology of the micropillars, and to study the effect of surface inclination on the droplet removal procedure.
- To augment the present SRT-SC-LB algorithm in a way that it can simulate phase change heat transfer problems with a larger span of density ratio, and use of the new algorithm for pool boiling related problems, such as generation of the boiling curves and study of the effect of surface wettability on boiling curves.

1.6 Thesis Outline

A brief rundown of the thesis organization is mentioned here. The first chapter is dedicated to presenting the relevant literature survey on LBM and its applicability in phase-change heat transfer problems. Accordingly, literature gaps are identified and objectives are set. The second chapter details the mathematical formulation of the pseudopotential-based LB algorithm and proposed modifications. The results of flow boiling simulation and the corresponding discussion are presented in chapter 3. Chapter 4 discusses the condensate droplet growth on nanostructured surfaces. Chapter 5 presents the results and discussion of the simulation of condensate droplet growth and removal phenomena on microstructured surfaces. The algorithmic modification of the SC-SRT-LB method and pool boiling simulation results through the application of the proposed scheme are presented in Chapter 6. Finally, the main conclusions, along with the possible directions of future research, are summarized in the last chapter.

Chapter 2

Mathematical Formulation of LBM

2.1 Introduction

The lattice Boltzmann method is a mesoscopic CFD approach originated from the kinetic theory of gas and statistical mechanics. It is a discrete computational technique based on the behavior of collection of particles known as particle distribution functions. The distribution function and its moments can be directly connected to macroscopic flow parameters. The basic idea behind the LBM is to determine the state of the distribution functions at discrete time steps in a discretized domain under the action of applied forces and to relate them with macroscopic parameters.

2.2 The Particle Distribution Function

In the lattice Boltzmann method (LBM), the fundamental variable is the particle distribution function, a probabilistic density distribution function $\left[f\left(\bar{x},\bar{c},t\right)\right]$ that represents the mass density both in physical and velocity space. To rephrase it, the distribution function $f\left(\bar{x},\bar{c},t\right)$ represents the density of particles with velocity $\bar{c}\left(c_x,c_y,c_z\right)$ at position $\bar{x}\left(x,y,z\right)$ and time t. It can be connected to the macroscopic variables through its moments which are the integrals of $f\left(\bar{x},\bar{c},t\right)$, weighted with some function of $\bar{c}$ over the entire velocity space. The macroscopic mass density can be calculated as the zeroth moment of the PDF –

$$\rho\left(\bar{x},t\right)=\iiint f\left(\bar{x},\bar{c},t\right)dc_x dc_y dc_z \tag{1}$$

The integration of the PDF over the whole velocity space represents the consideration of the contribution to the density of particles of all possible velocities at position $\bar{x}$ and time t. Macroscopic momentum density can be calculated as the first moment of the PDF as –

$$\rho\left(\bar{x},t\right)\bar{u}\left(\bar{x},t\right)=\iiint\bar{c}f\left(\bar{x},\bar{c},t\right)dc_x dc_y dc_z \tag{2}$$

In the same way, the total energy density can be calculated as –

$$\rho\left(\bar{x},t\right)E\left(\bar{x},t\right)=\frac{1}{2}\iiint\left|\bar{c}\right|^2 f\left(\bar{x},\bar{c},t\right)dc_x dc_y dc_z \tag{3}$$

In the kinetic theory of gases, the macroscopic pressure and temperature can be related to the macroscopic kinetic energy as $P=2/3nKE$ and $KE=3/2kT$, where n is the number of molecules per unit volume, and k is the Boltzmann constant. If gas is left sufficiently long to reach equilibrium, it can be assumed that the distribution function reaches an equilibrium distribution, whose expression can be found analytically from both kinetic theory and statistical mechanics. The analytical expression for the equilibrium distribution function can be written as –

$$f^{eq}\left(\bar{x},\left|\bar{u}_r\right|,t\right)=\rho\left(\frac{1}{2\pi RT}\right)^{\frac{3}{2}}e^{-\frac{\left|\bar{u}_r\right|^2}{2RT}} \tag{4}$$

where $\bar{v}$ is the relative velocity $\left(\bar{v}=\bar{\xi}-\bar{u}\right)$. This equilibrium distribution function are also written as Maxwell-Boltzmann distribution function after the name of original contributors.

2.3 The Boltzmann Transport Equation

In the lattice Boltzmann method (LBM), the fluid motion is described by the evolution of the particle distribution functions, and the basic equation that governs the evolution is known as the Boltzmann transport equation. Since the PDF f is a function of velocity $\bar{c}$, position $\bar{x}$, and time t, the total derivative of the distribution function with respect to time t can be written as –

$$\frac{df}{dt}=\left(\frac{\partial f}{\partial t}\right)\frac{dt}{dt}+\left(\frac{\partial f}{\partial x_\beta}\right)\frac{dx_\beta}{dt}+\left(\frac{\partial f}{\partial c_\beta}\right)\frac{dc_\beta}{dt} \tag{5}$$

where β indicates the specific direction of the vector. This equation can be further modified by replacing particle velocity dx_β/dt as c_β, dc_β/dt as body force F_β/ρ, and introducing a collision operator $\Omega\left(f\right)$, assuming that the distribution function evolves only through the collision phenomenon. The modified form can be written as –

$$\frac{\partial f}{\partial t}+c_{\beta}\frac{\partial f}{\partial x_{\beta}}+\frac{F_{\beta}}{\rho}\frac{\partial f}{\partial c_{\beta}}=\Omega\left(f\right) \tag{6}$$

This equation is commonly known as the Boltzmann transport equation and it is the basic governing equation of the LBM. This equation is discretized in physical space, velocity space, and time to obtain the discretized Boltzmann equation which is solved in discrete lattices and time steps.

2.4 Single Relaxation Time Model

Before going into the discretization of the Boltzmann equation, specification of the form of the collision operator is necessary. Boltzmann's original collision operator is a very complicated double integral over the velocity space, which considers all possible outcomes of two-particle collision scenarios. Bhatnagar et al. [13] proposed a very simplified form of this collision operator, which captures the relaxation of the PDF towards equilibrium PDF. This operator is known as the BGK operator after the name of the original contributors, and can be written as –

$$\Omega\left(f\right)=-\frac{1}{\tau}\left(f-f^{eq}\right) \tag{7}$$

τ is known as the relaxation time and it determines the speed of equilibration. The value of this relaxation time can be directly correlated to the transport coefficients like kinematic viscosity (υ) and thermal diffusivity (α). The Boltzmann equation, after replacing the original collision operator with the BGK operator, reads as –

$$\frac{\partial f}{\partial t}+c_{\beta}\frac{\partial f}{\partial x_{\beta}}+\frac{F_{\beta}}{\rho}\frac{\partial f}{\partial c_{\beta}}=-\frac{1}{\tau}\left(f-f^{eq}\right) \tag{8}$$

This is the final equation of the single relaxation time-based LB model, which is discretized in velocity space, physical space, and time. To begin with the discretization, the force term $\frac{F_{\beta}}{\rho}\frac{\partial f}{\partial c_{\beta}}$ is left out from Eq.(8) for ease of calculation. The whole discretization procedure is explained thoroughly in Kruger et al.[5]. The discretized equation reads as –

$$f_i\left(\overline{x}+\overline{c}_i\Delta t,t+\Delta t\right)=f_i\left(\overline{x},t\right)-\frac{\Delta t}{\tau}\left\{f_i\left(\overline{x},t\right)-f_i^{eq}\left(\rho,\overline{u},t\right)\right\} \tag{9}$$

where f_i is the PDF with velocity $\overline{c}_i$ at position $\overline{x}$ at time t, τ is the relaxation time. f_i^{eq} is the discretized form of the equilibrium particle distribution function. Actually, the velocity space is discretized in different directions forming different lattice structures. Instead of considering all directions, one considers discrete directions according to the lattice structure; i.e., particles with specific velocities $(\bar{c}_i)$ move in specific directions (i) bearing specific weights (w_i). Various lattice structures can be constructed for the one-dimensional domain(D1Q2, D1Q3), two-dimensional domain (D2Q4, D2Q5, D2Q9) and three-dimensional domain (D3Q15, D3Q19, D3Q27), and velocity sets can be constructed accordingly. The only constraint is that the velocity sets should maintain the rotational isotropy of the lattice. D2Q9 lattice is used in this work, where the particles move in nine different directions with specific velocities and weights in a two-dimensional domain. The velocity sets and corresponding weight factors are presented in Figure 1.

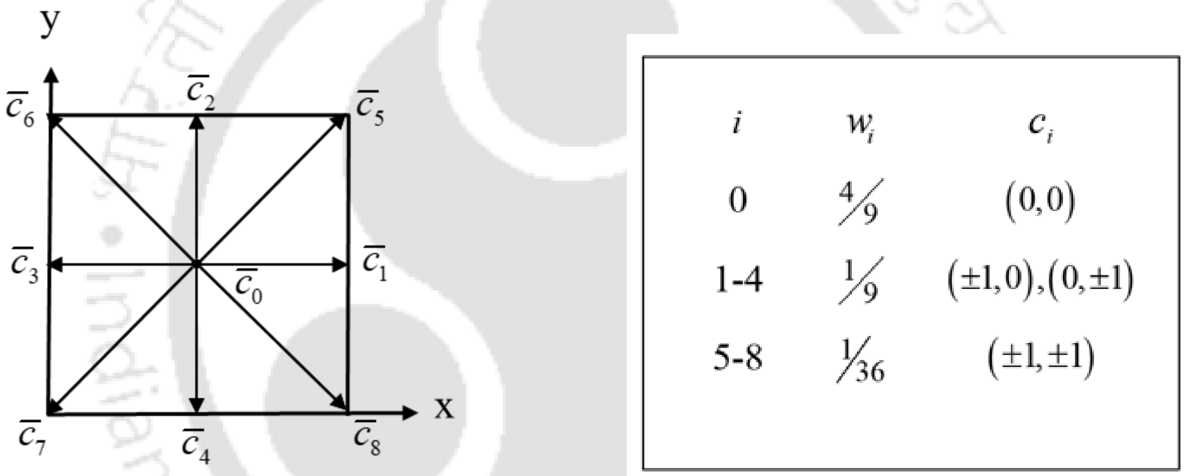

i	w_i	c_i
0	$4/9$	$(0,0)$
1-4	$1/9$	$(\pm1,0),(0,\pm1)$
5-8	$1/36$	$(\pm1,\pm1)$

(a) (b)

Fig. 1 D2Q9 lattice structure, corresponding velocity sets, and weight factors

The discretized form of the equilibrium PDF can be written as –

$$f_i^{eq}(\rho,\bar{u},t)=w_i\rho(\bar{x},t)\left[1+\frac{\bar{c}_i\cdot\bar{u}}{c_s^2}+\frac{1}{2}\frac{(\bar{c}_i\cdot\bar{u})^2}{c_s^4}-\frac{1}{2}\frac{\bar{u}^2}{c_s^2}\right] \tag{10}$$

In the two dimensional space, $\bar{c}_i$ and $\bar{c}_s$ are defined as:

$$\bar{c}_i=\frac{\Delta x}{\Delta t}\hat{i}+\frac{\Delta y}{\Delta t}\hat{j} \quad , \quad \bar{c}_s=\frac{\bar{c}_i}{\sqrt{3}} \tag{11}$$

It is already described that the mass and momentum density can be calculated through the moments of PDF [Eq (1,2)]. The same philosophy remains intact after the discretization procedure. The mass density is calculated as the summation of the distribution functions and the momentum density is calculated as the summation of the first moment of PDF.

$$\rho(\bar{x},t) = \sum f_i(\bar{x},t),\ \rho(\bar{x},t)\bar{u}(\bar{x},t) = \sum c_i f_i(\bar{x},t) \tag{12}$$

The macroscopic NSE can be recovered from the discretized LBE [Eq. 9] through Chapman-Enskong expansion upto second order of accuracy. The relaxation time can be related to the kinematic viscosity of the fluid as $\upsilon = c_s^2\left(\tau - \frac{1}{2}\right)$, and the macroscopic pressure is calculated from density values as $P = c_s^2\rho$.

2.5 Force Schemes

The incorporation of different external forces in the LB formulation is a very intriguing research topic for the past few years. In this work, interparticle interaction force, surface wettability force, and gravitational force are required to be incorporated for the simulation of different physical scenarios. All of these forces are incorporated inside a single external body force term. The body force term can be written as:

$$\bar{F}(\bar{x}) = \bar{F}^{SC}(\bar{x}) + \bar{F}^{wet}(\bar{x}) + \bar{F}^{ext}(\bar{x}) \tag{13}$$

$\bar{F}^{SC}$ is the interparticle interaction force responsible for natural phase separation. $\bar{F}^{wet}$ denotes the surface wettability force and $\bar{F}^{ext}$ represents all other external body forces. Numerous schemes are available to include the forcing term in LBE. They can be divided into three primary schemes, and all other popular schemes are derived from them. For simulating multiphase flow all these three schemes can be used for different problems.

2.5.1 Shan-Chen forcing scheme

This scheme was first proposed by Shan and Chen[158] in 1993. For this scheme, no source term has to be added in the LB equation, but the fluid velocity is modified using the external force and this modified velocity is used to calculate the equilibrium distribution function. This modified velocity is known as equilibrium velocity distribution and it is calculated as:

$$\bar{u}^{eq}(\bar{x},t) = \bar{u}'(\bar{x},t) + \bar{F}\tau/\rho \tag{14a}$$

where $\bar{u}'(\bar{x},t)=\frac{\sum \bar{c}_i f_i(\bar{x},t)}{\rho(\bar{x},t)}$. This is not the actual fluid velocity. The actual fluid velocity is calculated as:

$$\bar{u}(\bar{x},t)=\bar{u}'(\bar{x},t)+\bar{F}\Delta t/2\rho \tag{14b}$$

It must be noted that equilibrium velocity and physical velocity are not identical in this scheme. Despite having the capability of simulating high-density ratio cases for multiphase flow problems, this scheme has poor numerical accuracy.

2.5.2 Guo's forcing scheme

This scheme was proposed by Guo et al.[159] in 2002. In this scheme, a source term has to be incorporated in the LBE. The final LBE reads as:

$$f_i(\bar{x}+c_i\Delta t,t+\Delta t)=f_i(\bar{x},t)-\frac{\Delta t}{\tau}\left(f_i(\bar{x},t)-f_i^{eq}(\rho,\bar{u},t)\right)+S_i\Delta t \tag{15}$$

Where S_i is the source term, which is calculated as:

$$S_i=\left(1-\frac{\Delta t}{2\tau}\right)w_i\left(\frac{c_{i\alpha}}{c_s^2}+\frac{\left(c_{i\alpha}c_{i\beta}-c_s^2\delta_{\alpha\beta}\right)u_\beta}{c_s^4}\right)F_\alpha \tag{16a}$$

Actual fluid velocity calculated here is the same as the Shan-Chen forcing scheme -

$$\bar{u}(\bar{x},t)=\bar{u}'(\bar{x},t)+\bar{F}\Delta t/2\rho \tag{16b}$$

This scheme is more accurate than Shan-Chen forcing scheme for multiphase problems, but the density ratio achieved is lower for this scheme.

2.5.3 EDM forcing scheme

Exact difference method (EDM) is another scheme used to include force in LBE. This scheme was first proposed by Kuperstokh et al.[44] in 2006 to simulate the effect of the electric field in a fluid flow problem. In this scheme, a source term is added in the LBE as the previous one, and the LBE reads as:

$$f_i(\bar{x}+c_i\Delta t,t+\Delta t)=f_i(\bar{x},t)-\frac{\Delta t}{\tau}\left(f_i(\bar{x},t)-f_i^{eq}(\rho,\bar{u},t)\right)+S_i \tag{17}$$

But, the source term calculation is different here. The source term can be calculated as –

$$S_i = f_i^{eq}\left(\rho, \bar{u}' + \Delta\bar{u}\right) - f_i^{eq}\left(\rho, \bar{u}\right) \tag{18a}$$

where $\bar{u}'\left(\bar{x},t\right) = \dfrac{\sum \bar{c}_i f_i\left(\bar{x},t\right)}{\rho\left(\bar{x},t\right)}$ and $\Delta\bar{u} = \dfrac{\bar{F}\Delta t}{\rho}$. The actual fluid velocity is calculated as the previous scheme.

$$\bar{u}\left(\bar{x},t\right) = \bar{u}'\left(\bar{x},t\right) + \bar{F}\Delta t \big/ 2\rho \tag{18b}$$

According to Gong et al. [45], EDM is the best forcing scheme for simulating thermal multiphase flow problems.

2.6 MRT Method

Relaxing the discrete populations with individual relaxation rates instead of using the same relaxation time for all populations can provide better numerical stability and accuracy. Populations are transformed into the moment space from the velocity space using a transformation matrix $\left[M\right]$ in the MRT model, where the collision step is performed. Post-collision populations are transformed back to the physical velocity space using the inverse of the transformation matrix $\left[M^{-1}\right]$, and streaming operation is executed. The use of the MRT model in combination with the pseudopotential multiphase model offers much better numerical stability and simulations can be performed at higher density ratios in comparison to the single relaxation time model. The MRT LBE reads as:

$$f_i\left(\bar{x} + \bar{c}_i\Delta t, t + \Delta t\right) = f_i\left(\bar{x},t\right) - \bar{M}^{-1}\bar{S}_m\bar{M}\left[f_i\left(\bar{x},t\right) - f_i^{eq}\left(\rho,\bar{u},t\right)\right]\Delta t + F_i\left(\bar{x},t\right)\Delta t \tag{19a}$$

$\bar{M}$ in Eq. (19a) is the orthogonal transformation matrix, which transforms the particle distribution functions from velocity space to moment space. It is defined as:

$$\bar{M}=\begin{bmatrix} 1 & 1 & 1 & 1 & 1 & 1 & 1 & 1 & 1 \\ -4 & -1 & -1 & -1 & -1 & 2 & 2 & 2 & 2 \\ 4 & -2 & -2 & -2 & -2 & 1 & 1 & 1 & 1 \\ 0 & 1 & 0 & -1 & 0 & 1 & -1 & -1 & 1 \\ 0 & -2 & 0 & 2 & 0 & 1 & -1 & -1 & 1 \\ 0 & 0 & 1 & 0 & -1 & 1 & 1 & -1 & -1 \\ 0 & 0 & -2 & 0 & 2 & 1 & 1 & -1 & -1 \\ 0 & 1 & -1 & 1 & -1 & 0 & 0 & 0 & 0 \\ 0 & 0 & 0 & 0 & 0 & 1 & -1 & 1 & -1 \end{bmatrix} \tag{19b}$$

$\bar{S}_m$ is the diagonal matrix containing the values for different relaxation times in the moment space - $\bar{S}_m=\left(\tau_0,\tau_1,\tau_2,\tau_3,\tau_4,\tau_5,\tau_6,\tau_7,\tau_8\right)^T$. Among these relaxation time parameters, τ_7 and τ_8 are directly related to the kinematic viscosity of the fluid according to the relation - $\left(\tau_7=\tau_8=3\upsilon+0.5\right)$. The RHS of Eq. (19a) can be rewritten as –

$$\bar{m}^*=\bar{m}-\bar{S}_m\left(\bar{m}-\bar{m}^{eq}\right)\Delta t+\Delta t\left(\bar{I}-\frac{\bar{S}_m}{2}\right)\bar{S} \tag{20a}$$

where $\bar{m}=\bar{M}f$, $\bar{m}^{eq}=\bar{M}f^{eq}$, $\bar{I}$ is the unit tensor, and $\bar{S}$ is the forcing term $\left[\bar{M}\bar{F}=\left(\bar{I}-\frac{\bar{S}_m}{2}\right)\bar{S}\right]$ for calculation in the moment space. Accordingly, populations in the new time step can be found as –

$$f_i\left(\bar{x}+\bar{c}_i\Delta t,t+\Delta t\right)=\bar{M}^{-1}\bar{m}^* \tag{20b}$$

The fluid velocity $\bar{u}$ is calculated as[5]:

$$\bar{u}\left(\bar{x},t\right)=\sum f_i\left(\bar{x},t\right)c_i+\bar{F}\Delta t\big/2\rho \tag{21}$$

where $\bar{F}$ is the total external force acting on the fluid. Following the work of Li et al.[48], an improved thermodynamically consistent form of Guo's[159] forcing scheme is used in this work. The forcing term inside the moment space $\bar{S}$ can be written as –

$$\bar{S} = \begin{bmatrix} 0 \\ 6\left(u_x F_x + u_y F_y\right) + \dfrac{\sigma_m \left|F^{sc}\right|^2}{\psi^2 \Delta t\left(\tau_7 - \frac{1}{2}\right)} \\ -6\left(u_x F_x + u_y F_y\right) - \dfrac{\sigma_m \left|F^{sc}\right|^2}{\psi^2 \Delta t\left(\tau_7 - \frac{1}{2}\right)} \\ F_x \\ -F_x \\ F_y \\ -F_y \\ 2\left(u_x F_x - u_y F_y\right) \\ u_x F_y + u_y F_x \end{bmatrix} \tag{22}$$

where σ_m is a parameter to tune the mechanical stability[48] of the simulation. In this work, the value of this tuning parameter is assumed to be $\sigma_m = 0.103$ to achieve the best results.

2.7 Pseudopotential Model

Shan and Chen proposed their interparticle interaction force based multiphase model in 1993 [10]. The underlying idea of this model is to introduce a simple interaction force defined between lattice nodes which can be used to model both multiphase and multicomponent flows with or without surface tension.

To find a functional form of the interaction force, it is assumed that the intermolecular forces act between sets of molecules and are additive. As a consequence, a higher density of molecules leads to a stronger force. The magnitude of the interaction between fluid elements at $\tilde{x}$ (on this lattice node the SC force is being calculated) and $\bar{x}$ (neighboring nodes) will be proportional to $\rho(\bar{x})\rho(\tilde{x})$. The force will also be a strong function between molecules and total force must be calculated by integrating all the forces in all directions. So, the final form of interaction force can be written as:

$$\bar{F}^{sc}(\bar{x}) = -\int(\bar{x}-\tilde{x})G(\bar{x},\tilde{x})\psi(\bar{x})\psi(\tilde{x})d^3\tilde{x} \tag{23}$$

In this equation, the local fluid density ρ is replaced by the effective density function ψ, which is called the pseudopotential function. The reason to introduce this pseudo density instead of using the original density is to eliminate the numerical instability. A very popular form of the pseudopotential is[5,37] –

$$\psi(\rho) = \rho_0\left[1 - \exp\left(\rho \big/ \rho_0\right)\right] \qquad (24)$$

Where ρ_0 is generally taken as 1. The form of the force presented in Eq. (23) is the analytical form of the SC force, which has to be discretized before using in LBE. The simplest form of discretized SC force for a single component fluid is represented as the sum of pseudopotential interaction of the nearest lattice neighbors is [22] –

$$\bar{F}^{sc}(\bar{x}) = -\psi(\bar{x})G\sum_i w_i\psi(\bar{x} + c_i\Delta t)c_i\Delta t \qquad (25)$$

where $G(\bar{x},\tilde{x}) = w_i G$ for $\tilde{x} = \bar{x} + c_i\Delta t$ and otherwise its value is zero. $\psi(\bar{x})$ is known as the pseudopotential function and calculated from the densities of the local lattice nodes. For $D2Q9$ lattice $w(|\bar{c}_i|)$ is given as :

$$w(|\bar{c}_i|) = \begin{cases} w_1 & \text{if} \quad |\bar{c}_i| = \bar{c} \\ w_2 & \text{if} \quad |\bar{c}_i| = \sqrt{2}\bar{c} \\ 0 & \text{otherwise} \end{cases} \qquad (26)$$

with constraint $w_1 = 4w_2$ coming from the weight factors of different velocity space directions of $D2Q9$ lattice, which are the same as the weight factors provided in Fig.1^5. The sum runs over all velocities c_i of the underlying lattice and w_i is the weight factor. This force is incorporated into the LB equation using different force schemes.

2.7.1 Maxwell area construction rule

Ideally, for multiphase systems, the multiphase force should have a thermodynamically consistent form, i. e. the pressure and the equilibrium densities for a given temperature should be the same as those derived from thermodynamic principles using the Maxwell area construction rule. The physical requirement of having coexistence of phases puts a constraint on the equation of state, which describes the complex interdependency between pressure, density, and temperature.

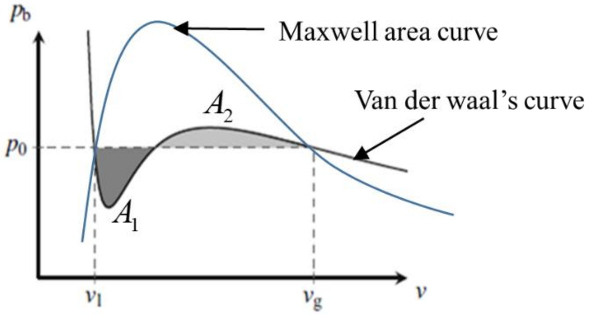

Fig. 2 Maxwell area construction rule for Van-der Waals equation of state

There are several equations of state (EOS) used to explain the behavior of coexisting phases of a fluid. The generic pressure-volume curve for the famous Van-der Waals(VdW) EOS is plotted in Fig. 2 to explain the Maxwell area construction rule. It can be seen from the figure, that there is a range of pressures for which two distinct molar volumes can be adopted for the same bulk pressure p_b, for a fixed temperature. The Maxwell area construction rule postulates that, for a given temperature, the liquid-vapor co-existence happens at a pressure p_0 such that both the shaded areas in the figure are identical. It can be represented mathematically as:

$$\int_{v_l}^{v_g} \left(p_0 - p_b \left(v, T \right) \right) dv = 0 \tag{27}$$

The molar volumes of gas and liquid should satisfy –

$$p_0 = p_b \left(v_g, T \right) = p_b \left(v_l, T \right) \tag{28}$$

Any model for the equation of state that satisfies the above constraint is thermodynamically consistent. A curve plotted by joining all the points satisfying the Maxwell area rule is known as the Maxwell curve, which is represented by the blue line in Fig. 2. As the molar specific volumes are obtained analytically, liquid and vapor densities are also known analytically for a particular temperature, which should agree with the densities obtained from the numerical method used to model a multiphase flow situation. When the coexisting densities of a fluid at a particular temperature agree well with the analytical values, the model is said to be thermodynamically consistent.

2.7.2 Shan-Chen EOS

If the pseudopotential function of the neighboring nodes $\left[\psi\left(\bar{x}+c_i\Delta t\right)\right]$ is expanded using Taylor's series expansion, and the expanded form is substituted into the discretized SC force form [Eq. (25)], the following equation can be obtained –

$$\bar{F}^{SC}\left(\bar{x}\right)=-G\psi\left(\bar{x}\right)\sum_i w_i c_i \Delta t\left[\psi\left(\bar{x}\right)+c_{i\alpha}\Delta t\partial_\alpha\psi\left(\bar{x}\right)+\frac{1}{2}c_{i\alpha}c_{i\beta}\Delta t^2\partial_\alpha\partial_\beta\psi\left(\bar{x}\right)+.....\right] \tag{29a}$$

To maintain the isotropy of a lattice discretized into velocity space, velocity sets must obey some symmetry conditions, which can be written as –

$$\sum_i w_i = 1 \tag{29b}$$

$$\sum_i w_i c_{i\alpha} = 0 \tag{29c}$$

$$\sum_i w_i c_{i\alpha} c_{i\beta} = c_s^2 \delta_{\alpha\beta} \tag{29d}$$

$$\sum_i w_i c_{i\alpha} c_{i\beta} c_{i\gamma} = 0 \tag{29e}$$

Including expansion terms upto third order from Eq. 29(a), and using the velocity symmetry set conditions [29(b)-29(e)], the following continuum form of the SC force can be obtained –

$$\bar{F}^{SC}\left(\bar{x}\right)=-G\psi\left(\bar{x}\right)\left[c_s^2\Delta t^2\nabla\psi\left(\bar{x}\right)+\frac{c_s^4\Delta t^4}{2}\nabla\left\{\Delta\psi\left(\bar{x}\right)\right\}\right] \tag{29f}$$

The first term of Eq. 29(f) contributes to forming the SC non-ideal equation of state, while the second term takes care of the interfacial surface tension force[5]. The final form of the SC non-ideal equation of state can be written as –

$$p_b\left(\rho\right)=c_s^2\rho+\frac{c_s^2\Delta t^2 G}{2}\psi^2\left(\rho\right) \tag{30}$$

A careful observation of this equation of state [Eq. (30)] reveals that it has no properly defined temperature parameter, though it is possible to define a temperature like parameter $\left(T=-1/G\right)$ controlling the phase separation process. At critical points, the first and second derivative of pressure with respect to density is zero. Using these two derivative constraints on SC EOS, the critical properties can be found as - $\rho_c=\rho_0\ln 2$ and $G_c=-2/9\rho_0$. The absence of a properly defined temperature parameter makes the model unsuitable for the simulation of thermal multiphase flow problems. Due to the lack of a proper temperature parameter in the SC EOS, specific densities at specified temperatures cannot be obtained. Hence, the Maxwell area construction rule can never be satisfied leading to a thermodynamically inconsistent model.

2.7.3 Modifications for the simulation of phase change heat transfer

Yuan et al. [4] devised a new method for the incorporation of realistic EOS in calculating the pseudopotential. From Eq. (30), $\psi(\bar{x})$ can be written as :

$$\psi(\rho)=\sqrt{\frac{2\left(p_b-c_s^2\rho\right)}{c_s^2\Delta t^2\left|G\right|}} \tag{31}$$

In Eq. (31), the bulk pressure p_b can be replaced with any realistic equation of state used to calculate the liquid-vapor phase coexistence values experimentally. The Peng-Robinson (PR) equation of state is the most accurate cubic equation of state to calculate the liquid and vapor densities inside the vapor dome [45]. It is written as:

$$p_b=\frac{\rho RT}{1-b\rho}-\frac{a\alpha(T)\rho^2}{\left(1+2b\rho-b^2\rho^2\right)} \tag{32}$$

where $\alpha(T)=\left[1+\left(0.37464+1.54226\omega-0.26992\omega^2\right)\times\left(1-\sqrt{T/T_c^2}\right)\right]^2$

$$a=0.45724\,R^2T_c^2/p_c \quad \text{and} \quad b=0.0778\,RT_c/p_c$$

Here ω is known as the ascentric factor which is different for different fluids. Following the work of Yuan et. al [4], the values of a and b are taken as $2/49$ and $2/21$ respectively. Value of the universal gas constant at lattice level is taken as $R=1$. The critical temperature (T_c), pressure(p_c) and density(ρ_c) can be calculated from the derivative constraints and using the value of a, b and R. To relate the non-dimensional values with physical properties, reduced properties are used as written below.

$$\rho_R=\frac{\rho}{\rho_C}\ , \qquad T_R=\frac{T}{T_C}\ , \qquad p_R=\frac{p}{p_C} \tag{33}$$

Subscripts R and C denotes the reduced and critical properties. According to the law of corresponding states, the reduced properties should be the same irrespective of the units used. Unit conversion can be written as:

$$\rho_R = \frac{\rho^{lu}}{\rho_C^{lu}} = \frac{\rho^{real}}{\rho_C^{real}} \;, \qquad T_R = \frac{T^{lu}}{T_C^{lu}} = \frac{T^{real}}{T_C^{real}} \;, \qquad p_R = \frac{p^{lu}}{p_C^{lu}} = \frac{p^{real}}{p_C^{real}} \tag{34}$$

It can be concluded from the work of Yuan et al. [4] that the use of realistic EOS instead of SC EOS can render the original SC model thermodynamically consistent inside a wide temperature range. Beyond that temperature range, coexisting densities for specified temperatures do not match with the analytical values obtained from the Maxwell area construction curve. For PR EOS, the temperature below which the coexisting densities start to mismatch with the analytical results is $T_R = 0.9$.

Gong et al. [45] proposed a new form of the original interparticle interaction force which helps the modified SC model to achieve better thermodynamic consistency. According to the work of Gong et al. [80], the new structure of the interaction force is written as:

$$\bar{F}(\bar{x}) = -G\sum_i w(|\bar{c}_i|)\left[\beta\psi(\bar{x})\psi(\bar{x}+\bar{c}_i\Delta t) + \left(\frac{1-\beta}{2}\right)\psi^2(\bar{x}+\bar{c}_i\Delta t)\right]\bar{c}_i\Delta t \tag{35}$$

where β is a weighting factor associated with a particular EOS. They showed that $\beta = 1.16$ is the optimum value for PR EOS to achieve the best results.

The surface wettability force is also calculated by using the pseudopotential function. Benzi et. al. [160] proposed a very simple model to incorporate the surface wettability force for a single component multiphase fluid and solid wall. The desired contact angle is obtained by changing a parameter ρ_w, which represents the fluid density at the solid wall. The parameter ρ_w is known as false wall density in LB literature[5]. The adhesion force between the vapor/liquid phase and the solid wall is calculated by the following expression given below:

$$\bar{F}^{ads}(\bar{x}) = -G\psi(\bar{x})\sum w_i\psi(\rho_w)S_{ind}(\bar{x}+\bar{c}_i\Delta t)\bar{c}_i\Delta t \tag{36a}$$

An indicator function S_{ind} as appearing in Eq. (36) is used to denote the solid and fluid nodes. Note that the indicator function takes a value 1 for a solid node and helps to calculate the adhesive force. On the other hand, this function becomes 0 when it is a fluid node.

Gravitational force is also required as an external force in this work. Calculation of the gravitational force is slightly different for boiling and condensation problems. Following the work of Kang et al.[161], the gravitational force for boiling related problems (where vapor bubble moves through liquid) can be calculated as:

$$\bar{F}^{g}\left(\bar{x},t\right)=g_{a}\left(1-\frac{\rho_{avg}\left(t\right)}{\rho\left(\bar{x},t\right)}\right) \tag{36b}$$

The calculation procedure of the gravitational force is slightly different for the case of condensation, where liquid droplet moves through vapor. The gravitational force can be calculated following the work of Liu et al.[82] as:

$$\bar{F}^{g}\left(\bar{x},t\right)=g_{a}\left(\rho\left(\bar{x},t\right)-\rho_{vap}\left(t\right)\right) \tag{36c}$$

2.7.4 Proposed thermal multirange pseudopotential model

Despite having several advantages over the conventional approaches, the thermal multiphase LB model fails to simulate phase change problems in the practical density ratio range[O(10^3)]. The multiphase simulations using this LB approach are unstable and inaccurate at very high density ratio range. It is imperative to know the reasons behind this failure, which in turn will help to devise proper techniques to remove the shortcomings of the present model. Numerous research groups have worked[41,162,163] on this issue over the past decade and proposed some modifications. According to them, one of the major drawbacks of the SC multiphase model is the existence of spurious currents in the vicinity of the curved interface between the two coexisting phases. For a standard static droplet problem, where a droplet is placed inside the bulk vapor phase in a periodic domain, the velocity at all lattice nodes should be zero after the situation becomes steady. In contrast to this zero-velocity steady situation, in reality, small velocity currents exist in the domain and their value becomes higher near the curved interface. It is reported in the literature [41,162] that the false velocity currents form due to insufficient isotropy of the discretized form of the SC force term. Spurious velocity increases with the increment in the density ratio and subsequently, the simulation becomes numerically unstable. In the case of phase-change heat transfer simulations, due to the spurious velocity fluctuation at the interface, fluid temperature also oscillates at the interface erratically, which makes the simulation inaccurate and unstable at higher density ratios. If RHS of the SC force term in Eq. (25) is expanded according to the rule of n-dimensional Taylor series expansion upto 10th order, the expanded expression reads as:

$$\bar{F}(\bar{x}) = -G\psi(\bar{x})\Delta t \begin{bmatrix} E^{(2)}_{ij}\partial_j\psi + \frac{1}{3!}E^{(4)}_{ijkl}\partial_{jkl}\psi + \frac{1}{5!}E^{(6)}_{ijklmn}\partial_{jklmn}\psi \\ +\frac{1}{7!}E^{(8)}_{ijklmnpq}\partial_{jklmnpq}\psi + \frac{1}{9!}E^{(10)}_{ijklmnpqrs}\partial_{jklmnpqrs}\psi + \dots\dots\dots \end{bmatrix} \tag{37a}$$

where

$$E^{(n)} = E^{(n)}_{i_1 i_2 i_3 i_4 \dots\dots i_n} = \sum_i w\left(\left|\bar{c}_i\right|\right) c_{i_1} c_{i_2} c_{i_3} c_{i_4} \dots\dots\dots c_{i_n} \tag{37b}$$

Odd order tensorial terms are not included in the Eq. (37a) as they must possess zero value to satisfy the requirement of sufficient rotational isotropy of the $D2Q9$ lattice structure and velocity sets [Eq. 29(b)-(e)]. In mathematical terms, for an n-dimensional case, this condition can be written as:

$$E^{(2n+1)} = E^{(2n+1)}_{i_1 i_2 i_3 i_4 \dots\dots i_n} = \sum_i w\left(\left|\bar{c}_i\right|\right) c_{i_1} c_{i_2} c_{i_3} c_{i_4} \dots\dots\dots c_{i_{2n+1}} = 0, \qquad n \geq 0 \tag{38}$$

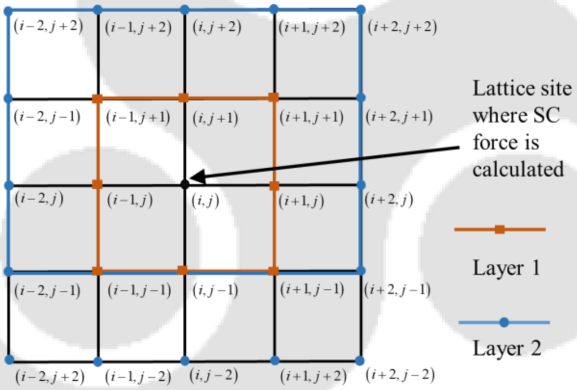

Fig. 3 Discretization schemes for different schemes – layer 1 points consider eight neighboring points for discretization. Consideration of both layer 1 and 2 for neighboring and next neighboring nodes respectively makes the scheme twenty five point scheme, which reduces the spurious current in the simulation results.

Shan [162] explained that considering only upto the 4th order terms $\left(E^{(4)}\right)$ of RHS of Eq. (37a) in the discretized form of the SC force includes only the next neighboring nodes (layer 1 of Fig. 3) and anisotropy stems from the first truncated term (the original form of the SC force), which happens to be the 6th order term $\left(E^{(6)}\right)$. But, if higher-order terms are included in the calculation of the force term, isotropy of the discretized force term increases. Hence, spurious velocity currents decrease and consequently, high density ratio simulation can be performed. The required coefficients for the higher-order discretization are calculated by Shan [162] and presented in Table 1.

A new form of discretization of the interparticle interaction force is proposed in this work, where the force scheme of Gong et al.[45] is modified with Shan's[162] idea of using more neighboring points for discretization. The proposed model enjoys the benefits of both previous models, as the discretized force form has better isotropy along with thermodynamic consistency. In this model, the modified form of SC force (Eq. 35) is taken, and instead of considering only the next neighboring nodes, another layer of neighboring points [layer 2 in Fig. 3] is used to calculate the force term. The new structure of the original SC force term can be expressed as:

$$\begin{aligned}\bar{F}(\bar{x}) = -G\beta\psi(\bar{x})\Delta t &\begin{bmatrix} E_{ij}^{(2)}\partial_j\psi(\bar{x}+\bar{c}_i\Delta t) + \frac{1}{3!}E_{ijkl}^{(4)}\partial_{jkl}\psi(\bar{x}+\bar{c}_i\Delta t) \\ +\frac{1}{5!}E_{ijklmn}^{(6)}\partial_{jklmn}\psi(\bar{x}+\bar{c}_i\Delta t) + \frac{1}{7!}E_{ijklmnpq}^{(8)}\partial_{jklmnpq}\psi(\bar{x}+\bar{c}_i\Delta t)\end{bmatrix} \\ -G\beta\Delta t &\begin{bmatrix} E_{ij}^{(2)}\partial_j\psi^2(\bar{x}+\bar{c}_i\Delta t) + \frac{1}{3!}E_{ijkl}^{(4)}\partial_{jkl}\psi^2(\bar{x}+\bar{c}_i\Delta t) \\ +\frac{1}{5!}E_{ijklmn}^{(6)}\partial_{jklmn}\psi^2(\bar{x}+\bar{c}_i\Delta t) + \frac{1}{7!}E_{ijklmnpq}^{(8)}\partial_{jklmnpq}\psi^2(\bar{x}+\bar{c}_i\Delta t)\end{bmatrix} + O(\partial^9)\end{aligned} \tag{39}$$

In this new form, the required coefficients for the discretization remain the same as presented in Table 1 (presented in appendix section). The whole form of the discretized force for D2Q9 lattice is presented in Appendix A. It can be seen from the expression of Eq. (39) that upto 8th order terms are considered for the discretization purpose. So the first truncated term is:

$$\begin{aligned}T_e = -G\beta\psi(\bar{x})\Delta t&\left[\frac{1}{9!}E_{ijklmnpqrs}^{(10)}\partial_{jklmnpqrs}\psi(\bar{x}+\bar{c}_i\Delta t)\right] \\ -G\beta\Delta t&\left[\frac{1}{9!}E_{ijklmnpqrs}^{(10)}\partial_{jklmnpqrs}\psi^2(\bar{x}+\bar{c}_i\Delta t)\right]\end{aligned} \tag{40}$$

In the modified structure of the force term proposed by Gong et al. [45], only upto 4th order terms are considered for the discretization and anisotropy stems from the 6th order terms. In comparison to that, this new form of discretization offers much higher isotropy by considering terms upto 8th order and smaller amount of anisotropy comes from the neglected 10th order term. As a consequence, spurious velocity becomes smaller and higher density ratio thermal multiphase flow simulations can be performed.

2.8 Energy Equation

DDF approach for solving the energy field is used in this work. In this approach, a second distribution function is defined for the temperature field and the thermal LBE using the temperature distribution function reads as:

$$g_i\left(\bar{x}+\bar{c}_i\Delta t,t+\Delta t\right)=g_i\left(\bar{x},t\right)-\frac{\Delta t\left[g_i\left(\bar{x},t\right)-g_i^{eq}\left(\bar{\mathrm{x}},t\right)\right]}{\tau_g} \tag{41}$$

The equilibrium temperature distribution function g_i^{eq} is written as:

$$g_i^{eq}=w_iT\left(\bar{x},t\right)\left[1+\frac{\bar{c}_i\cdot\bar{u}}{c_s^2}+\frac{1}{2}\frac{\left(\bar{c}_i\cdot\bar{u}\right)^2}{c_s^4}-\frac{1}{2}\frac{\left(\bar{u}\right)^2}{c_s^2}\right] \tag{42}$$

In this case, the temperature and thermal diffusivity are defined as:

$$T_i\left(\bar{x},t\right)=\sum_i g_i\left(\bar{x},t\right) \qquad \alpha_T=c_s^2\left(\tau_g-\frac{1}{2}\right) \tag{43}$$

Hazi et al.[77] proposed the incorporation of a source term (ϕ) in the LBE to accommodate the liquid-vapor phase change phenomenon.

$$g_i\left(\bar{x}+\bar{c}_i\Delta t,t+\Delta t\right)=g_i\left(\bar{x},t\right)-\frac{\Delta t\left[g_i\left(\bar{x},t\right)-g_i^{eq}\left(\bar{x},t\right)\right]}{\tau_g}+w_i\Delta t\phi\left(\bar{x},t\right) \tag{44}$$

According to Hazi et al. [79], using the macroscopic energy equation and thermodynamic Tds equations, the source term is derived as:

$$\phi=\frac{T}{\rho^2c_v}\left(\frac{\partial p}{\partial T}\right)_\rho\frac{d\rho}{dt}+T\nabla\cdot\bar{u} \tag{45}$$

where $\left(\frac{\partial p}{\partial T}\right)_\rho$ is calculated directly from the corresponding EOS. It may be mentioned here that the temporal density gradient is inconvenient from the perspective of numerical implementation. To simplify the numerical implementation and decrease the computational cost, a relatively simple form is derived using the basic mass conservation equation (the continuity equation) by Gong et [80] al. The modified source term is calculated as:

$$\phi = T\left[1-\frac{1}{\rho c_v}\left(\frac{\partial p}{\partial T}\right)_{\rho}\right]\nabla\cdot\bar{u} \tag{46}$$

A second-order central difference scheme is used to calculate the divergence of velocity and temporal gradient of density. Thus, the liquid–vapor phase change process can be simulated by combining the modified pseudo-potential model for multiphase flows and the energy equation model. Relevant properties like thermal conductivity and viscosity at the liquid-vapor interface are estimated employing a linear interpolation, which helps avoid steep property gradients at the interface, resulting in a diffused-interface representation.

$$\varphi = \varphi_{liq}\frac{\rho-\rho_{vap}}{\rho_{liq}-\rho_{vap}} + \varphi_{vap}\frac{\rho_{liq}-\rho}{\rho_{liq}-\rho_{vap}} \tag{47}$$

MRT-based energy equation can also be adopted for better numerical stability and accuracy. The governing MRT-LB energy equation can be written as:

$$g_i\left(\bar{x}+\bar{c}_i\Delta t, t+\Delta t\right) = g_i\left(\bar{x},t\right) - \bar{M}^{-1}\bar{S}_T\bar{M}\left(g_i - g_i^{eq}\right)\Delta t + \omega_i\phi\left(\bar{x},t\right)\Delta t \tag{48}$$

The orthogonal transformation matrix $\bar{M}$ is the same as Eq. (20). $\bar{S}_T$ is the diagonal matrix containing the relaxation factors in moment space for collision[114] - $\bar{S}_T = \left(\tau_0^e, \tau_1^e, \tau_2^e, \tau_3^e, \tau_4^e, \tau_5^e, \tau_6^e, \tau_7^e, \tau_8^e\right)^T$. Here τ_3^e and τ_5^e are related to the macroscopic thermal diffusivity (α_T) as: $\left(\tau_3^e = \tau_5^e = 3\alpha_T + 0.5\right)$. Equilibrium particle distribution function, temperature, and the source term for phase change are calculated in the same way as the SRT model.

2.9 Boundary Conditions

Since LB method is a mesoscopic approach and its boundary conditions are not originated directly from the physical macroscopic equations, simulating the boundary phenomena has been an important research topic for the past thirty years. The boundary conditions used in this work in different physical scenarios are described in detail in the present section.

2.9.1 Bounceback condition

Bounceback condition is a very popular boundary condition used for no-slip walls. The basic working principle for bounceback scheme is that the populations hitting the rigid wall during propagation are reflected back to their original location. If x_b is considered as boundary node and populations propagating from boundary nodes at time t, then the bounceback scheme can generally be represented as:

$$f_i\left(\overline{x}_{bo}, t+\Delta t\right) = f_{i,opposite}\left(\overline{x}_{bo}, t\right) \tag{49}$$

where $f_{i,opposite}\left(\overline{x}_{bo}, t\right)$ represents the opposite direction population of a particular population. As soon as the missing populations are known in this way, macroscopic variables like velocity and density can be calculated very easily.

2.9.2 Periodic condition

This kind of boundary conditions can only be applied to those situations where the flow is periodic, and they state that flow leaving from one side will enter through the opposite side instantaneously. As a consequence, mass and momentum are conserved while using the periodic boundary conditions. Implementation of periodic boundary conditions is very simple in LBM. During propagation, the unknown particle distribution functions on one side are swapped by those leaving the domain from the opposite side. Mathematically, the periodic boundary condition can be represented as –

$$f_i\left(\overline{x}, t+\Delta t\right) = f_i\left(\overline{x}+L, t\right) \tag{50}$$

Where $f_i\left(\overline{x}+L, t\right)$ represents the population leaving from other side for a domain length L.

2.9.3 Non-equilibrium bounceback condition

The non-equilibrium bounce back approach was first used by Zou and He[164] in 1996. This can be applied for both inlet velocity conditions or constant pressure boundary conditions. The basic principle of this boundary condition is to assume that the non-equilibrium distribution part of the normal population at a boundary node is bounced back from the boundary, and using this assumption velocity and density fields are calculated. Afterward, from the known velocity and density fields, unknown populations are calculated. For the incompressible LB method, the relation between pressure and density is linear $\left(p = c_s^2\rho\right)$. So, the known pressure boundary condition can be replaced by known density at the boundary in incompressible LBM. As an example, if the bottom surface of a domain is considered, after the streaming process, six populations $\left(f_0, f_1, f_3, f_4, f_7, f_8\right)$ are known and the other three populations $\left(f_2, f_5, f_6\right)$ are unknown. Now, using Eq. (12), three separate equations can be written for the distribution functions:

$$f_2 + f_5 + f_6 = \rho - \left(f_0 + f_1 + f_3 + f_7 + f_4 + f_8 \right) \tag{51a}$$

$$\rho u_x = f_1 - f_3 + f_8 - f_7 + f_5 - f_6 \tag{51b}$$

$$\rho u_y = f_2 - f_4 + f_5 - f_7 + f_6 - f_8 \tag{51c}$$

where u_x and u_y are the velocity in x and y direction. Now, if the density is unknown, we get three equations for four unknowns ρ, f_2, f_5, f_6. To close the system, it is assumed that the non-equilibrium part$\left(f^{neq} = f - f^{eq} \right)$ of PDF normal to the boundary is bounced back. This can be written in equation form as:

$$f_2 - f_2^{eq} = f_4 - f_4^{eq} \tag{51d}$$

Now, considering eq. (51), there are four separate algebraic equations are present for four unknowns. After some algebraic manipulations, the four unknowns can be written as functions of known terms as:

$$\rho = \frac{1}{1-u_y}\left[f_0 + f_1 + f_3 + 2\left(f_4 + f_7 + f_8 \right) \right] \tag{52a}$$

$$f_4 = f_2 + \frac{2}{3}\rho u_y \tag{52b}$$

$$f_5 = f_7 - \frac{1}{2}\left(f_1 - f_3 \right) + \frac{1}{2}\rho u_x + \frac{1}{6}\rho u_y \tag{52c}$$

$$f_6 = f_8 + \frac{1}{2}\left(f_1 - f_3 \right) - \frac{1}{2}\rho u_x + \frac{1}{6}\rho u_y \tag{52d}$$

It is worth mentioning here, that the collision operation should be done on the boundary nodes while using this boundary scheme. The same technique can be applied for other sides of a domain, where the unknown populations are different from this one. In the same way, calculation of unknown populations can be done, when the velocity of a specific boundary is known. This boundary scheme is applied for all the open boundaries in this work.

2.9.4 Thermal boundary condition

Anti-bounceback scheme is used as the thermal boundary condition throughout this work. This boundary condition can be used when the boundary temperature is known. If the wall temperature is T_W, the anti bounceback scheme can be written as –

$$g_i\left(\bar{x}_{bo}, t+\Delta t\right) = -g_{i,opposite}\left(\bar{x}_{bo}, t\right) + 2w_i T_W \qquad (53)$$

For constant heat flux boundary conditions, simple FDM is used to calculate the boundary temperature first, and then the temperature value is used in Eq.(53). If q_w is the wall heat flux, wall temperature can be calculated as -

$$T_W = T_{neighbor} + \frac{q_W \Delta x}{k} \qquad (54)$$

Here k is the thermal conductivity, $T_{neighbor}$ is the temperature of the neighboring node to the wall inside the domain, and Δx is the lattice thickness.

2.10 Lattice Boltzmann Algorithm

The algorithm for the LB simulation requires initialization of the macroscopic parameters for the whole flow field, and calculation of PDF and equilibrium PDF accordingly. After initialization, collision and propagation operations are performed for the momentum equation. Once the propagation step is completed, calculations of unknown populations at boundaries using appropriate boundary conditions are executed and macroscopic flow variables are calculated. The source term for the energy equation is calculated next, using which post-collision populations for the energy equation are calculated. Subsequently, streaming, application of boundary conditions, and macroscopic temperature calculation are performed. Once all macroscopic variables in the domain are known, SC force is calculated, which will be used in the next collision step for momentum. Repetitions of these operations are done at each time step until the required results are obtained. A flowchart for the complete algorithm is presented in Fig. 4.

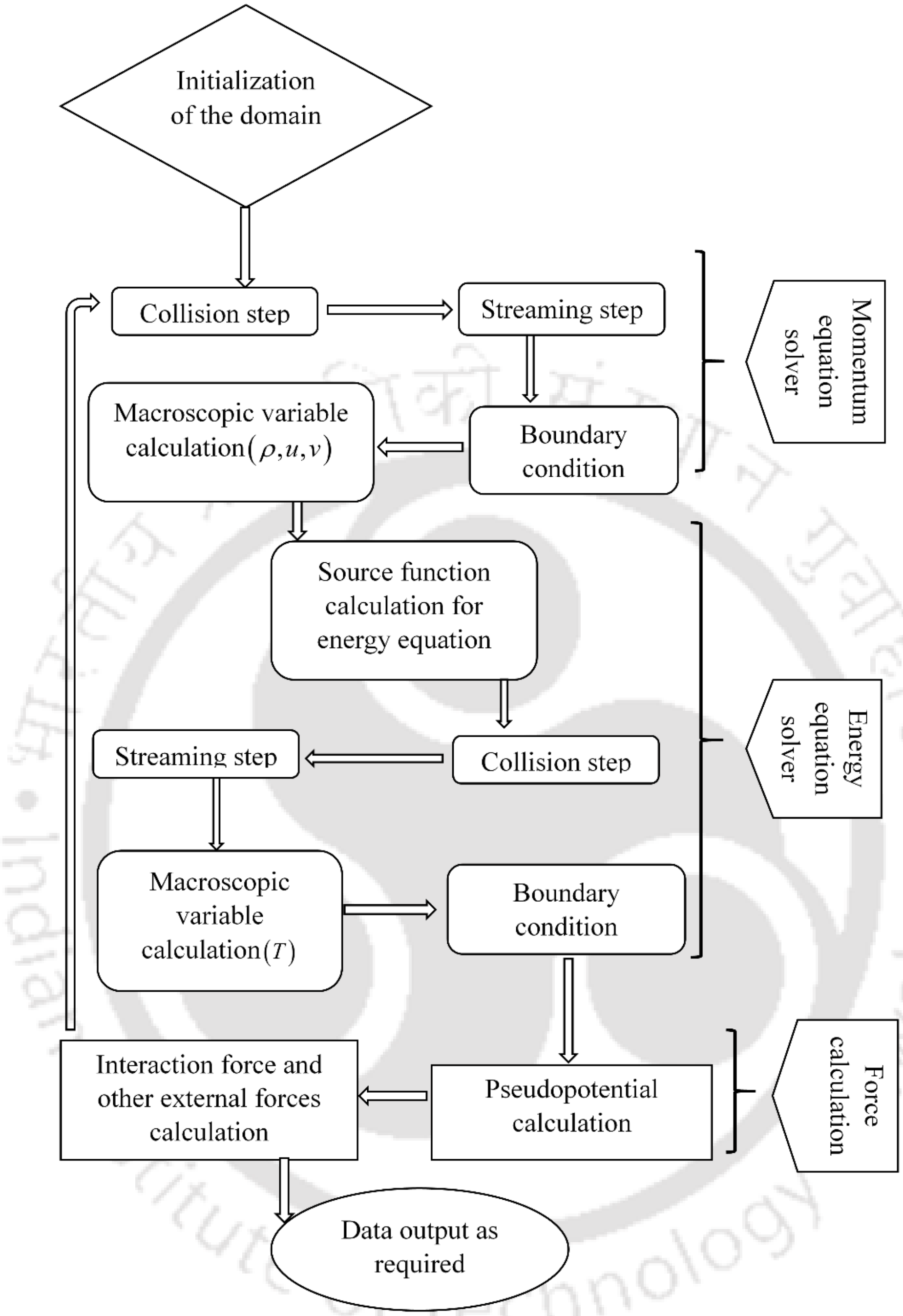

Fig 4 Flowchart for the LB algorithm

Chapter 3

LBM Simulation of Flow Boiling through Narrow Fluidic Channel

3.1 Introduction

Subcooled flow boiling in a narrow fluidic channel provides higher heat transfer performance than conventional channels, attributed primarily to the larger area per unit volume of the fluid in close proximity to the heating zone. Several studies on the phase change phenomenon in the paradigm of flow boiling in mini and microchannels following both the experimental investigations as well as numerical simulations have been reported in the literature. Although, experiments on two phase flow with the associated phase change phenomenon can predict different flow patterns and the involved thermohydrodynamics, the basic mechanism of phase change process and complex interplay of the involved forces behind different kinds of bubble behavior are remaining restricted to be explored through experimental investigations. In the conventional numerical approaches, phase change simulations following these methods require either a nucleus to be placed at the nucleation site or ingraining of pseudo boiling approach in the model itself. A brief literature survey on the various works on flow boiling reveals that despite having a great possibility to be an excellent numerical method, only a few works are reported using the pseudopotential based thermal multiphase model in the arena of flow boiling. This work aims to extend the applicability of the phase change LB model in a full-scale simulation of flow boiling in a horizontal narrow fluidic channel. Also, parametric studies which are remaining unexplored to date like the effect of wall superheat, surface wettability, and inlet mass flux on the bubble dynamics (to be precise, departure diameter and release frequency) in nucleate flow boiling regime are performed. Bubble dynamics and heat transfer characteristics are investigated in detail and the effect of different parameters on these aspects are studied thoroughly.

3.2 Problem Definition

A computational domain comprising of 40×1000 lattices is selected to represent a two-dimensional rectangular channel having height-to-length ratio of 1 / 25, the schematic of which is presented in Fig. 5. The channel is subjected to a stream of subcooled liquid with specified velocity and temperature at the inlet, whereas constant pressure and zero temperature gradient conditions are imposed at the exit plane. Both the top and bottom walls are stationary impermeable surfaces, allowing for no-slip boundary condition, while remaining isothermal as well. A microheater is mounted on the bottom wall at one-fifth distance from the channel inlet. It is numerically replicated by inflicting a constant degree of wall superheat on five lattice nodes. All the boundary conditions are marked in Fig. 5 for easier cognizance. The no-slip boundary condition is numerically realized through the classical bounceback approach[5], whereas the entry and exit conditions are accomplished using the non-equilibrium bounceback scheme[164]. The anti-bounceback approach[5] is preferred for the thermal boundary conditions.

The domain is initially assumed to be filled with saturated liquid maintaining its temperature at $T_R = 0.9$. R134a is considered to be the working fluid and all thermophysical properties are estimated at this temperature. Computation is carried out without heating for 10000 timesteps since triggering the motion, to allow the flow to be hydrodynamically fully-developed. Only then the microheater is switched on and ensuing hydrodynamics are followed for computational characterization.

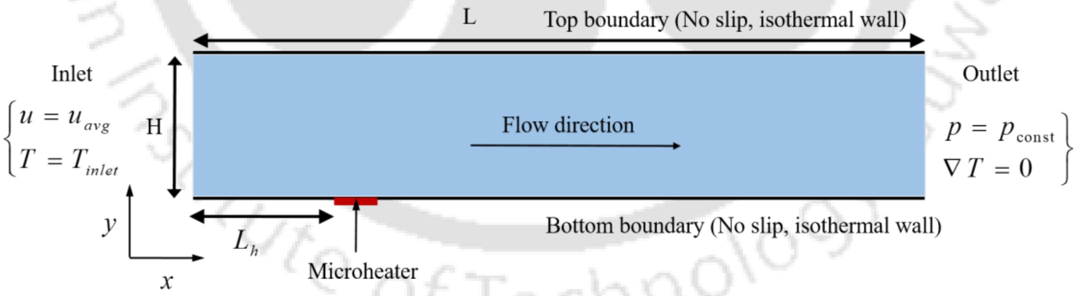

Fig. 5 Schematic presentation of the physical domain considered in present study, along with all applicable boundary conditions. The coordinate system is attached at the left bottom corner of the channel.

3.3 Model Validation

In an effort to ascertain the accuracy of the algorithm, certain benchmark cases from literature are simulated and compared with the standard solutions. Our first selection is for single-phase isothermal Poiseullie flow through a duct, primarily to check the consistency of the solver. The cross-sectional profile of x-direction velocity is compared with the analytical solution in Fig. 6(a), for the axial position of 8H with $\mathrm{Re}_{in} = 0.96$ at t = 10000 lattice units. The inlet Reynolds number Re_{in} has been defined in terms of the supply velocity, channel width and inlet-plane properties. On application of pressure inlet and outlet boundary conditions, the analytical profile follows the well-established form of,

$$\frac{u(y)}{u_{avg}} = \frac{6y}{H}\left\{1 - \frac{y}{H}\right\} \tag{55}$$

for the rectangular duct under consideration. As desired, an excellent match can be observed, with parabolic shape and maximum velocity assuming 1.5 times the average value, which substantiates the correctness of the algorithm for single-phase flows.

As noted earlier, one major concern with the classical SC model is the thermodynamic inconsistency, as the simultaneous requirement of compliance to EOS and consistency to the thermodynamic definition of surface tension can be satisfied only for very low density ratio. The recent amendments[4,45], though, has helped eliminating this apprehension till a certain range. Reduced density values ρ_R are plotted against the reduced temperature T_R in Fig. 6(b), to facilitate a direct comparison with the analytical value. A satisfactory level of conformity is obtained for $T_R \geq 0.7$. In the present study, we persist with $T_R = 0.9$, where the model is very much consistent thermodynamically, and hence is expected to yield accurate predictions.

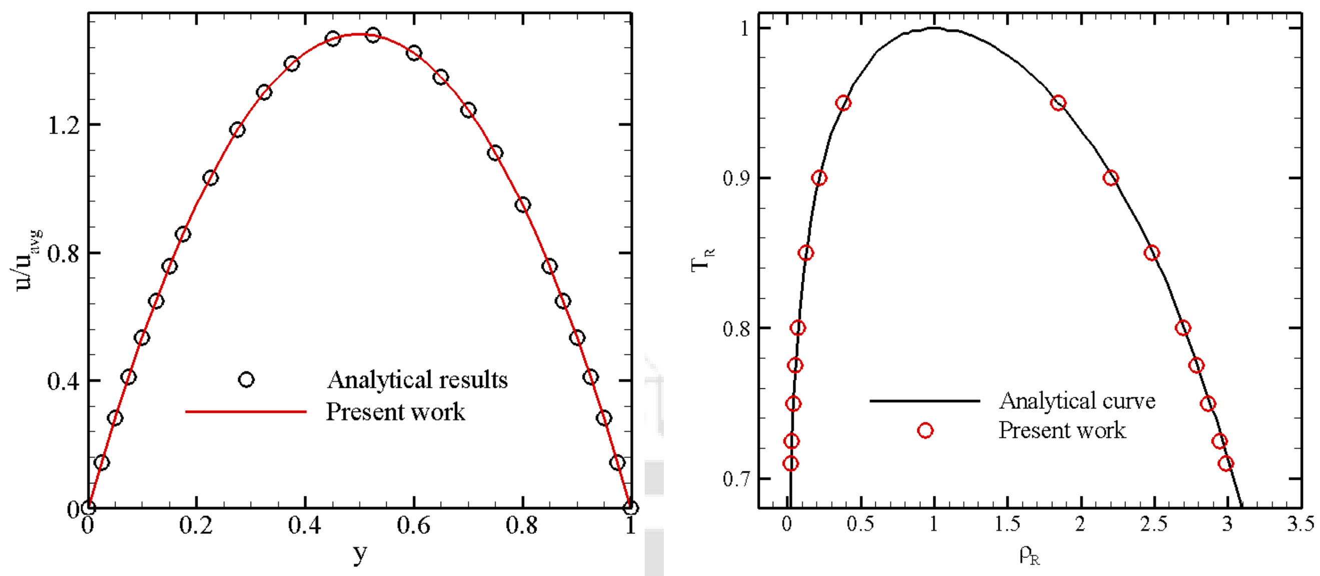

(a) (b)

Fig. 6 Model validation: (a) Parabolic velocity profile for single-phase flow through rectangular dust shows excellent match with the analytical solution; (b) Coexisting densities of liquid and vapour phases adhere to the Maxwell area construction rule till $T_R = 0.7$

Owing to the lack of reliable experimental data, as well as thermalhydraulic correlation, for flow boiling at this temperature range, another set of validation is attempted for pool boiling scenario. According to Fritz's correlation[6], the bubble departure diameter is reliant on gravity, surface tension, surface wettability, as well as the coexisting densities of both phases. For a specified temperature, other properties are constant, making the departure diameter a direct function of gravity. We consider a rectangular domain of aspect ratio 4, initially filled with saturated liquid having $T_R = 0.9$. The bottom boundary is maintained isothermal at the saturation temperature itself, while the side boundaries are periodic and the top is envisaged as a free surface. A microheater spanning 5 lattice units is placed at the center of the bottom wall, which is maintained at a higher temperature of $T_R = 1.05$. Snapshots of the resultant ebullition cycle are presented in Fig. 7(a), vividly illustrating each important stage of pool boiling, such as nucleation, growth, and departure, for a lattice-level gravitational acceleration of $g = 5\times10^{-5}$. Here the phases have been identified based on their density levels. A nodal density value greater than the $\rho_{avg} = {\rho_l + \rho_v}/{2}$ symbolizes liquid, whereas a lower level corresponds to the vapor phase.

The variation in the departure diameter for different levels of g is portrayed in Fig. 7(b) for the same temperature combinations mentioned above. The developed data points can be regressed as, $D_d = 0.246 g^{-0.49}$ which is within acceptable proximity to the exponent of 0.5 proposed by Fritz. Therefore, we can definitely claim that the present SC-LBM algorithm can successfully reproduce the boiling phenomenon and hence can be used to explore the microdynamics of flow boiling.

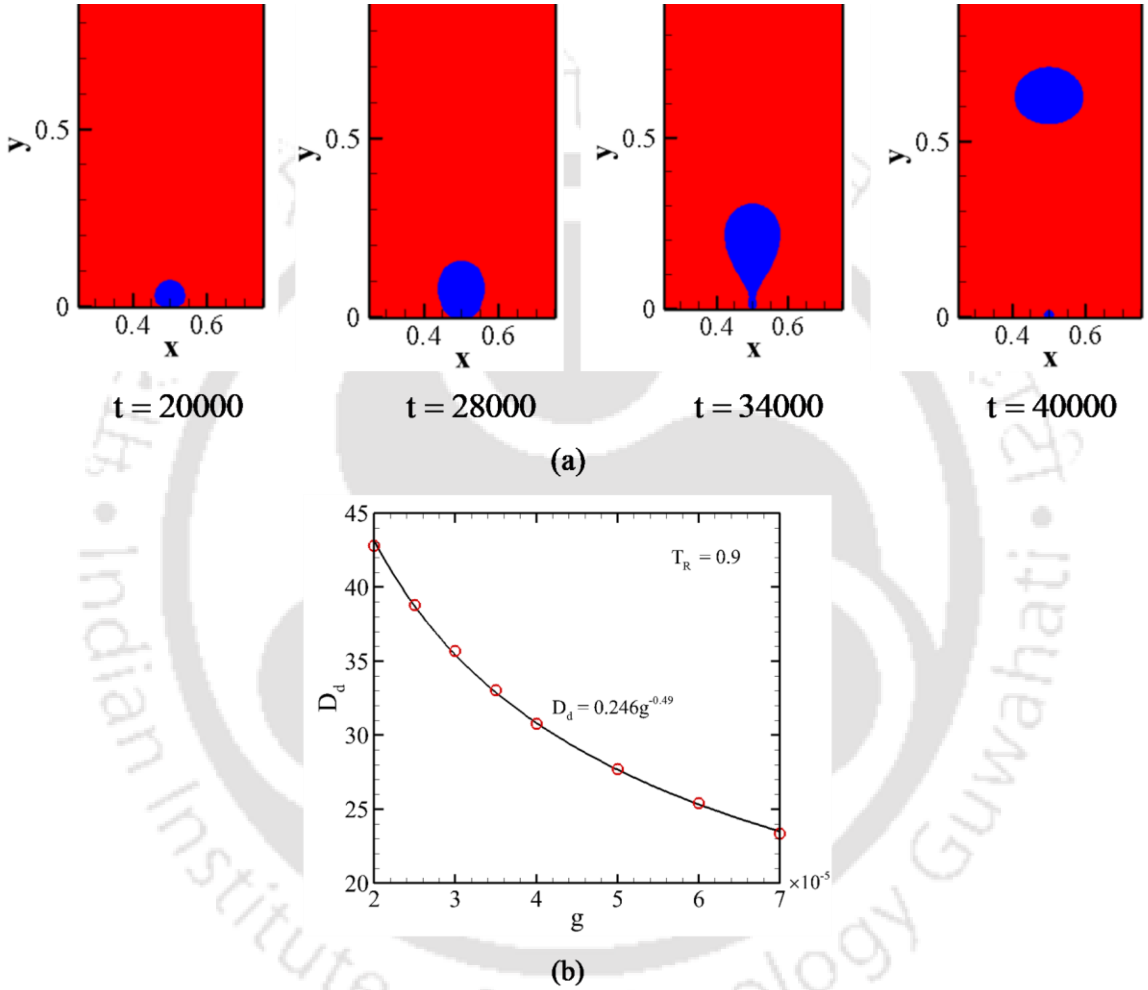

(a)

(b)

Fig. 7 (a) Snapshots of one bubble ebullition cycle from a microheater in an open vertical domain at different time instants, with red and blue colors respectively symbolizing liquid and vapor phases; (b) Variation in bubble departure diameter with gravitational acceleration shows reasonable allegiance to the Fritz's correlationship

3.4 General Bubble Dynamics

The objective of the present study is to explore the dynamics of vapor bubbles during flow boiling in a narrow fluidic channel. During real-life experimentation, vapor production is facilitated through the presence of nucleation sites, in the form of cavities or discontinuities, on the heated surface. It is also possible to embed a microheater, having dimension comparable to the bubble diameter, on the wall adjacent to the flow field, which can serve as a nucleation site. A direct numerical duplication of the same is not possible with the Eulerian-averaging approach. It is necessary either to initialize the domain with a pre-existing vapor nucleus[106], or allow vapor injection through a microgap till the formation of a stable nucleus, which is referred as pseudo-nucleation[108]. Both the options fail to mimic the experimental situation, and phase-change LB models clearly score better here by allowing natural separation of phases. In the present SC-LBM algorithm, liquid-vapor coexistence density is controlled by the selected non-ideal EOS (PR-EOS) appearing inside the modified pressure tensor. Once the liquid temperature is higher than saturation (superheated liquid) and sufficient energy is available in latent mode, the EOS will allow the nodal instantaneous density to acquire the magnitude corresponding to saturated vapor. The reverse is true on dissipation of sufficient amount of energy from the vapor phase. It is, therefore, possible to initiate vapor nucleation in the flow field by placing a microheater on the surface (Fig. 5), analogous to the experiments, consequently allowing us to get a more comprehensive perspective of flow boiling. We, therefore, employ the SC-LBM algorithm for exploring the dynamics and regimes flow boiling in the subsequent sections. Quite often the shape instabilities or dynamics of rising bubbles in multiphase simulations are characterized using the Eötvös number, to envisage the interplay between gravitational and surface tension forces. However, it requires the information about the bubble diameter, which is continuously changing for a growing nucleus. The Morton number $Mo = {g\mu l^4 \Delta\rho} \big/ {\rho_l^2 \sigma^3}$, being a sole function of fluid properties, seems a more reasonable choice. Unless mentioned otherwise, all the reported simulations correspond to $T_{\mathrm{R},in} = 0.9$, $\mathrm{Re}_{in} = 0.96$, $Mo = 7.27\times10^{-3}$, $T_{R,h} = 1.2$ and $\theta = 52.23^0$. The adopted length and time scales are discussed in the Appendix B. Accordingly, the present channel having a width of 40 lattice units closely resembles a rectangular minichannel of 1.01 mm height, while 1 lu time = 8.81 s of physical time. For the ease of representation, all the subsequent results have been displayed using time in lu. However, that can always be correlated to the macroscopic time using the above conversion.

The microheater is activated at t = 10000 l.u., with the logical presumption of the single-phase fluid already attaining fully-developed condition. Because of the external heating, temperature of the fluid in the vicinity of the heater increases, and vapor nucleation process is gradually initiated. It is a well-established fact that multiphase flow through any duct always experiences greater pressure drop compared to its single-phase counterpart, mostly owing to the emergence of strong accelerational components [6]. We have initialized the domain with liquid maintained at saturation temperature corresponding to the exit pressure, which is also the inlet value. On the incipience of flow, inlet pressure must increase to accommodate for the pressure drop suffered across the duct. Such rise in inlet pressure is even more prominent on the onset of nucleation, and can mutate with the transition in flow regimes. The direct implication of such pressure inflation, with constant inlet temperature, is the fluid attaining subcooled state at the entrance plane, and the entire thermohydrodynamics inside the channel assuming the characteristics of subcooled flow boiling.

Following the recent argument of Du et al.[165], during its growth from a nucleation site, a bubble can be subjected to six different forces, namely, buoyancy, contact pressure force, lift, drag, bubble growth force and surface tension. While the first three act solely in the vertical direction, drag is horizontal, and the other two can have components along both coordinate directions in a 2D domain. Combined effect of drag, lift and buoyancy is an attempt to detach the bubble from the nucleation site, whereas surface tension and bubble growth forces intend the opposite. Bubble departure is possible when the balance within these two conflicting groups is broken, and subsequently, the bubble may briefly slide along the channel wall depending on the relative strength of the first set. Of course, the bubble will finally encroach into the bulk stream to flow downstream and possibly rise towards the upper part of the channel owing to buoyancy.

The rate of bubble growth is modulated by the interplay between the rate of evaporation, at the interface in contact with the slender superheated liquid layer engulfing the microheater surface, and the rate of condensation, at the portion of the interface far away from the heated surface and submerged in the subcooled liquid. During the entire ebullition cycle, encompassing nucleation, growth and departure, the rate of evaporation is much higher, as the bubble is expected to be primarily enveloped by the superheated liquid. That is, however, not true for the post-departure period, as the bubble moves with the bulk stream and is surrounded by saturated or subcooled liquid, which can lead to a reduction in bubble volume owing to the dominant condensation effect and eventual collapse. The entire bubble flow dynamics explained above is demonstrated through multiple snapshots in Fig. 8 for three sequential bubble release.

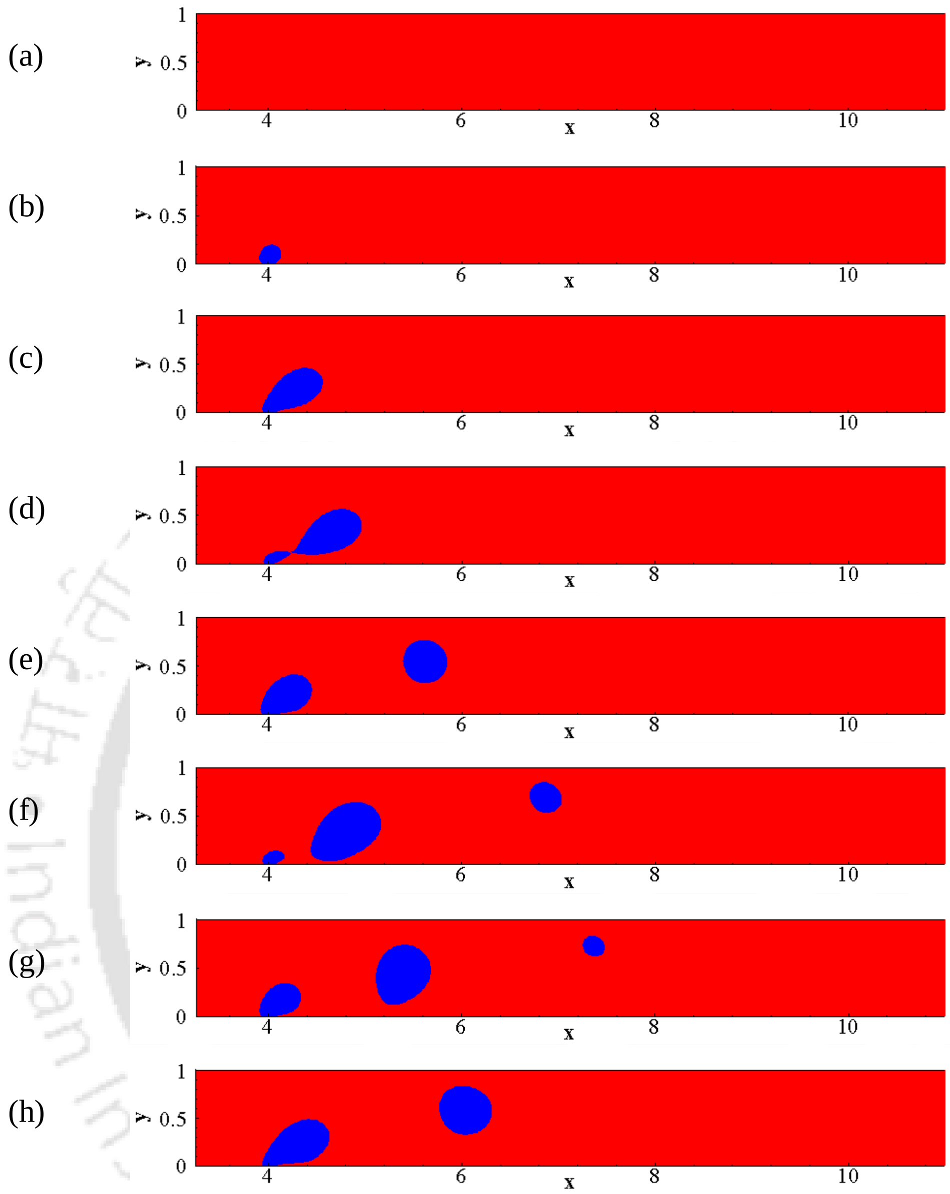

Fig. 8 Snapshots of a complete bubble evolution cycle in bubbly flow $\left(\mathrm{Re}_{in}=0.96, T_{R,in}=0.9, T_{R,h}=1.2\right)$, with red and blue colors respectively symbolizing liquid and vapor phases: (a) t = 10000, (b) t = 12000, (c) t = 20000, (d) t = 25848, (e) t = 32000, (f) t = 38000, (g) t = 42000, (h) t = 47000

The first instance presented in Fig. 8(a) corresponds to t = 10000 lu, which marks the end of no-heating simulation. As expected, the entire domain is filled with single-phase liquid and the flow is hydrodynamically fully-developed. Now the microheater is activated, instigating the development of a superheated liquid layer around it, and subsequent phase conversion. At t = 12000 lu, a small vapor embryo can be spotted on the heater surface (Fig. 8(b)), which is being pushed downstream by the inertia of the flowing liquid. Consequently, the interface is asymmetric with respect to the vertical direction, with a little tilt towards the right. This is a crucial difference in the mechanism of nucleation compared to pool boiling, where buoyancy is the solitary influence to note and gives a symmetric shape to the growing bubble. The shearing effect of the surrounding liquid keeps on increasing with the continual enhancement in the two-phase contact line, as the nucleus continually grows in volume and a much larger bubble can be seen in Fig. 8(c) at t = 20000 lu. It is very much inclined towards right, with the principal axis making an angle of about 40^0 to the wall. Continuous shoving of the liquid also aids the necking of the bubble, as is hinted here, leading to the eventual departure at t = 25848 lu (Fig. 8(d)). As the first bubble leaves the surface, a small embryo is left behind, which starts growing into the second bubble, thereby initiating a repetitive pattern. An excellent account of the role of the velocity of the neighboring liquid on the departure process can be found following the magnified view of the vectors shown in Fig. 8. With the appearance of the bubble at t = 12000 lu, there is only local distortion in the originally-parallel flow pattern. The motion of the fluid away from the nucleation site remains virtually ignorant of the presence of the vapor embryo. The continued growth in the volume of the bubble, however, inflict more significant changes in the velocity vectors in subsequent time intervals, with the liquid being pushed towards the upper wall. As the nucleus progressively tilts to the flow direction, a thin liquid film also starts forming below that. Figure 8(b) presents the domain at t = 25848 lu, the instant of departure. Clearly, the departed bubble is being pushed forward by the moving liquid, while also floating upwards owing to the buoyancy effects, as is demonstrated by the vectors inside the interface.

It is interesting to observe from Fig. 8(e), while the second bubble has evolved significantly in volume, the departed one has withered a bit, suggesting towards condensation. The same can be substantiated following the temperature fields portrayed in Fig. 9, which shows considerable temperature variation in the vertical direction inside the growing vapor embryo. The vapor phase interior to the nucleus is generally superheated, with very high temperature being observed in the vicinity of the microheater. The same, though, is not applicable for the liquid in contact with the tip of the bubble, particularly when that has grown sufficiently in size. Post-departure, the first bubble leaving the heater is completely engulfed by liquid having much lower temperature (Fig. 9(b)). As there is no energy source available to this bubble, while it loses energy to the surrounding liquid via convection across the interface, it starts

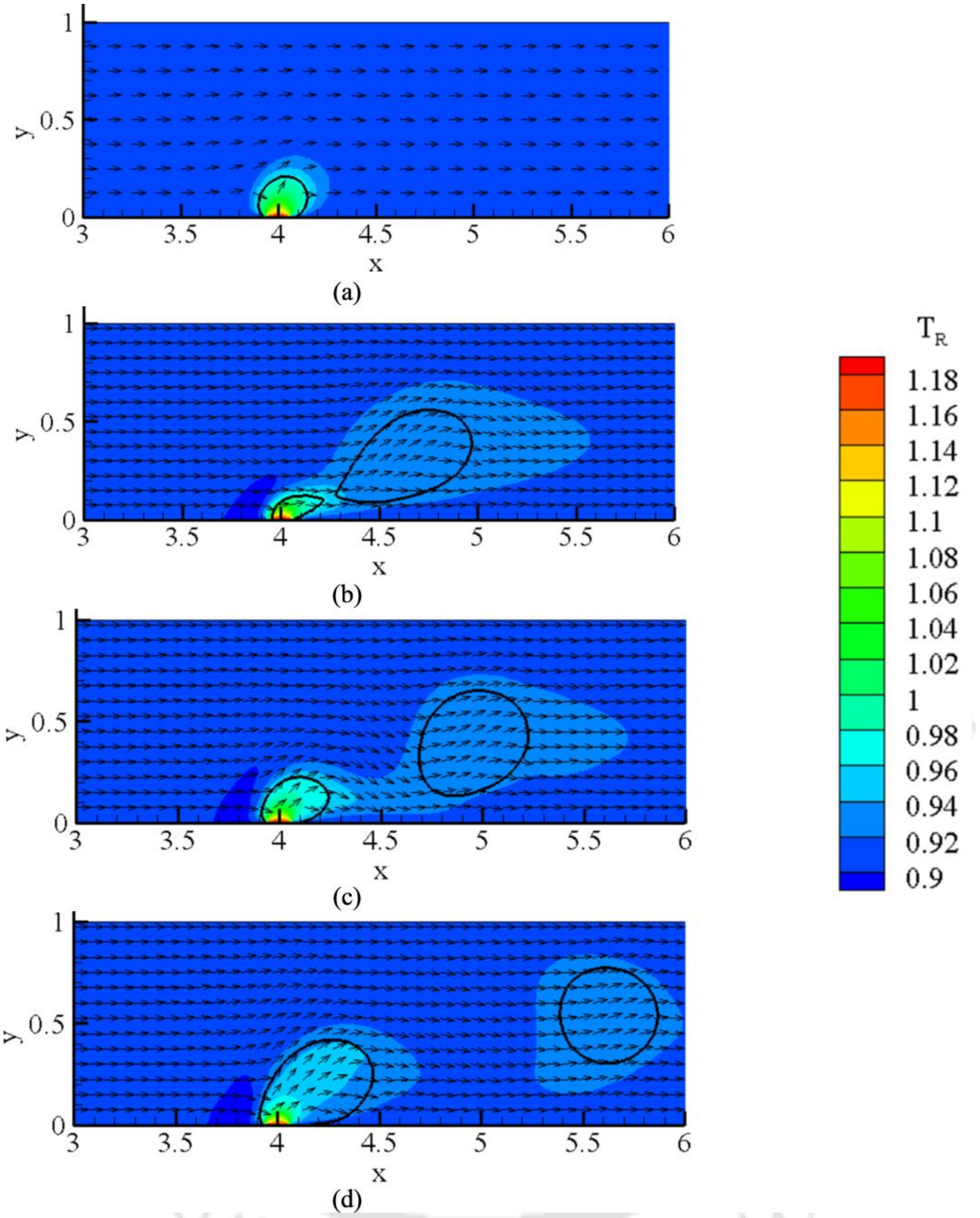

3

Fig. 9 Contours of reduced temperature and velocity vectors around the departing bubble at certain time intervals for $\mathrm{Re}_{in} = 0.96, T_{R,in} = 0.9, T_{R,h} = 1.2$: (a) t = 12000, (b) t = 25848, (c) t = 28000 and (d) t = 32000. Subcooled liquid is seen to rush in to fill the void created by departure. Strong temperature gradient is also evident inside the growing nucleus.

condensing, which is very much palpable in Fig. 9(c) corresponding to t = 28000 lu, shortly after the departure of the first bubble. The second bubble sitting on the microheater is completely surrounded by superheated liquid, but not the departed one. The velocity vectors clearly signify that the subcooled liquid is rushing in to fill the void created by the departure of the earlier bubble, which leads to the heat loss from the initially superheated bubble, and hence condensation. The volume of the bubble is even smaller at t = 32000 lu (Fig. 9(d)), with a narrower thermal boundary layer around it and the space between both the bubbles almost being completely occupied by the low-temperature liquid. The observed presence of strong temperature gradient inside the growing nucleus is consistent with the experimental observations, but commonly ignored during numerical simulation by assuming the vapor phase to remain saturated. So, it can be claimed as a testimony of the present numerical framework in successfully emulating the local thermalhydraulics of the ebullition cycle.

Each of the subsequent bubbles demonstrates cycles identical to the first one, as can be affirmed following Fig. (8f-h). Consequent to their individual departures, the bubbles condense steadily in the subcooled stream. As mentioned before, based on the imposed inlet temperature and exit pressure, bulk liquid is mostly subcooled within the channel, while the fluid particles interior to the interface are expected to be superheated, as already discussed in the previous paragraph. The wall superheat employed on the microheater surface $\left(\Delta T_{\text{sup}} = 0.3T_c\right)$ possibly is not very high and hence not capable of imparting sufficient energy into the departing bubbles to make them survive in the bulk. The bubble also moves upward owing to buoyancy during its travel. As the top wall is maintained at the inlet temperature throughout, the liquid in contact with it is always highly-subcooled, and hence absorbs energy from the moving bubble, augmenting the condensation rate. The first vapor bubble completely condenses slightly before t = 47000 lu (Fig. 8h), when the third one is about of leave the nucleation site.

An alternate perspective to the entire lifespan can be obtained following the temporal variation in the area of the first departed bubble, as illustrated in Fig. 10. As we are performing a 2D simulation, the area can be considered to be a direct representation of the bubble volume. It becomes non-zero immediately on applying wall superheat and increases monotonically till the departure. Some minor ripples can be noted immediately before departure, which is associated with the necking and possibly also with the condensation from the upper surface of the bubble. On departure, the bubble leaves behind a

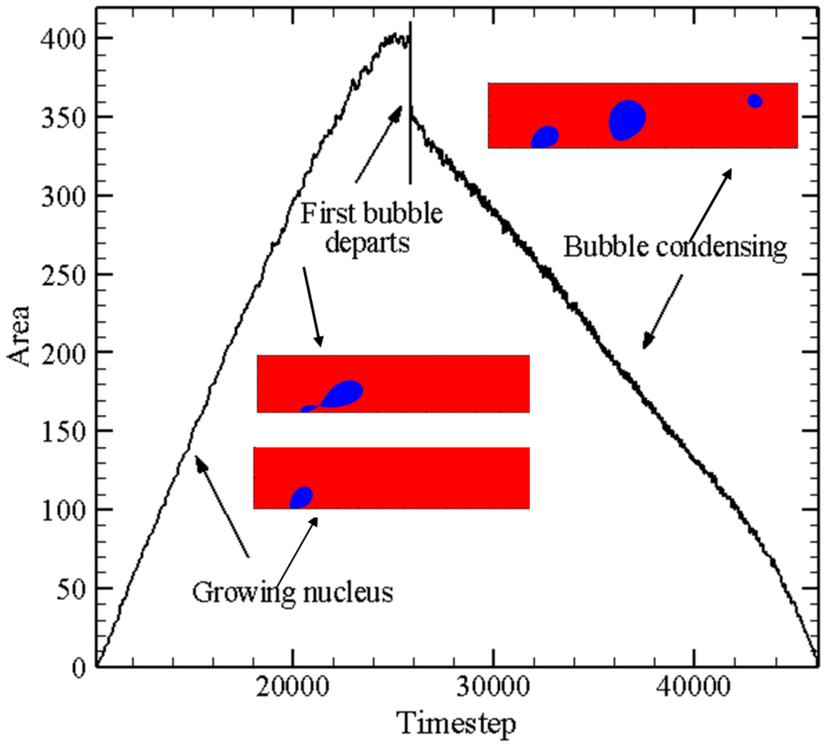

Fig. 10 Temporal variation in the area of the first bubble over its entire lifespan, along with certain important snapshots, for $\mathrm{Re}_{in} = 0.96, T_{R,in} = 0.9, T_{R,h} = 1.2$

small embryo to facilitate the next nucleation, which explains the sudden drop in area at t = 25848 lu. As the bubble moves away from the heater, it experiences condensation owing to the heat loss to neighboring subcooled liquid. That is clearly depicted through the steady decline in the area post-departure. The rate of deterioration enhances with time, as the bubble transgresses towards the upper wall. The area finally attains a zero value at t = 46185 lu, indicating the complete collapse of the first vapor bubble. The same cycle is repeated for each of the subsequent ones, allowing the domain to attain near-periodicity.

It may be noted here that the evolution of the shape of the first bubble till departure is visibly similar to the one reported by [166] employing LBM for slowly-flowing fluid, where they tracked the interface with an extended Cahn-Hilliard equation. Their approach requires the assumption of an initial nucleus, while being computationally expensive. The limitation of their model is highlighted by the regression relation of $D_d \propto g^{-0.425}$ for pool boiling. To expedite a better qualitative comparison, we have compared the bubble shapes during nucleation and growth with the observations of Zu et al.[1] in Fig. 11. They experimented with a rectangular microchannel of 0.38 mm height, housing a localized heater at

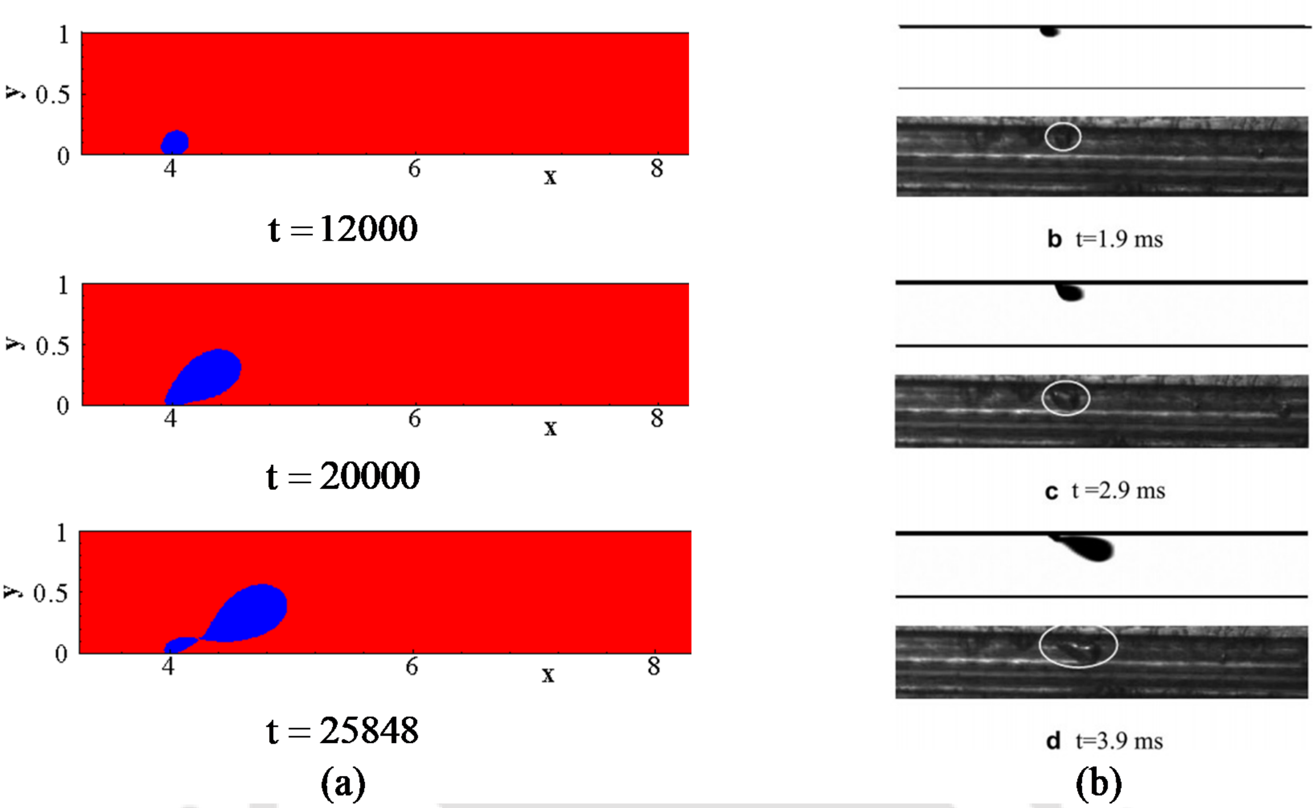

Fig. 11 Visual comparison of the evolution in bubble shapes till departure with the experimental observations and computational results of Zu et al.[1]

the upper wall, and also performed numerical simulation adopting volume-of-fluid with pseudo-boiling approach, where vapor is injected into the domain at a controlled rate to simulate phase-change. The similarity in the shapes from nucleation till departure is quite palpable. A quantitative comparison, however, is not feasible, as their working medium was water, involving a noticeable difference in working condition. There is conspicuous dissimilarity in the involved length and time scales, owing to the substantial disparity in the magnitudes of the relevant thermophysical properties, and also reported uncertainty in determining the time of bubble generation and height of the nucleation site. Still, the success of the present model in reproducing the physics around the nucleation site cannot be mistaken. A measure of the substantially greater computational resource requirement with volume-of-fluid solver is evident from the employment of $225 \times 50 \times 50$ meshes, with local grid-refinement around the point of injection, despite which it fails to replicate the natural process of nucleation.

The departure diameter and time required for departure are expected to hinge upon the prevailing drag force, which, in turn, is a direct function of the inlet velocity. The liquid inertia is higher with larger mass flux, and hence has greater potential of tearing the bubble from the microheater surface. Consequently, the departure diameter is supposed to reduce with increasing the flow rate, i.e., inlet Reynolds number (Re_{in}). The converse is true for lower Re_{in}. A similar effect can be foreseen by increasing the wall superheat, as a larger surface temperature is apprehended to infuse energy at a faster rate into the nucleus, instigating accelerated bubble growth, and hence early departure owing to buoyancy. When the bubble diameter becomes comparable with the channel dimension, we enter the slug flow regime, characterized by large vapor slugs covering virtually the entire channel cross-section. The effect can be envisaged to be more prominent in narrow channels, as is the present case.

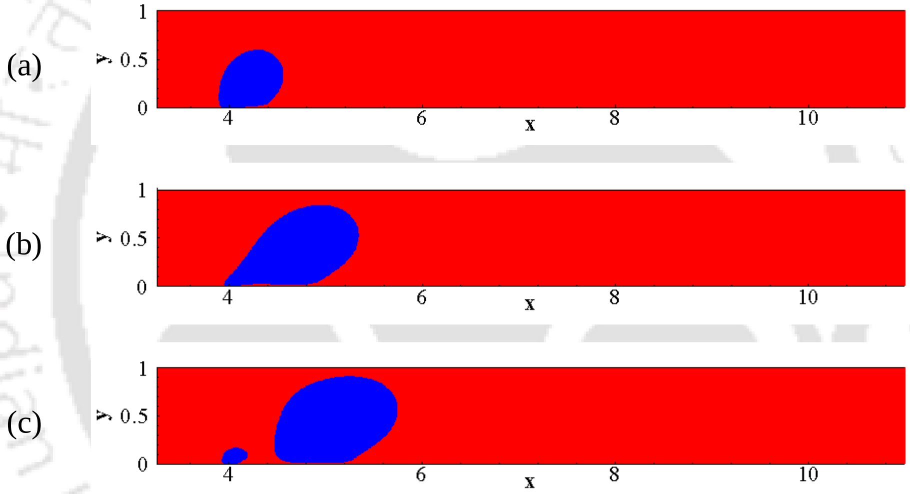

Fig. 12 Snapshots of bubble evolution in slug flow $\left(\mathrm{Re}_{in}=0.48, T_{R,in}=0.9, T_{R,h}=1.2\right)$, with red and blue colors respectively symbolizing liquid and vapor phases: (a) t = 18000, (b) t = 26000 and (c) t = 30000

In an effort to reproduce the above physics, simulations are performed for $\mathrm{Re}_{in}=0.48$, while maintaining identical superheat and contact angle, and a few sample snapshots of the domain is presented in Fig. 12. The growth of the bubble is much faster compared to the bubbly flow situation, as is shown in Fig. 12(a) for t = 18000 lu. The growth rate continually increases with time, and the bubble starts elongating in the flow direction, as it has no space to expand in vertical. A notably-stretched bubble is about to depart at t = 26000 lu (Fig. 12(b)). Lower velocity results in reduced drag force, which delays the departure, while allowing the bubble to grow, emphasizing the role of liquid inertia. At t = 30000 lu, departure is complete and the large vapor slug is sliding along the lower wall, while a small nucleus is left behind to initiate a repetitive pattern. A direct comparison can be drawn here regarding the transient evolution of the shape of the nucleus till departure for the two Reynolds numbers considered, which is available in Fig. 13. For $\mathrm{Re}_{in} = 0.96$, the bubble starts to tilt towards the right almost immediately after appearance and gradually assumes an elliptical profile, while also shifting upwards owing to the enhancing buoyancy effect. For $\mathrm{Re}_{in} = 0.48$, however, the bottom interface of the nucleus continues to be very close to the lower wall, and the bubble slides along the wall even after the departure, primarily because of its characteristic dimension is comparable with the channel height. Similar sliding of slug bubbles has been observed in microchannel during experiments as well[167].

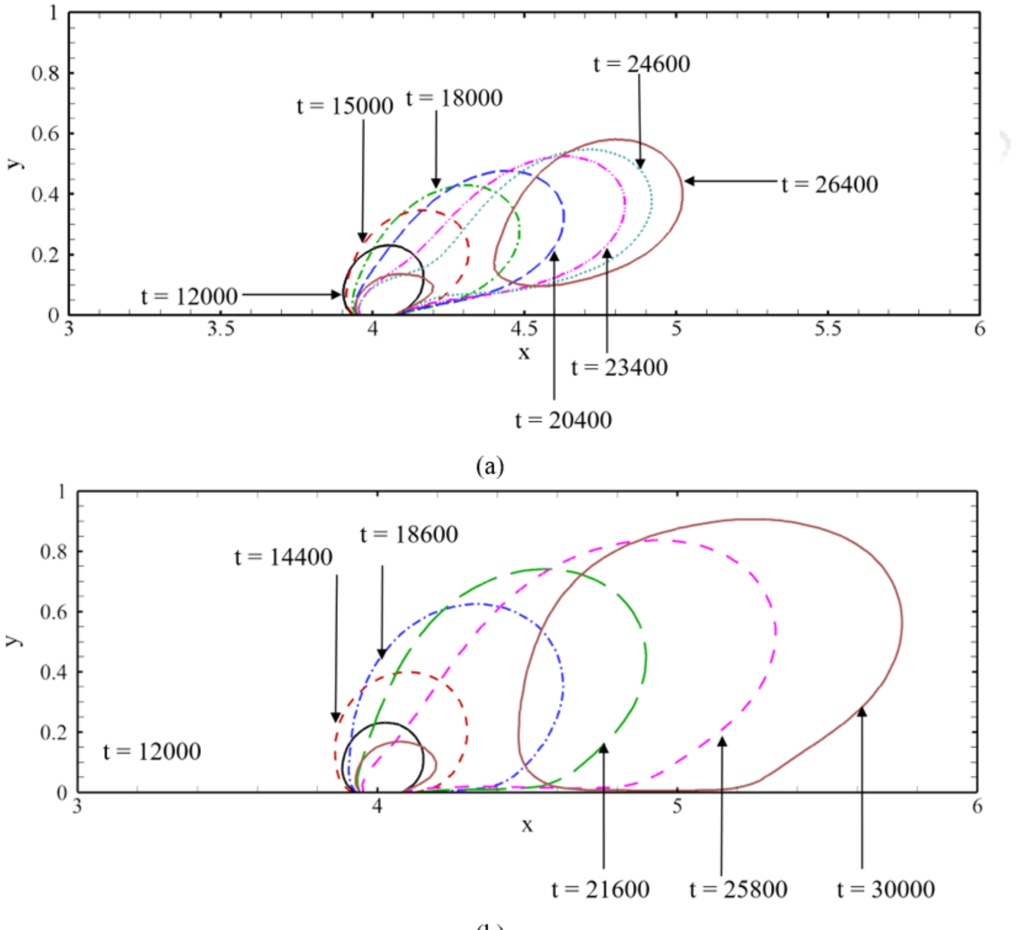

(a)

(b)

Fig. 13 Temporal evaluation of the interface of the bubble for (a) $\mathrm{Re}_{in} = 0.96$ and (b) $\mathrm{Re}_{in} = 0.48$

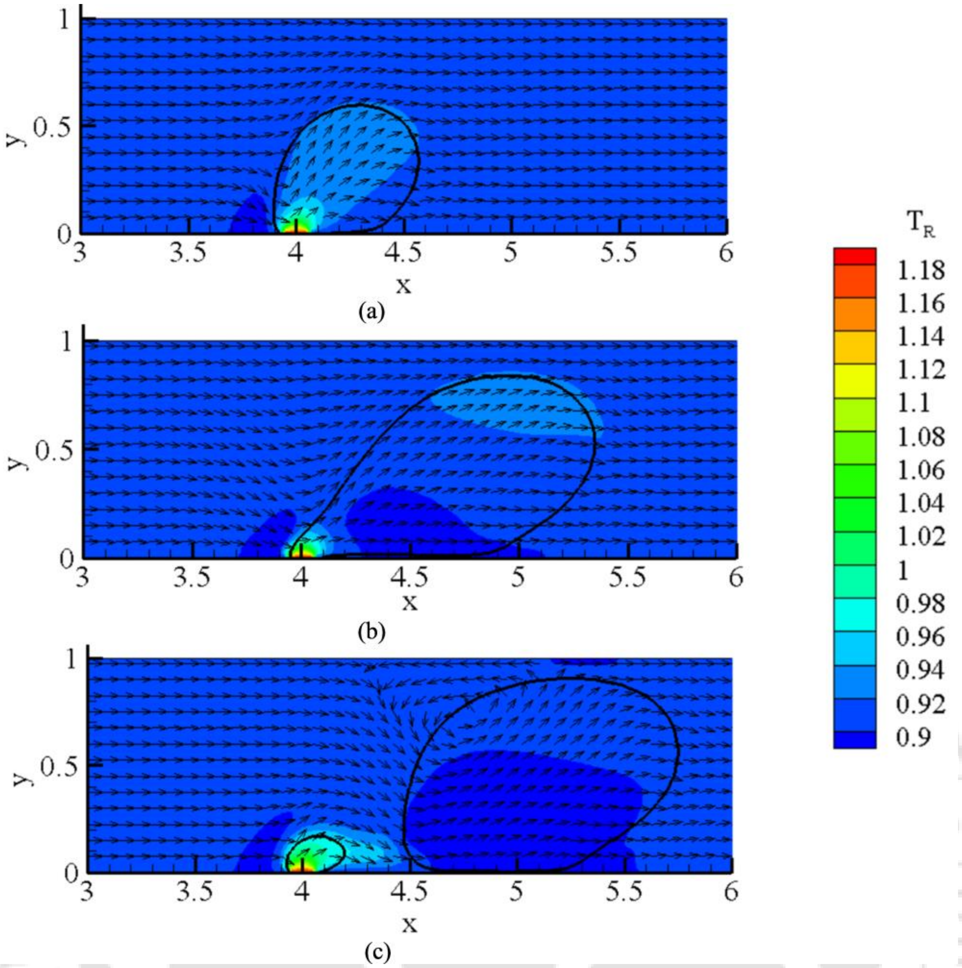

Fig. 14 Contours of reduced temperature and velocity vectors around the bubble slug at certain time intervals for $\mathrm{Re}_{in} = 0.48, T_{R,in} = 0.9, T_{R,h} = 1.2$: (a) t = 18000, (b) t = 26000 and (c) t = 30000

More insight about the corresponding velocity and thermal fields can be acquired following Fig. 14. The rapid growth of the slug bubble distorts the liquid field much earlier than the bubbly flow. That, however, leads to a noticeably moderate temperature level inside the nucleus, with the temperature in the upper part of the bubble being reasonably close to the surrounding liquid. Consequently, the rate of condensation is not significant in the slug flow regime and the departed bubble moves downstream without any appreciable change in the volume. A slender zone of recirculation can be observed near the top wall at t = 30000 lu. This is the manifestation of the swift forward movement of the slug, which creates a low-pressure zone in the rear and induces the local reversed motion. Interestingly, the velocity vector close to the lower edge of the slug attempts to lift it from the surface, as the combined impact of the lift force and buoyancy. But, the equivalent diameter of the bubble being of the same order as the channel width, it is enveloped only by thin liquid films on either side. Consequently, the local buoyancy effect is substantially smaller than the inertia of the slug alone and hence it continues to slide along the bottom surface. Therefore, the present SC-LBM algorithm is successful in capturing the multiphase dynamics inside the narrow channel for both the bubbly and slug flow regimes, while adhering to the underlying physics. Now we can employ the in-house code for exploring the effect of relevant parameters of importance.

3.5 Effect of Inlet Velocity

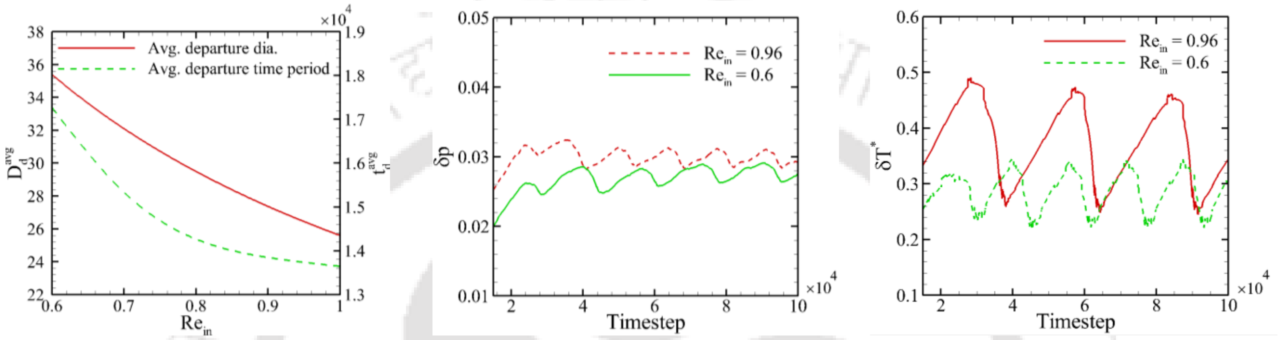

(a) (b) (c)

Fig. 15 (a) The variations in average bubble departure diameter and average bubble departure time with inlet Reynolds number (Re_{in}), and temporal profiles of (b) inlet-to-outlet pressure differential and (c) normalized temperature difference for two different Re_{in}

As discussed above, the supply velocity, characterized by the inlet Reynolds number $\mathrm{Re}_{\mathrm{in}}$, has a strong influence on the departure diameter and nucleation frequency. Greater velocity enhances the shearing effect, causing early departure with lesser bubble volume. Du et al.[165] argued that a larger flow rate also augments convective heat transfer, which allows a greater fraction of the supplied energy to be carried by the liquid phase, thereby slowing down the bubble growth. To have a more comprehensive view, simulations are performed for multiple Re_{in} , and the concerned variations in the average values of the departure diameter and time are presented in Fig. 15(a). The time period of departure on the right hand side Y-axis refers to the time between two subsequent bubble departure events. The times between two bubble departure events are measured for five subsequent bubble departure cases and averaged them to find the average bubble departure period $\left(t_d^{avg}\right)$.Since the first bubble leaves the heater surface, the exercise becomes near-periodic, with minor variations in the departing bubble volume. Here we have estimated the departure diameter as the one averaged over five subsequent departures, while the time period is averaged over four successive releases since the first one. Both the departure diameter and ebullition time of a single bubble continually reduces with Re_{in}, in the anticipated line. Yoo et al.[167] nicely deliberated about the conflict between the single-phase convection and bubble-induced heat transfer on increasing the mass flux. An enhanced flow rate affects both the wall evaporation and quenching processes, causing lesser drop in the temperature of the superheated liquid layer, allowing a quicker recovery towards subsequent nucleation. That can be viewed as the primary reason for the reduction in ebullition time with a rise in flow rate. Sun et al.[166] found the departure diameter to show an exponential relationship with the inlet velocity, where the release frequency varied linearly. Du et al.[165], on the contrary, proposed a regression relationship of $D_d \propto \mathrm{Re}_b^{-0.751}$, analyzing 5 different databases. Here, D_d is the average departure diameter normalized using the characteristics length, and Re_b is the bubble Reynolds number. We can relate the simulated departure diameters as, $D_d^{avg} \propto \mathrm{Re}_{in}^{-0.635}$, which is reasonably close to Du et al.[165], while the time period exhibits a near exponential decline.

The pressure difference across the channel also acquires a periodic pattern, as is displayed in Fig. 15(b), where the temporal variation in pressure drop along the centerline is available for two different $\mathrm{Re}_{\mathrm{in}}$. As mentioned earlier, emergence of the vapor phase enhances the pressure differential, with the accelerational component coming to prominence. It can clearly be seen that every departure corresponds to a reduction in pressure drop, whereas the same starts increasing again with the growth of the next nucleus. With the bubble occupying increasingly larger fraction of the flow area, the pressure drop increases, as the fluid density averaged over the entire domain starts to drop. Post-departure, the bubble condenses in the free stream, which helps the domain to recover pressure for a certain period. Such steep fall in pressure differential was also predicted by the 3D model of Zu et al.[1]. With increase in flow velocity, the shearing loss at both the walls gets augmented, incurring greater pressure loss, which can also be seen from Fig. 15(b).

The associated heat transfer rate can also be characterized following the temporal variation in the normalized temperature differential at the heated surface, $\delta T^* = \left(T_{wall} - T_{neighbour}\right) / \left(T_{wall} - T_{bulk}\right)$ as presented in Fig. 15(c). At the onset of nucleation, vapor starts accumulating on the heated surface, not allowing liquid to come in contact. Vapor being a poor conductor, rate of heat transfer starts declining, as is manifested by the steep rise in the temperature differential. That is also one of the reasons of having stiff temperature gradient inside the nucleus itself (Fig. 8). Thermal communication starts to improve with the initiation of necking. As the bubble gets detached, surrounding liquid rushes in to fill that void, which strongly enhances the convective component of overall heat transfer. The same is manifested in the form of the rapid deterioration in δT^*. For lower $\mathrm{Re}_{\mathrm{in}}$, forced convection is weaker, reducing the heat transfer rate and thereby increasing the surface temperature differential (Fig. 15(c)). The slower bubble growth is also responsible, as vapor stays longer in contact with the heated surface. The upsurge in heat transfer is much starker at lower flow rates, owing to the release of larger-sized bubbles and consequently higher level of liquid motion. Similar role of Reynolds number on the heat transfer coefficient during flow boiling is well-documented in literature[168].

3.6 Effect of Wall Superheat

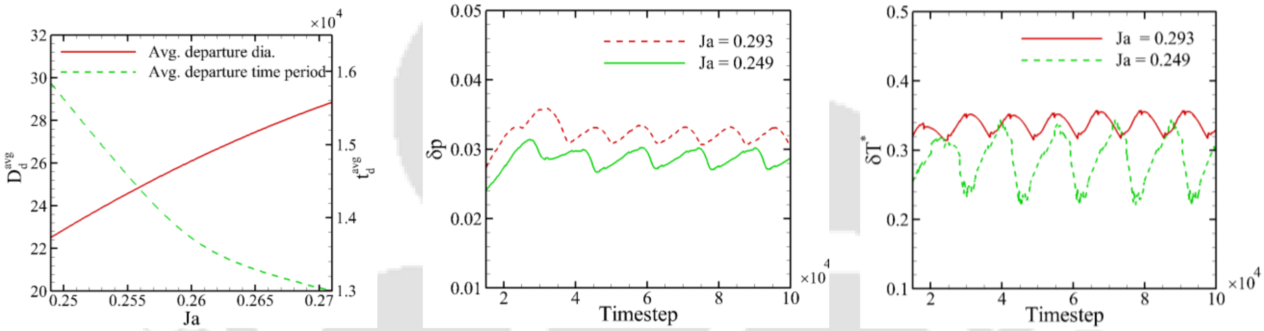

(a) (b) (c)

Fig. 16 (a) The variations in average bubble departure diameter and average bubble departure time with Jacob number (Ja), and temporal profiles of (b) inlet-to-outlet pressure differential and (c) normalized temperature difference for two different Ja

The degree of superheat imposed on the microheater can be represented in terms of the Jacob number $Ja\left(=c_{p,f}\left(T_{wall}-T_{sat}\right)/h_{fg}\right)$, which can be viewed as the ratio of sensible heat transferred to the liquid at the wall to the latent heat transfer. All thermophysical properties being constant, Ja here is a direct function of the wall superheat. The effect of Ja on the flow field can be envisaged following Fig. 16. Du et al.[165] mentioned that a higher Ja strengthens the bubble growth force, which resists the departure. Higher wall superheat also allows the nucleus to gain energy at an elevated rate. Both the above factors contribute towards greater departure diameter, as is evident from Fig. 16(a). A quicker growth also raises the buoyancy, which aids the release from the nucleation site, consequently reducing the length of the ebullition period. The temporal profiles of pressure drop across the channel and normalized temperature difference follows the periodic behavior, as discussed above. Higher wall superheat corresponds to greater bubble area and also enhanced bubble-induced liquid motion post-departure, which is reflected in elevated inlet-to-exit pressure differential. It is interesting to observe that, on increasing Ja, the highest level of δT^* remains nearly the same. However, the undulations are substantially subsided, yielding more-uniform heat transfer rate over the entire span under consideration. That is possibly a consequence of the quicker bubble release and enhanced bubble induced heat transfer[168,169].

3.7 Flow Regime Map

We have seen from the previous discussions that the present SC-LBM algorithm is successful in reproducing the two most common multiphase flow regimes associated with horizontal narrow channels, and also logical pattern of parametric effects. The combined effect of the two variables considered here, namely Re_{in} and Ja, can be summarily viewed in terms of a flow regime map. We have already observed that the bubble departure diameter continually increases with reduction in inlet Reynolds number, owing to the reduced shearing action, and it is possible to attain the slug flow condition for sufficiently small Re_{in}. Similarly, a greater Jacob number produces larger bubble at the instant of release, as higher rate of energy addition infuses more energy into the nucleus. The same is distinctly demonstrated in Fig. 17.

We have compared the temporal variation in the area occupied by the vapor phase $\left(A_{vap}\right)$ and the normalized rate of phase change $\left(\Delta m_{vap}\right)$ for two different Re_{in} in Fig. 17(a). The latter quantity has been estimated by comparing the mass of vapor present in the entire domain in two successive time instants and then scaling that using the vapor density (ρ_v). Clearly the rate of vapor generation is greater at

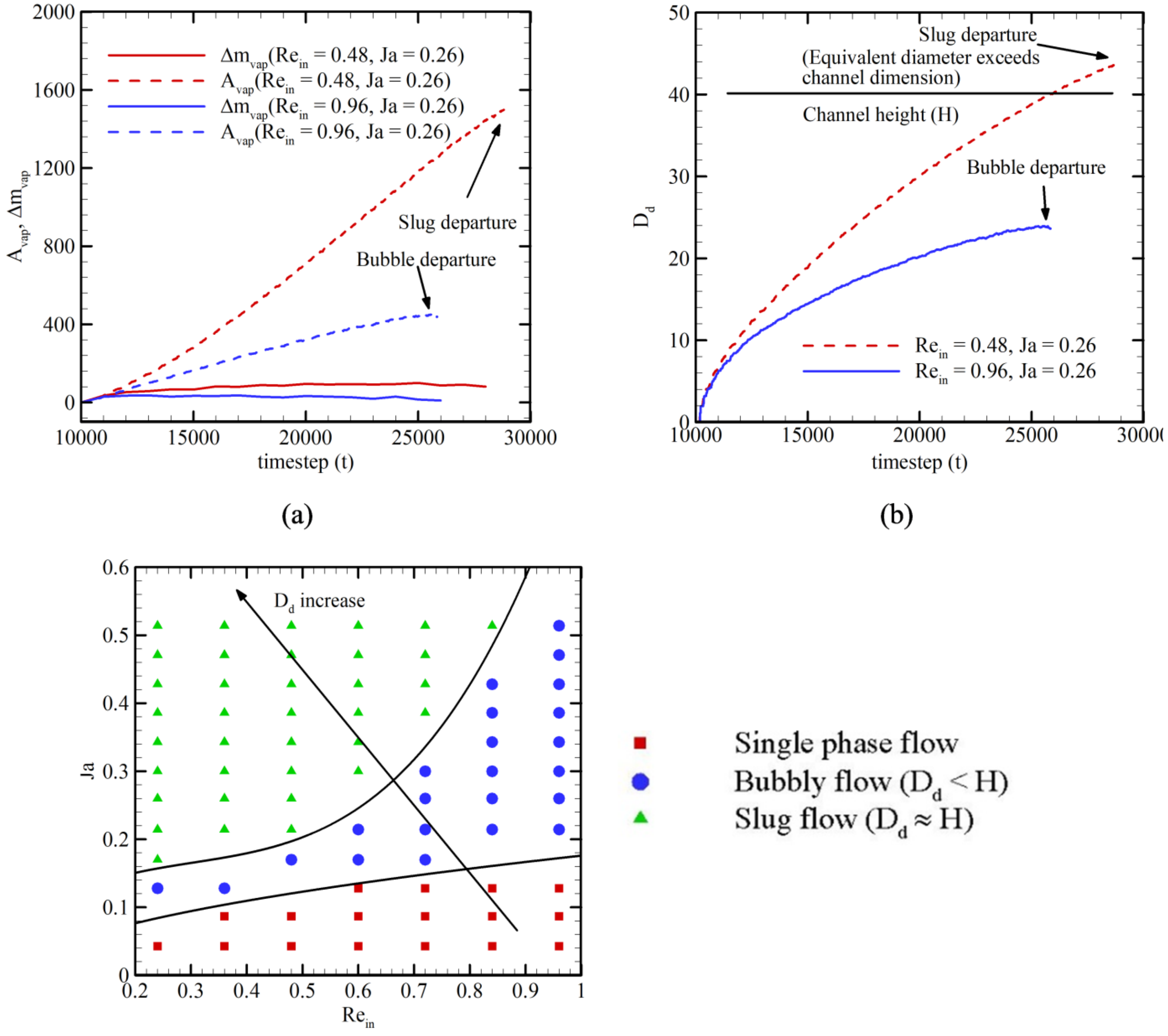

(a)

(b)

(c)

Fig. 17 Flow pattern map in $\mathrm{Re}_{in} - Ja$ plane; where the flow regime changes from single-phase to bubbly to slug in the direction of the arrow; the average bubbled departure diameter increase with increase in Ja and decrease in Re_{in}

$\mathrm{Re}_{in} = 0.48$ and the escalation in the area occupied by vapor, which is indicative of the vapor volume, is very steep. That, however, is quite moderate at higher Re_{in}, and, in fact, shows an inversion shortly before departure, which is the consequence of condensation at the upper surface of the bubble. We have already seen the same trend in Fig. 10. In order to quantify the flow pattern, equivalent diameters of the first nucleus are compared for these two cases (Fig. 17(b)). Diameter of the slug bubble at the instant of departure is definitely higher than the channel height, which is compatible to the experimental observation and also the theoretical definition of a bubble slug. The equivalent diameter of the departing bubble for bubbly flow, though, is significantly smaller. We have employed this particular criterion to differentiate between the bubbly and slug flow regimes and the corresponding transitions have been elaborated in (D_d) Fig. 17(c). When the equivalent diameter at the instant of departure is smaller than the channel height (H), we have categorized the concerned flow regime as bubbly, and slug otherwise. Multiple simulation points are shown, along with the discriminating curves, which will facilitate easy identification of the flow regime from the $\mathrm{Re}_{in} - Ja$ combination. If the flow rate is very high or degree of superheat is low enough, sufficient amount of energy is not available to induce the phase change, and the entire domain experiences solely single-phase flow. Consequently, moving along the negative x-direction or positive y-direction, we can sequentially encounter single-phase flow, multiphase bubbly flow and multiphase slug flow respectively. Same can also be achieved following the arrow shown in the figure, which indicates the direction towards which the departure diameter increases. Qualitatively similar role of inlet mass flux regarding transition from bubbly to slug flow was hinted by Haricharan et al.[170] for horizontal microchannels of various dimensions during their experiments.

3.8 Effect of Surface Wettability

For a specific fluid flowing under a particular set of operating conditions, the nature of the three-phase interface can be a deciding factor in determining the ebullition characteristics and consequent channel thermohydrodynamics. Any combination of liquid-vapor interface and solid surface has an equilibrium value for the static contact angle at given pressure and temperature, dictated by the interfacial energy balance, which characterizes the wettability of the surface. As already mentioned through Eq. (36a), the contact angle can be modulated here by varying the false wall density ρ_w, a graphical representation of which is available in Fig 18. With ρ_w assuming a value closer to the liquid one, the contact angle approaches zero, whereas the reverse is true when it moves towards vapor-level.

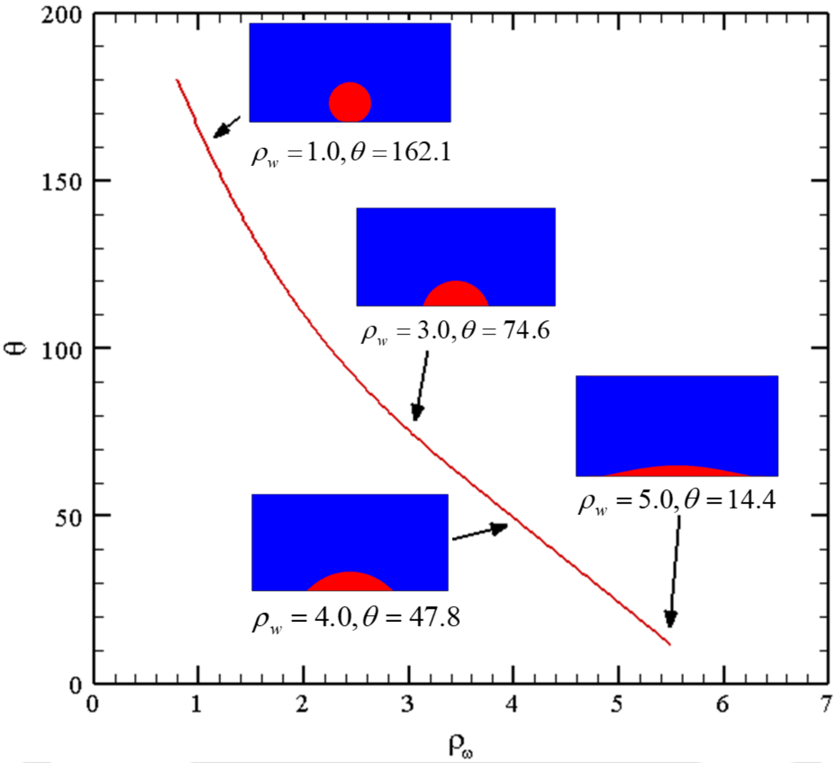

Fig. 18 Variation of the static contact angle (θ_c) with false wall density (ρ_w), where some sample bubble shapes are also shown; an increment in ρ_w causes a decrement in θ_c

Edel et al.[169] argued that the bubble departure is determined by the instantaneous drag force of the passing liquid and the prevailing surface tension force at the bubble contact line. A larger contact angle corresponds to lesser surface wetting by the liquid phase, allowing better accumulation of vapor on the microheater. With vapor covering larger portion of the heated surface, there is an increase in the effective heat transfer area available to the nucleus (Mukherjee et al.[171]). It is, therefore, feasible for the bubble to absorb larger amount of energy, leading to higher departure diameter. The same can be confirmed from Fig. 19(a-b). A reduction in the contact angle (θ_c) from 64.74^0 to 52.23^0 inflicts a noticeable change to the shape at the instant of departure, as well as hints towards a possible shift in the flow regime altogether. While $\theta_c = 52.23^0$ yields smaller bubble, leading to the bubbly flow pattern, the other one produces an elongated bubble, which tends to slide along the surface initially, and then approach the slug flow regime. The effect of the contact angle on the departure diameter is summarized in Fig. 19(c). D_d increases almost linearly with θ_c and an augmentation of about 17^0 in θ_c enforces more than 12% rise. An increase in heat transfer area also enhances the bubble growth force, which tends to resist the departure. Consequently the average bubble release period steadily increases with θ_c.

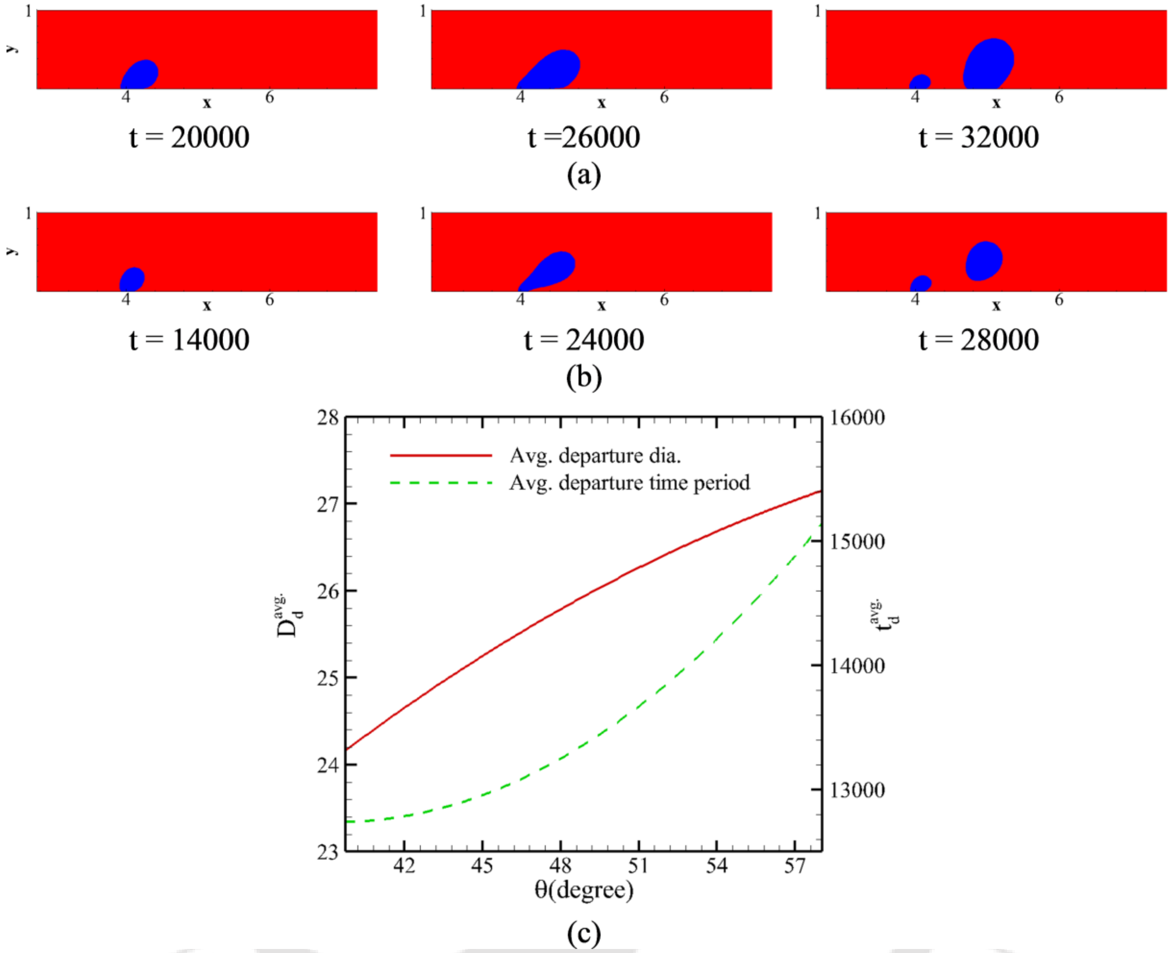

Fig. 19 Effect of surface wettability on the bubble characteristics at the instant of departure; the snapshots of bubble growth till departure for (a) $\theta_c = 64.74^0$ and (b) $\theta_c = 52.23^0$, clearly shows that the departure diameter increases with the contact angle. (c) The variations in average bubble departure diameter and average bubble departure time with the contact angle (θ_c)

Periodic dewetting and rewetting of the heated surface is another common phenomenon in conjunction with flow boiling. During the bubble growth, liquid phase converts to vapor at the microheater surface, pushing liquid away from it, which is referred as dewetting. On initiation of necking, however, liquid is allowed to rush back towards the middle of the heater, thereby rewetting it again, which leads the path towards the next nucleation. This repetitive pattern with the three-phase contact line is clearly visible from Fig. 20, in terms of the temporal evolution of its length (L_t). As already explained, vapor phase covers larger area with the increase in the contact angle, causing an obvious increase in the length of the three-phase contact line. L_t increases from a peak value of about 6.8 for $\theta_c = 52.23^0$ to close to 10 for $\theta_c = 64.74^0$. We can, therefore, claim that the present algorithm is capable of efficiently capturing the effect of surface wettability as well.

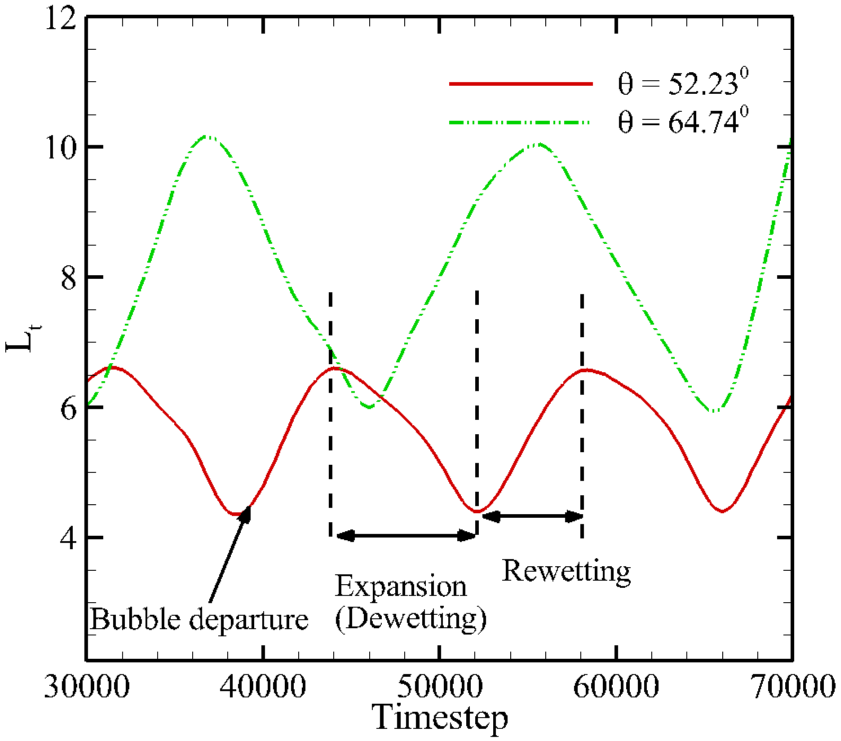

Fig. 20 Effect of the contact angle on the movement of the three-phase contact line of the growing bubble

3.9 Summary

The entire thermohydrodynamics associated with flow boiling in narrow channels, involving nucleation, growth and departure of the bubble at the microheater, and subsequent adoption of bubbly or slug flow regimes, have been aptly illustrated. Both the departure diameter and ebullition period of a bubble at the nucleation site are dependent on the inlet velocity and wall superheat. Present algorithm is able to capture their effects quite logically, while also being consistent with the available literature. We have compared the bubbly and slug flow regimes in terms of the bubble growth pattern and departure characteristics. Pressure drop across the channel and heat transport characteristics exhibit a repetitive pattern, which is also a rational observation. Increase in wall superheat or reduction in mass flux tends to convert the flow domain from single-phase to bubbly to slug, which is amply demonstrated through a qualitative flow regime map. Finally, the effect of surface wettability in terms of the contact angle has also been discussed.

Chapter 4

MRT-LBM Simulation of Condensation on Horizontal Nanostructured Surface

4.1 Introduction

The primary objective of the present study is the exploration of the effect of the solid substrate morphology and its degree of subcooling on the droplet nucleation mode and subsequent development, which can be characterized in terms of the mass condensation rate, nucleation time and the associated heat transfer rate. To accomplish the same, an in-house MRT-SC-LBM code has been developed to simulate condensation on rough surfaces following the mathematical structure detailed in the chapter II. It is imperative to validate the code for both isothermal and non-isothermal situations to reap confidence on its correctness, and the same is presented in the following two sub-sections.

4.2 Model Validation: Laplace Test and Maxwell Area Construction Curve

The process of phase-separation being spontaneous in the framework of the pseudopotential-based LBM, there is no need of adopting additional interface tracking algorithm. Laplace test is a very popular practice followed within the LB community to assess the accuracy of interface generation by following the variation of the inverse droplet radius $(1/r)$ with pressure differential across the interface $(\delta p = p_{in} - p_{out})$ for a specific temperature. According to the Laplace's principle, they must exhibit a linear relationship, with surface tension being the constant of proportionality. Prediction from our numerical model is presented in Fig. 21(a) for $T_R = 0.9$, which aptly demonstrates the successful acquisition of surface tension.

Another indispensable appraisal for any multiphase LBM code is for the predicted magnitudes of the liquid and vapor densities corresponding to the imposed saturation temperature, which must adhere to the analytical levels obtained from the Maxwell area construction rule, in order to corroborate the thermodynamic consistency of the numerical structure, as discussed earlier. We have, therefore, performed a static droplet test for a wide range of the reduced temperature (T_R) and consequent predictions are available in Fig. 21(b). There is no perceptible difference between the analytical and numerical magnitudes of ρ_R^v and ρ_R^l even when the reduced level of saturation temperature is around 0.65, which sufficiently encompasses the scope of the present study, thereby substantiating the accuracy of the developed computation setup for exploration of multiphase flows.

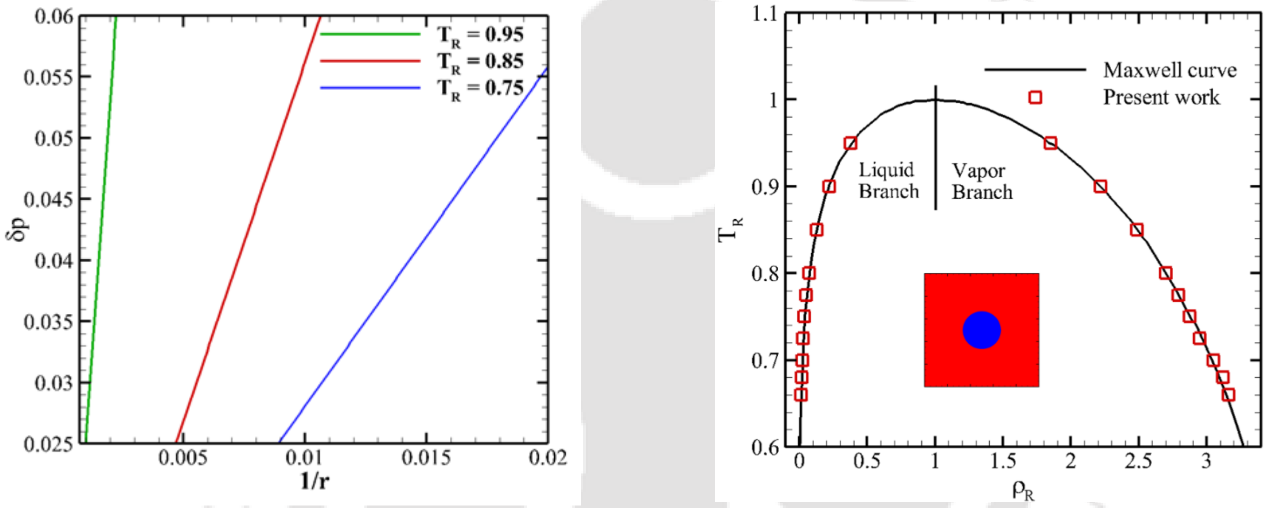

(a) (b)

Fig. 21 (a) Laplace test: Inverse of the radius $(1/r)$ of the static droplet (shown in inset) shows linear relationship with pressure differential across the interface $(\delta p = p_{in} - p_{out})$ for three different T_R values; (b) Maxwell area construction rule: excellent conformity between the analytical and numerical coexisting density values for both the phases even for $T_R < 0.7$

4.3 Model Validation: Nusselt's Falling Film

Next we apply the in-house code to simulate the seminal problem of Nusselt's falling film, in order to perceive its capability in replicating condensation heat transfer. Here we have a vertical flat plate of temperature T_w maintained in contact with saturated vapor of temperature $T_s\,(T_s > T_w)$. Owing to the subcooled condition of the plate, vapor condenses on it and the condensate liquid flows downwards under the influence of gravity, gradually leading to the formation of a steady liquid film on the surface.

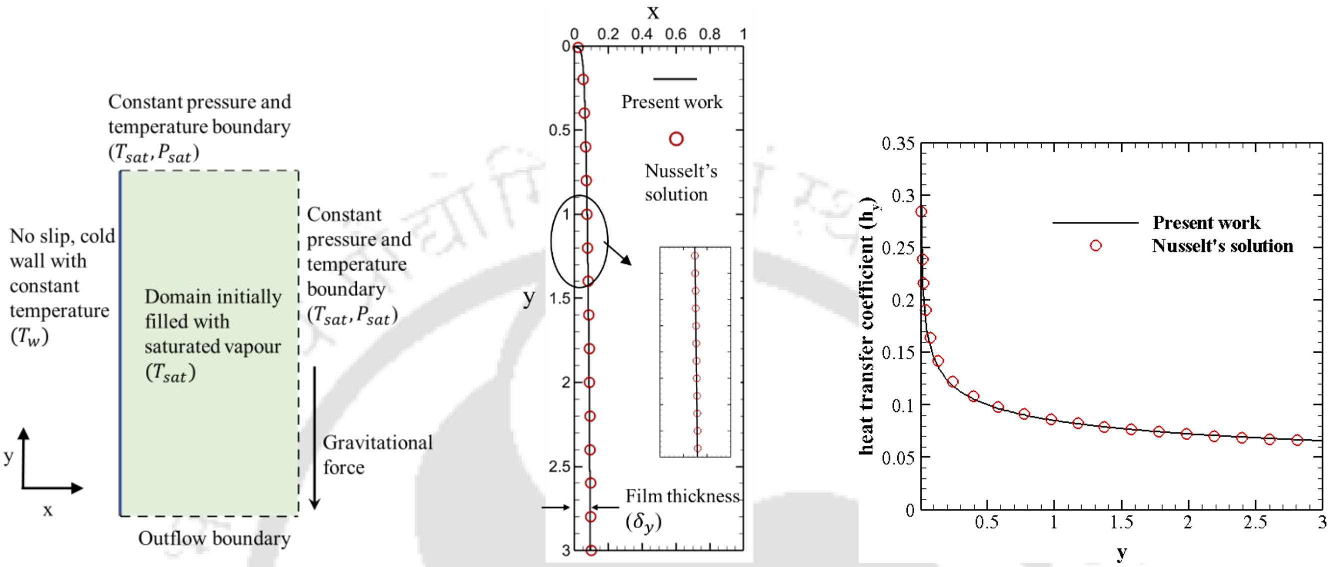

(a) (b) (c)

Fig. 22 (a) Schematic representation of the computational domain to analyze condensation on a vertical subcooled wall; Variations in (b) condensate film thickness and (c) local heat transfer coefficient along the surface of the plate, and comparison with the Nusselt's analytical solution[2]

Analytical solution for this particular scenario was furnished by Nusselt to foretell the film thickness at any location of the plate in terms of the fluid properties, and initial and boundary conditions as,

$$\delta_f(y)=\left[\frac{4\mu_l k_l (T_s-T_w)\,y}{g h_{fg}\rho_l(\rho_l-\rho_v)}\right]^{1/4} \tag{56a}$$

where μ_l is the viscosity, k_l is the thermal conductivity of the saturated liquid, g is gravitational acceleration, h_{fg} is the latent heat for condensation and ρ is density, and the subscripts l and v are used for liquid and vapor phase. The local heat transfer coefficient at a location y is given as: $h_y = k_l/\delta_f$.

The classical theory, however, had several deterrents, such as the non-consideration of subcooling across the film, which can substantially affect the magnitude of the effective latent heat. A well-accepted amendment was postulated by Rohsenow[2], to reshape the latent heat as,

$$h_{fg}^{*} = h_{fg}\left[1 + 0.68\frac{c_{pl}\left(T_s - T_w\right)}{h_{fg}}\right] \tag{56b}$$

which has been found to yield very rational predictions, and hence, we have validated our in-house code with the Nusselt’s theory after incorporating the above correction.

A schematic representation of the relevant computational domain, along with the imposed boundary conditions, is presented in Fig. 22(a). A rectangular domain having 120×360 lattices is considered, which is initially filled with saturated vapor having $T_s = 0.9T_c$. The flat plate is introduced by considering the left vertical boundary of the domain as a no-slip impermeable wall, maintained at $T_s = 0.7T_c$. Following Vasyliv et al.[141], the bottom boundary is treated as an outflow one with embedded Neumann boundary conditions, while the conditions of the top and right boundaries are detailed in the figure. The vapor film thickness and the local heat transfer coefficient along the wall are compared with the respective analytical solutions in Fig. 22(b) and (c) after attaining steady state. Here the film surface is identified as the contour of the average density of both the phases. Excellent degree of conformity with the theoretical solution can be observed for both the parameters, which authenticates the accuracy of the developed solver for condensation on flat surfaces, and can now be used to reconnoiter the effect of surface roughness on the droplet nucleation in the next sub-section.

4.4 Formulation of the Computational Problem

The details of the computational domain under deliberation are delineated in this section, along with the adopted initial and boundary conditions to be introduced into the numerical framework. As shown in Fig. 23(a), we have deliberated over a square domain represented by 240×240 lattices, which is initially filled with saturated vapor having $T_{R,sat} = 0.9$. The bottom edge of the domain simulates a no-slip isothermal wall, whereas the side boundaries are considered to be periodic following Liu and Cheng[82], The top boundary is assumed to represent the far-field condition, which is ensured by imposing the saturation temperature and pressure here. All the mentioned conditions are illustrated in the figure as well for ease of comprehension. A cold spot of length $L_{cold} = 40$ lattice nodes, sustained at the subcooled temperature of $\left(T_{R,cold} < T_{R,sat}\right)$ is placed at the center of the bottom wall, which helps initiating the droplet nucleation. Remainder of the bottom surface is continued to be at $T_{R,sat}$ only.

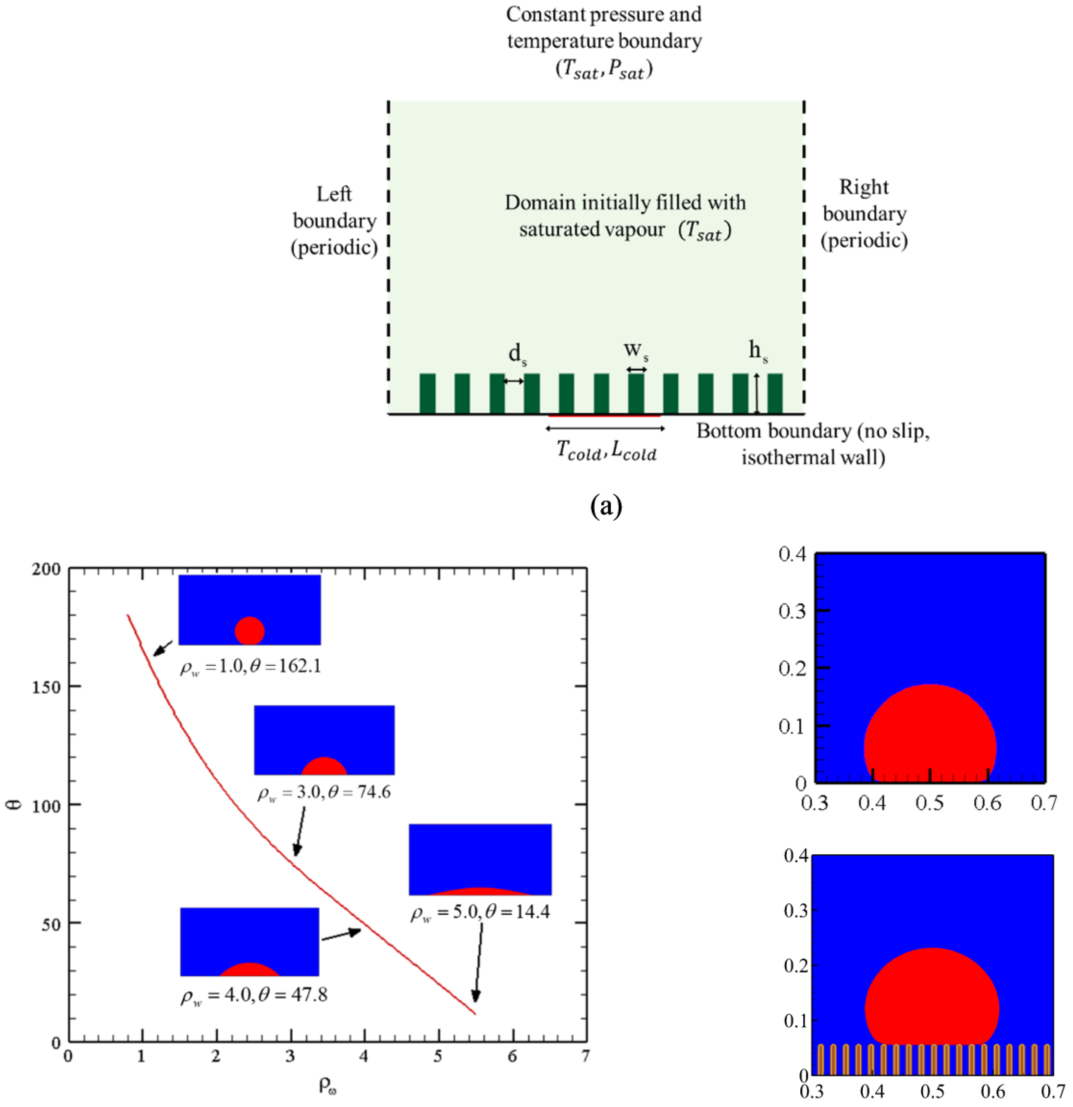

(a)

(b) (c)

Fig. 23 (a) Schematic representation of the computational domain under consideration, along with the imposed initial and boundary conditions; (b) Variation of the static contact angle (θ) with false wall density (ρ_w); (c) Static droplet on a plain surface (top figure) with $\rho_w = 1.75$, and on a rough surface (bottom figure) with specific roughness configuration $(w_s = 2, d_s = 3, h_s = 15)$. Static contact angle for the plain surface continues to be 124^0, whereas that enhances to 151^0 on the rough surface, rendering it to behave as superhydrophobic.

Relevant literature in the domain of wettability modulation of rough surface suggest that, with the contemporary manufacturing technology, the highest achievable contact angle of a properly-engineered smooth surface is about 120^{0}[129]. Proper tuning of the morphology of the rough surface is the most feasible option of enhancing the contact angle beyond that ceiling, in an attempt to approach superhydrophobicity. In adherence to various experimental and numerical works[120,130,135,140], we have placed rectangular nano-columns on the bottom wall, dimensional information for which are available in Fig. 23(a). The effect of gravity is discarded from the mathematical structure, as it is expected to be inconsequential at the nanoscale[172]. Heat conduction through the solid wall has also been neglected, considering their small dimension in the upward direction, by specifying the temperature along the entire exterior surface of each of the columns as that of the corresponding portion of the bottom surface.

As referred earlier in Eq. 36a, the effective magnitude of surface tension can numerically be modulated by altering the false wall density (ρ_w). With PR-EOS at $T_{R,sat} = 0.9$, the densities of the saturated liquid and vapor phases are 5.9 and 0.58 respectively. For a choice of ρ_w closer to ρ_l, the contact angle at the three-phase interface is lower, allowing the liquid to wet the surface, whereas with ρ_w approaching ρ_v, the surface advances toward superhyrophobicity. Variation in static contact angle (θ), with ρ_w is presented in Fig. 23(b), which reveals that a change of ρ_w from 1.0 to 5.0 affects a transition in static contact angle from 162.1^{0} to 14.4^{0}. We have maintained at constant magnitude of $\rho_w = 1.75$ throughout the present study, which sets the static contact angle for a droplet on a perfectly smooth surface at $\theta = 124^{0}$, and the same is demonstrated in the top figure of Fig. 23(c). The impact of the presence of nano-columns on the surface is illustrated in the bottom figure of Fig. 23(c). Here the selected surface structure can be characterized to have column width $w_s = 2$, column height $h_s = 15$, and inter-column distance $d_s = 3$, with all dimensions being at lattice scale. Clearly, the resulting droplet resembles the Cassie state, with a measured contact angle of about 151^{0}, hinting toward the superhydrophobic nature of the solid substrate, despite no change in the fluid-solid combination and hence in the associated force of adhesion. With variations in the characterizing dimensions of the nano-columns (w_s, d_s, h_s), it is possible to conceive different magnitudes of the effective contact angle and, therefore, the state of the condensate droplet, which is expected to strongly influence the subsequent hydrodynamics, and the same will be explored from the next sub-section onward.

It is pertinent to mention here that all the results presented and discussed within the scope of the current study are ensured to be independent of the choice of number of lattice nodes through a systematic mesh-convergence analysis. Formation of a Cassie droplet on the surface demonstrated above (Fig. 23(c)) is considered for the same. Three different lattice configurations, namely, 200×200, 240×240 and 280×280 are contemplated, with each producing near-identical droplet shapes, delineated in terms of the thickness of the diffused interface along the vertical centerline, which is measured as the width of the zone over which fluid density changes from liquid-level to vapor-level. Subsequently, each of the following simulations has been performed using the 240×240 lattice arrangement.

4.5 Hydrodynamics of the Condensate Nucleus

Quéré[129] postulated that the roughness topology of a homogeneous rough surface, i.e., the width, height and spacing of the nano-columns mounted on the surface, can modify the apparent wettability of the surface itself, coercing alteration in the shape and demeanor of the droplet sitting on it. As demonstrated by Aili et al.[173], if the characteristic dimension of the nano-structures is comparable with that of the droplet nucleus, nucleation can get initiated either on the tip of the columns, or inside the cavity separating the columns, depending on the energy barrier created by the intrinsic wettability of the surface and geometrical shape of the nucleation site. The final shape of the condensate droplet during condensation on rough surface (Cassie/Wenzel) has been reported through several recent experimental studies[3,173], while remaining restricted only to the theoretical appraisal of the nucleation characteristics owing to the lack of proper visualization techniques. One important inference from the available literature[133,173] is to identify the change in the free energy during the phase-change process as a primary contributor toward the recognition of the initial nucleation sites. Nucleation is most likely to be triggered at the location having the lowest level of free energy associated with the vapor-liquid transition. As per the classical nucleation theory[173,174], the free energy of heterogeneous nucleation at the three-phase interface is the summation of the three surface energies associated with each pair of phases, which consequently are associated with the continuous creation and extinction of the respective surfaces. For the nanostructured surface with densely-packed columns, the solid-liquid interfacial area is greater, necessitating larger energy requirement to form the solid-vapor interface interior to the crevices of the columns, thereby exacerbating the energy barrier. That allows the initiation of droplet nucleation at the tip of the columns, where the energy barrier is weaker because of the smaller solid-liquid interfacial area. Increase in the inter-column spacing reduces the solid-liquid contact area, consequently lessening the energy barrier in the gaps, and so droplet nucleation on the base surface is more feasible, thereby facilitating the appearance of both the Cassie and Wenzel droplet shapes with variation in the spacing.

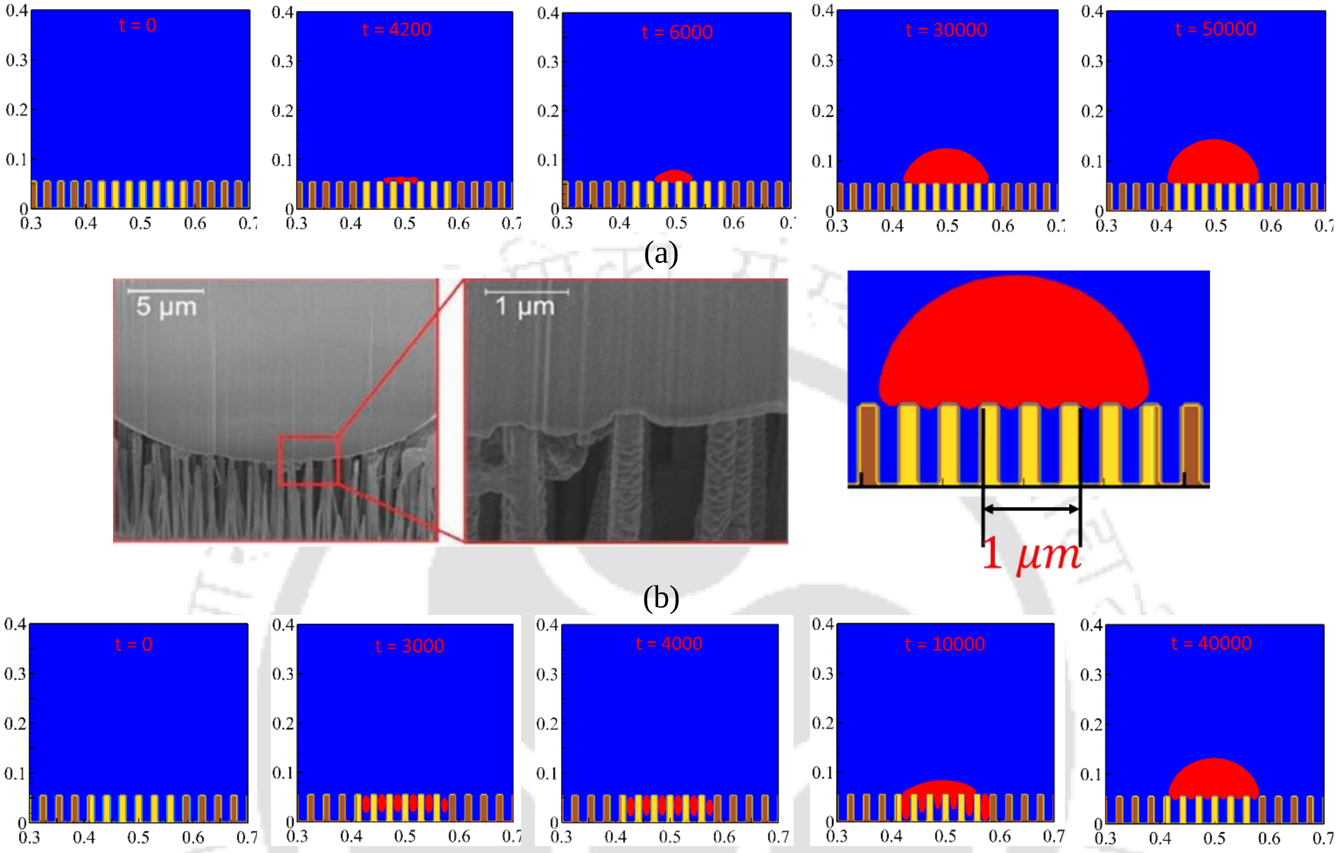

(a)

(b)

(c)

Fig. 24 Cassie droplet: (a) Sequential snapshots in top nucleation mode at different time levels; (b) Qualitative comparison of the present predictions with the experimental results of Rykaczewski et al.[3]; (c) Sequential snapshots in side nucleation mode at different time levels. Here all mentioned values are in respective lattice units. The blue and red colors correspond to liquid and vapor phases respectively, and the cold spot on solid surface is marked in golden color.

One of the primary advantages of the pseudopotential based LBM is the spontaneous phase separation, without obligating any assumption of an initial interface, unlike in conventional CFD-based tools or certain other multiphase LBM models. The adopted PR-EOS controls the coexisting density of both the involved phases. Once the temperature at any lattice node falls below the saturation temperature and sufficient amount of energy is possible to be extracted from the neighborhood of that location, the solver imposes the vapor density value through the EOS, thereby actualizing vapor-to-liquid phase transition.

That allows proficient simulation of the local-level microdynamics of the process of droplet nucleation, and we have used that to our advantage to envisage the role of roughness patterns on the droplet state. The simulation setup has already been detailed in the earlier section. We have maintained a fixed value of $T_{R,cold} = 0.8T_c$ for the remainder of the work, unless stated otherwise.

The first configuration is selected to have the specifications of $w_s = 3$, $h_s = 15$, and $d_s = 3$ lattice units (lu), and consequent nucleation and growth of a Cassie droplet, nucleating at the top of a nano-column, is presented in Fig. 24(a). As explained before, here the arrangement of the structures is too dense to allow phase change inside the cavities, particularly with the entire domain being filled with the vapor phase at $t = 0$. Tiny droplet nuclei are visible at the tip of the adjacent columns around $t = 4200$ lu, which agglomerate into a distinct condensate droplet sitting on the columns around $t = 6000$ lu. with the baseline of the drop having nearly a flat shape. With continuous removal of energy through the cold spot, the condensate droplet keeps on growing in size, because of the persistent movement of mass across the interface toward the liquid-side, and a substantially bigger drop is visible at $t = 50000$ lu. It is quite obvious that such a droplet can be removed relatively easily from the rough surface, and therefore, nanostructured surface instigating top nucleation mode can be viewed to exhibit superhydrophobic nature.

A qualitative comparison is drawn with the experimental pictures reported by Rykaczewski et al.[3] in Fig. 24(b) regarding the formation of a Cassie droplet on a solid substrate structured with nanoarrays. One lattice unit of length with present configuration is equivalent to a length scale $0.5\mu m$ as per the macroscopic system, which allows us to place three nanocolumns over a physical length of $1\mu m$, as marked in the figure, and it is the same number displayed with the surface used by Rykaczewski et al.[3]. We, therefore, have adhered to the same length scale as of theirs, which has guided us to the top nucleation mode, establishing the consistency of the numerical prediction with physical microdynamics. Both the experimental and numerical droplets portray very flat nature of the bottom interface, in contact with the columns, which can further be demonstrated following the displacement of the top and bottom interfaces along the vertical center-line, presented in Fig. 25(c). Here the continuous black line corresponds to the upper edge of the interface intersecting that vertical plane, whereas the dotted black one refers to the lower end. Clearly, the lower surface always remains in contact with the column, as is unveiled by the straight line. The upper end, however, continually ascends, indicating the growth of the nucleus, as observed earlier in Fig. 24(a).

Increase in the spacing between the columns can allow nucleation on the vertical surfaces of the interior of the columns to the cavities, initiating the side nucleation mode. It is illustrated in Fig. 24(c), where the surface morphology is specified as $w_s = 3, h_s = 15$, and $d_s = 4$ lu notifying only a single lattice unit of change in the width of the crevices compared to the previous geometry. Here the droplet nucleation starts at a vertical distance of 11 lu from the base surface at t = 3000 lu time, as shown by the green lines in Fig. 24(c). Initially, the droplet grows in both directions, with the bottom interface moving toward the base. Around t = 4000 lu, the upper interface reaches the tip of the column, which restricts any further downward displacement of the bottom edge of the interface. The lower interface, which is yet to touch the base, in fact, starts climbing upward after a short while, till arriving at the tip of the column and stays there, impressing a Cassie state of the nucleus from that instant onward. Zhang et al.[130] attributed such ascension of the condensate droplet, despite the side nucleation, to the Laplace pressure difference. As the upper surfaces of the individual nuclei merge with each other to form a bigger one, there is a reduction in the local radius of curvature in that part of the interface. Now the pressure differential across the interface being inversely proportional to the radius and the ambient pressure being a constant one, there will be a decline in local pressure in the upper section of the droplet. The magnitude in the lower part, however, remains unchanged, resulting in an upward thrust capable enough of dragging each of the tiny droplets out of their respective cavities, and allowing the formation of a single Cassie droplet settled on the tip of the nano-structures. From both Figs. 24(c) and 25(c), we can ascertain that the extraction of the droplets starts around t = 8110 lu and completes approximately at t = 12980 lu. A growing Cassie droplet is clearly visible at t = 40000 lu, indicating the attainment of superhydrophobicity even with side nucleation.

A discernible change in the state of the droplet nucleus can be realized with another lattice unit of increase in the width of the cavities $(d_s = 5lu)$ The initiation of phase change still continues to be in side nucleation mode, albeit starting at a vertical position of about 7 lu, lower than the previous case, as can be ascertained from the red lines plotted in Fig. 25(c). Such change is positioning can possibly be attributed to the competition between the prevailing energy barrier and heat transmission from the cold wall. As a consequence, the bottom interface touches the base surface at t = 2550 lu, with the upper edge still languishing about 5 lu below the tip of the columns, thereby not allowing any coalescence of the individual nuclei. Hence, there is no unbalanced Laplace pressure to lift the droplets and the same adheres to the base, as well as the vertical walls of the columns, owing to the adhesive forces (Fig. 25(a)). That is also evident from the displacement of the lower part of the interface, which, after a short initial time span, always sticks to the location h = 0. The sizes of the individual droplets get augmented with time because of the transformation of vapor to liquid coming in contact with the cold column walls, eventually stretching out of the cavities around t = 6000 lu and merging with each other to form a single droplet. This, however, always encompasses the columns attached to the cold spot and also remains in contact with the base surface, which is the precise characteristics of the Wenzel state. It leads to the filmwise condensation, in contrast to the dropwise condensation evident with the Cassie state, therefore tending more to the hydrophilic nature of the surface despite the presence of the nano-structures.

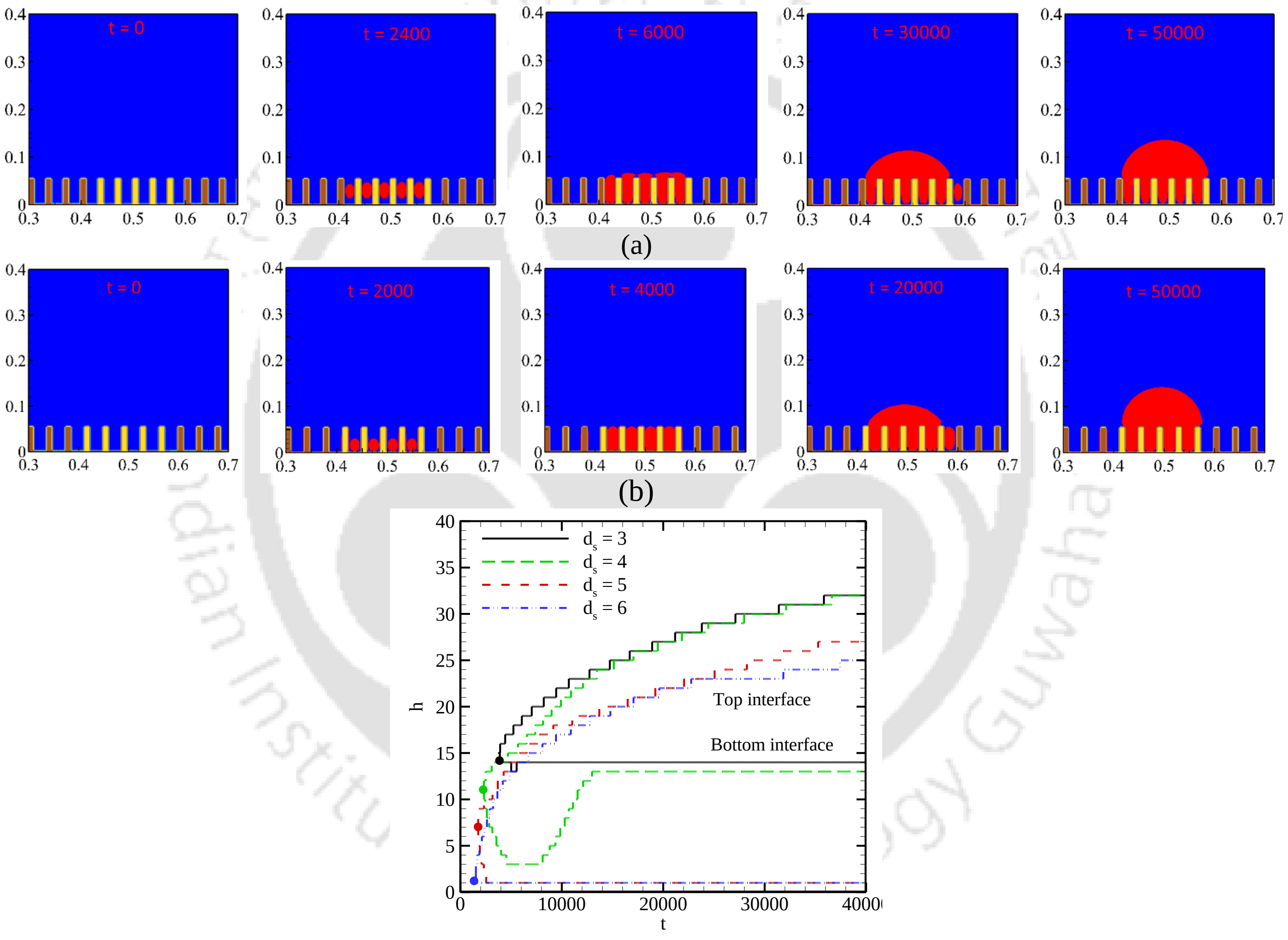

(a)

(b)

(c)

Fig. 25. Wenzel droplet: (a) Sequential snapshots in side nucleation mode at different time levels; (b) Sequential snapshots in bottom nucleation mode at different time levels; (c) Movement of the top and bottom interfaces of the condensate droplet along the vertical centerline

With any further enhancement in the inter-column spacing nucleation may get initiated from the base surface itself. One such scenario is presented through the snapshots in Fig. 25(b) for $d_s = 6$ lu and also by the temporal displacement of the two representative points on the interface in Fig. 24(c) (blue line). Lower surface of the droplet never leaves the base since nucleation, whereas the upper edge creeps out of the cavity after t = 4000 lu, gradually developing into a Wenzel drop, and consequent condensate film on the surface. Such filmwise condensation, generally, is not favored in commercial heat transfer appliances, as it deteriorates the rate of energy transmission owing to the loss of the contact between the subcooled surface and saturated vapor. The superiority of dropwise condensation in this precise context, because of the prompt removal of the condensate drop and continuity of the latent heat transfer, is well documented in literature[111,123,133] accentuating the role of the nano-columns in resolving the nature of condensation.

4.6 Interfacial Mass and Energy Interactions

In an attempt to acquire precise perception about the rate of interfacial interactions with either state of droplet nucleation, we analyze the rate of surface heat transfer at the cold spot $q = -kA_{cold}\, {}^{\partial T}\!/_{\partial n}$ and instantaneous mass of condensate (m_l) with time for each of four cases explored in the previous subsection. Here, k is the thermal conductivity of the fluid in contact with the cold surface and $\hat{n}$ is the direction normal to the same plane. Li et al.[142] discussed the trend regarding the same parameters during condensation on rough surfaces with variable wettability and identical geometric morphology. Adhering to their conjecture and also following the microdynamics of condensation at the cold spot observed during the present study, we can identify four distinct stages of heat transfer.

- As the temperature of initially-saturated vapor starts decreasing with it loosing energy to the subcooled solid, consequent temperature differential ΔT reduces. Prior to the initiation of phase transition, only sensible mode of heat transfer is possible, and that being proportional to ΔT, overall rate of heat transfer falls over a brief period.
- Once sufficient level of vapor subcooling has been achieved, condensation is instigated and latent mode of heat transfer is materialized, leading to a sharp rise in the rate of energy interaction. Small amount of sensible heat transfer also commences to the newly-appearing liquid phase.
- As the droplet grows in size, the cold spot increasingly gets covered by liquid. The consequent temperature differential between the surface and the adjacent fluid is much lower now, which

hinders energy transmission, causing a consequent decline in heat transfer(q). The proportion of latent mode in overall heat transfer diminishes rapidly with time.

- Eventually the steady-state scenario is achieved, with the cold spot being fully covered by liquid, and heat absorption from the vapor to the substrate is possible only through the liquid layer, which offers reasonably high thermal resistance.

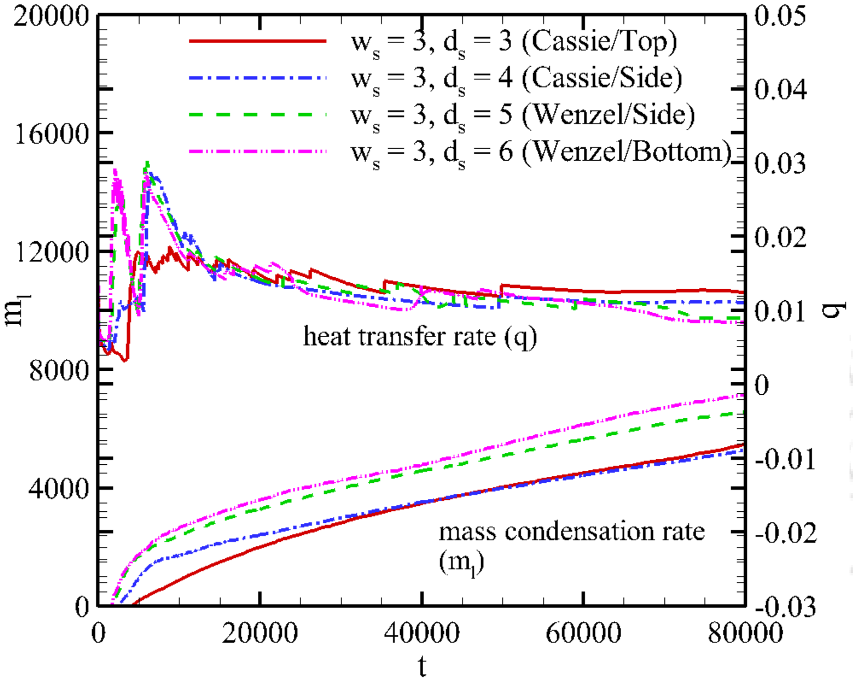

Fig. 26 Temporal variations in heat transfer rate at the solid surface (q) and accumulated mass of the condensate (m_l) for all the cases presented in Figs. 6 and 7, with different inter-column spacing (d_s) and identical dimensions of individual columns $(w_s = 3, h_s = 15)$.

Similar nature of transient progression can be found in Fig. 26 for the present study as well. The rate of heat transfer decreases over a short time span till the inception of nucleation, characterized by a rapid upsurge to attain a maxima, and then falls continuously with a moderate gradient. The magnitude of $q_{\max}$ is quite similar in all the cases apart from the top nucleation mode, where the active contact area is significantly smaller than the side or bottom nucleation cases. In fact, Cassie droplet in top nucleation mode does not exhibit any sharp decline in q beyond the peak. Interestingly, two peaks can be observed in both the modes of Wenzel state. While the first one conforms to the appearance of the inaugural liquid nucleus, the second one possibly emanates with greater contact area being active. The steady-state magnitude of q with Cassie drop in top nucleation mode is slightly higher than the rest, as a consequence of the lesser thickness of the liquid layer.

The rate of condensation follows the profile of q. It is significantly high during the initial phases of nucleation and droplet growth, as direct latent energy absorption is possible at the cold spot. Quéré[129] pointed out that the increment in the inter-column spacing lowers the apparent wettability of the solid substrate, as explained earlier using the concept of Laplace pressure. The energy barrier associated with the vapor-to-liquid phase transition is weaker with reduced wettability and hence, favorable for condensation, thereby allowing earlier droplet nucleation and greater rate of mass condensation with declining hydrophobicity of the cold surface. That argument is consistent with our observation, as d_s is varied from 3 to 6 lattice units in Fig. 26. The Wenzel state of nucleation is found to be associated with early commencement of phase transformation, as well as, greater mass of condensate accumulation with time, compared to the Cassie state. The filmwise condensation is classically known to yield considerably lower rate of heat transfer than the dropwise mode[123,124].

All the discussion till this point has revolved around the role of inter-column spacing on the nucleation characteristics. The repercussion of change in other relevant dimensions of the nano-structures is not that substantial, primarily because they don't significantly impact the apparent wettability of the surface. Several such cases are demonstrated in Fig. 26, where the ones in the top row illustrate the impact of column height (h_s) while the bottom ones represent the implications of change in width (w_s). The height (h_s) clearly has inconsequential impression on the rate of interactions for a Cassie droplet $(d_s = 3lu)$. The rate of mass condensation for a Wenzel droplet, however, is substantially enhanced with rise in h_s in Fig. 27(b). The rationale lies with the accretion in the area available for heat extraction. While the Cassie droplet is in contact only with the tip of the column, which remains unchanged with any alteration in the height, the Wenzel droplet wets the base surface, as well as the side walls of the columns. With $h_s = 20$ lu, it is possible to offer wider cold spot to the saturated vapor, emanating noticeably higher m_l. The effect of the column width is even less recognizable for both the droplet states. The rate of condensation is slightly lesser for the Wenzel drop with wider columns, as the available base area is lesser.

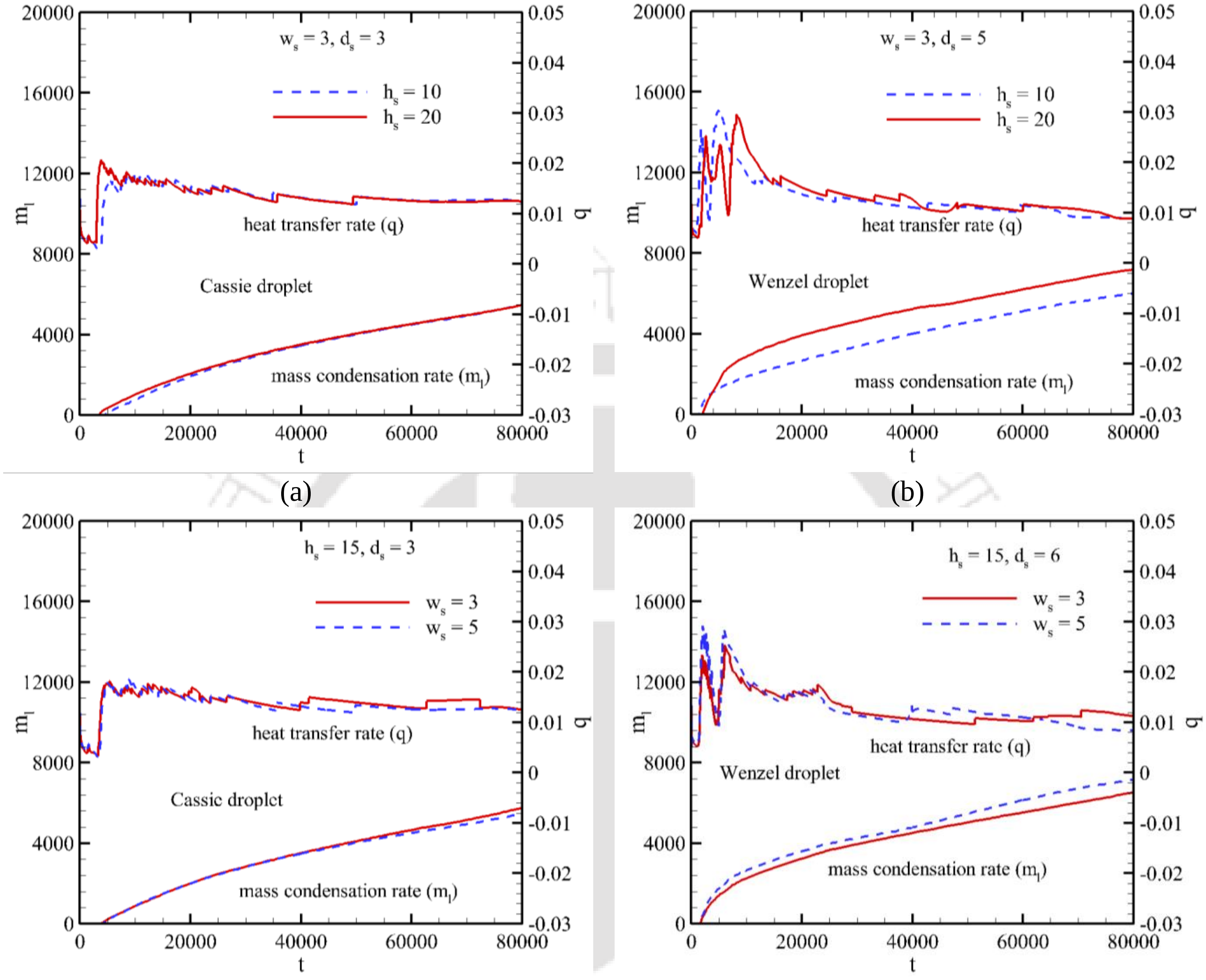

(a) (b)

(c) (d)

Fig. 27 Temporal variations in heat transfer rate at the solid surface (q) and accumulated mass of the condensate (m_l): Effect of column height (h_s) on (a) a Cassie droplet $(d_s = 3)$ (b) a Wenzel droplet $(d_s = 5)$; effect of column width (w_s) on (c) a Cassie droplet $(d_s = 3)$ (d) a Wenzel droplet $(d_s = 6)$

4.7 Nucleation Time

As the apparent wettability of a nanostructured surface is modulated by adjusting the dimensions of the nano-array, the time required for nucleation t_n is also attuned accordingly. Here the nucleation time has been numerically estimated as the time required for the liquid phase to occupy ten lattice cells since the very inception of simulation. Hydrophilic surface has a greater affinity to the liquid phase, providing additional impetus towards condensation, and therefore, any change leading toward hydrophilicity helps in early nucleation. The same can be affirmed following the trends evident in Fig. 28. Substantially greater time is required to initiate the Cassie droplets, particularly in the top nucleation mode, as the area consequent to heat transfer is the smallest among all the four orientations. Appearance of liquid phase is almost instantaneous in the Wenzel state, again owing to the availability of wider cold surface. Time requirement increases with the column height till a certain level, beyond which it becomes invariant for any kinds of nucleation (Fig. 28(a)). Nucleation time is found to be decreasing with column width (w_s) for the Cassie droplet in top nucleation mode from Fig. 28(b). As the Cassie drop engages only with the tip of the column for energy interaction, any increment in column width provides greater contact area between the solid and vapor, and hence an early incipience of condensation. For side or bottom nucleation modes, however, there is hardly any change in t_n with w_s for very obvious reasons.

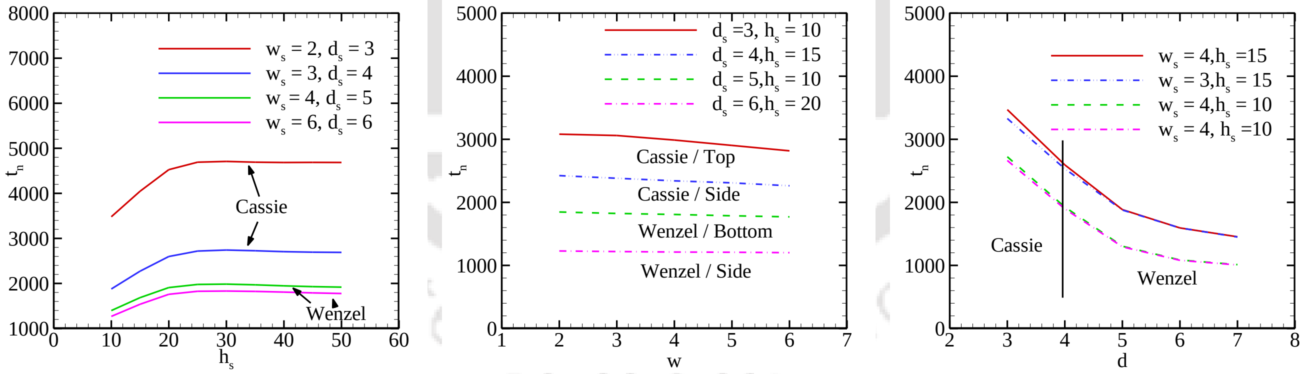

(a) (b) (c)

Fig. 28 Variation in nucleation time (t_n) with (a) column height (h_s) (b) column height (w_s) (c) inter column spacing (d_s)

Really interesting pattern can be observed from Fig. 28(c) about the effect of the inter-column spacing (d_s). As detailed in the previous sections, a bigger gap between the neighboring columns diminishes the hydrophobic character, promoting the transformation from Cassie to Wenzel state.

Remaining consistent with the tendency of the Wenzel drops to nucleate promptly, steep fall in the nucleation time can clearly be identified for any combination of height and width. Beyond a certain magnitude of d_s, though, the profiles for any types of nucleation become near-horizontal, as the columns are now too far apart from each other to inflict the impact of the nanoarray.

4.8 Phase Diagram

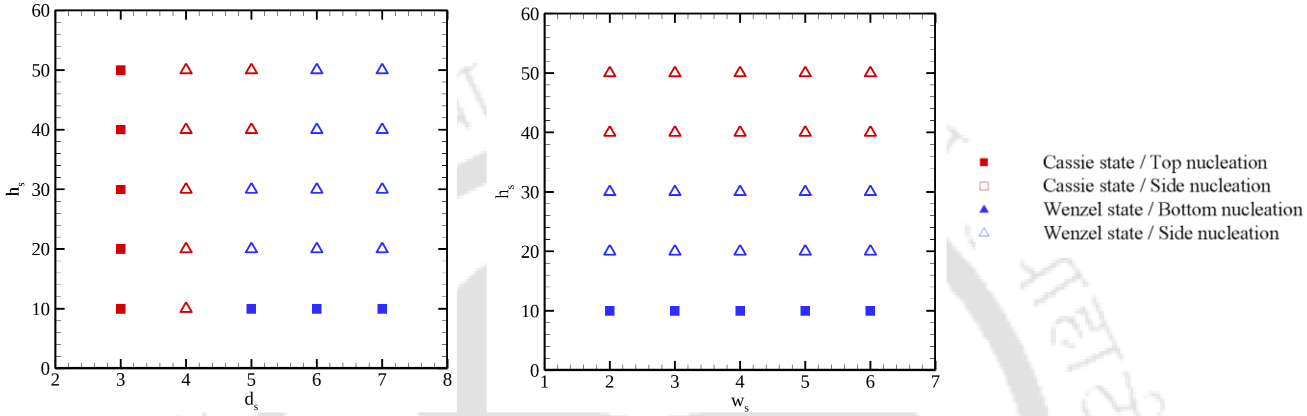

(a) (b)

Fig 29. Phase diagrams encompassing all the four modes of droplet nucleation on a nano-structured surface on (a) $h_s - d_s$ plane with $w_s = 4$ (b) $h_s - d_s$ plane with $d_s = 5$.

In many industrial applications, it is generally preferable to have droplet condensation, to facilitate higher rate of heat transfer and also easier removal of the condensate. Therefore, based on the discussions till this point, it can be inferred that an array of densely-packed taller and slimmer columns is desirable to ensure Cassie droplet in top nucleation mode, and so a superhydrophobic substrate. Certain combinations of intermediate spacing and height can lead to side nucleation, raising the possibility of both Cassie and Wenzel nucleation, depending on the positioning of the lower interface of the droplet at the instant of the upper interface peeping out of the cavity, while a large inter-column spacing always actuates bottom nucleation. In an attempt to accomplish complete cognizance about the possible modes of nucleation for any specific surface morphology, all the explored combinations are summarized in a pair of phase diagrams in Fig. 29. When the columns are very closely-spaced $(d_s \le 3lu)$, phase transition is always happening through Cassie drops in top nucleation mode. With an increase in the spacing beyond that, however, the side nucleation is prompted, continuing to yield Cassie drops over a short range. Quite interesting pattern can be noted following a vertical line drawn at $d_s = 5lu$. Such a spacing leads to

Wenzel drops in bottom nucleation mode for shorter columns $(h_s \approx 10lu)$ and side nucleation mode for intermediate heights. When the columns are reasonably tall $(h_s > 40lu)$, the process of condensation reverts back to the Cassie drops with side nucleation, as the lower interface of a growing nucleus is not able to make to the base surface. With further increase in the spacing, only Wenzel drops, instigating filmwise condensation, is possible, with the mode of bottom or side nucleation being determined by the column heights. As already recognized in the previous sub-section, the width of the column has inconsequential role in adjudicating either the nature of nucleation or the rates of interactions. The same can be reinforced by developing similar phase diagrams for other column widths to identify no perceptible change in the conclusions.

4.9 Effect of Cold Spot Temperature

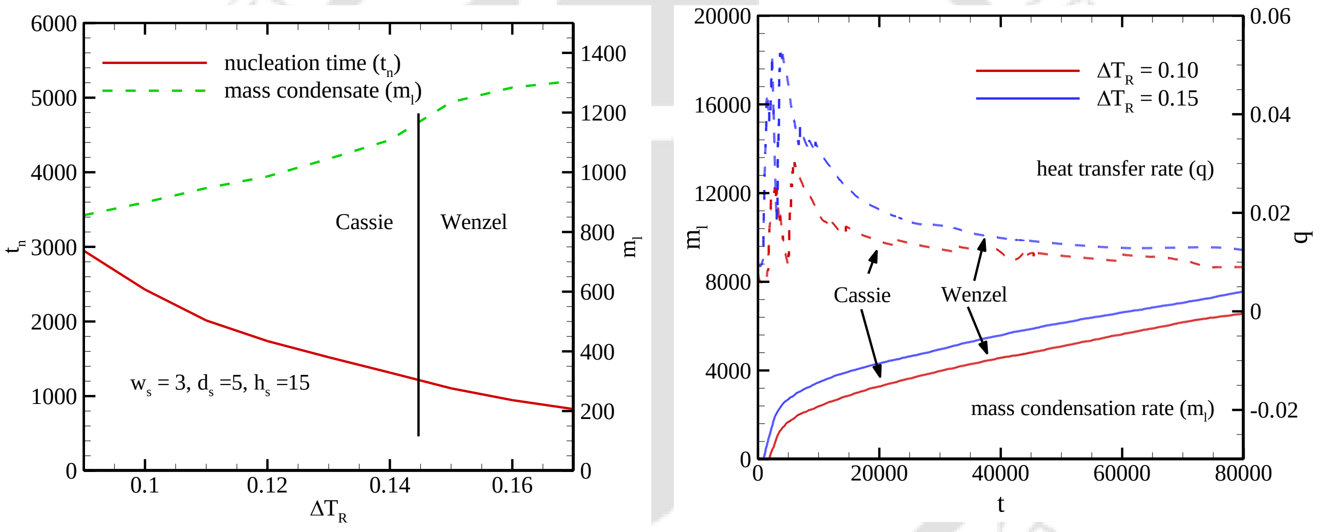

(a) (b)

Fig. 30(a) Effect of the degree of subcooling (ΔT_R) on the nucleation time and total mass of condensate accumulated till t = 50000, with the droplet changing from Cassie to Wenzel state for high ΔT_R; (b) temporal variations in heat transfer rate (q) and mass of condensate (m_l) for two different cold spot temperatures.

One of the prime novelties of the present work, in retrospect to the existing LBM studies on condensation[130,140], is the consideration of thermal non-equilibrium within the condensate layer. A selected section of the base surface, one-sixth of the total length, is imposed with lower temperature, while maintaining the remainder at the saturation value, thereby creating a cold spot and hence, a stimulus for energy interaction between the saturated vapor and the surface structures. Each of the earlier results corresponds to a low temperature of $T_{R,cold} = 0.8lu$, inflicting a degree of subcooling of $\Delta T_R = 0.1lu$. To ascertain the influence of this temperature, $T_{R,cold}$ has been regulated over the range of 0.81 to 0.73 lu, subsequently administering ΔT_R of 0.09 to 0.17 lu respectively, and associated observations are illustrated in Fig. 30.

Any lowering in the temperature of the cold spot renders greater potential for absorption of energy from the vapor phase and therefore promotes condensation. Consequently, the amount of time required for nucleation continually reduces with rise in ΔT_R, while the mass of condensate accumulated over a certain time span steadily increases, as can be endorsed from Fig. 30(a). Another conspicuous phenomenon to note is the transition from Cassie to Wenzel state for $\Delta T_R \geq 0.15lu$. Our choice of the nanostructured surface for the present set of simulations can be defined with $w_s = 3$, $h_s = 15$ and $d_s = 4$ lu , which yielded Cassie droplet in side nucleation mode for $T_{R,cold} = 0.8lu$, as discussed earlier. For such levels of ΔT_R, the nucleus is forced to climb along the columns toward the tip under the action of the unbalance Laplace pressure. For lower $T_{R,cold}$ though, the rate of generation of liquid is significantly faster, allowing the initial droplet nucleus to experience accelerated growth and fill the cavity up in much lesser time. When ΔT_R swells beyond 0.15 lu, the lower surface of the interface is able to contact the base surface before the top can creep out of the cavities. There is no creation of unbalance in Laplace force as a consequence, facilitating the transition to the Wenzel state, with the droplet adhering to the base surface and side walls of the columnar structures. There is also a change in the amount of condensate mass, with no appreciable deviation in the profile of the nucleation time.

The rates of energy and mass interactions are compared in Fig. 30(b) for two different temperatures of the cold spot. As expected, both are higher for the cooler surface with $\Delta T_R = 0.15lu$, which is associated with the Wenzel state. Noticeably early initiation of the phase transition can be observed for this case, along with substantially higher magnitude of the peak heat flux and much steeper rise in the condensate accumulation rate. It can, therefore, be concluded that the surface temperature can also effectuate critical evolution in the microdynamics of the droplet nucleus, as well as the rate of interfacial interactions, along with the nanostructures. It is preferable to perpetuate a controlled level of subcooling at the cold spot to ensure the superhydrophobic nature.

4.10 Summary

In the present study, we have delved into the intriguing scenario of condensation on nano-structured surfaces, where the nature of nucleation and associated thermalhydraulics are closely regulated by the specifications of the surface architecture. While systematic experiments have immensely contributed in comprehending the corresponding visual nature of droplet nucleus, detailed numerical analyses are necessary to unearth crucial information about the local transport characteristics, and the mesoscopic framework of LBM has been employed here. We have adopted an MRT-based LBM structure, in collaboration with the pseudopotential model, to envisage the role of the dimensions of the nano-columns mounted on the bottom surface of a rectangular domain. The computational domain is initially assumed to be filled up with saturated vapor and a cold spot has been imposed at the center of the base surface to facilitate phase transition. The most important observation is the attainment of superhydrophobic conditions for certain combinations to the column dimensions and inter-column spacing, with the later parameter being earmarked as the most influential one, despite the static contact angle with the selected fluid-solid pair on a smooth surface being only around 124^0. Both the Cassie and Wenzel states of nucleus are possible to be achieved, with sequential appearance of the top, side and bottom mode of nucleation with gradual widening of the inter-column gaps, primarily owing to the consequent modulation in the apparent wettability of the cold spot. Superhydrophobicity is associated with the Cassie state, which allows the droplet to sit at the tip of the columns, even during side nucleation, thereby expediting easy removal of liquid. Influences of both the height and width of the columns are found to be near-inconsequential on the overall characteristics, as neither sufficiently affect the apparent wettability and associated imbalance in Laplace pressure. Reduction in the temperature of the cold spot also promotes early condensation, with Cassie-to-Wenzel transition for a greater degree of subcooling.

Four distinct stages of heat transfer can be recognized, with each according to a different proportion of sensible and latent energy transmission to varying fluid phases. The Wenzel state is found to demonstrate early nucleation and larger amount of condensation, with a particularly steep gradient of condensate formation during the early stages of the process. It also displays greater surface heat flux, uniquely characterized by two peaks of near-identical magnitude. The Cassie state with side nucleation can attain a similar level of maxima in heat flux, albeit at a noticeably later instant, leading to a lower time-average value. Heat transfer rate (q) for Cassie droplet in top nucleation mode, however, is consistently the inferior one, specifically during the first three stages of energy interactions, because of the limited contact area. All the four condensation scenarios are summarized through couple of phase diagrams, which aid easy identification of the mode of nucleation from the knowledge of the surface topology, and subsequent characterization of the local thermalhydraulics of the phase-change process.

Chapter 5

MRT-LBM Simulation of Condensate Flow Dynamics on Microstructured Surface

5.1 Introduction

The primary objective of this work is to analyze DWC and FWC on surfaces with different textures and inclinations. The first part of this section provides validation of the in-house code through isothermal and thermal benchmark problems. The next part is dedicated to a thorough analysis of DWC and FWC through temporal snapshots of the simulation domain and corresponding condensate mass accumulation and heat transfer rate. MRT-SC-LB scheme is used here for the numerical computation, which is already explained in the formulation section (chapter 2). The benchmarking of the developed in-house code for condensations problems has already been presented in chapter 4. As the numerical framework used here is the same as the previous one, benchmarking results are not shown here to avoid repetition.

5.2 Simulation Setup

In this work, the condensation problem on a rough surface is studied for different roughness parameters and surface inclinations. The computational domain, and initial as well as boundary conditions of the problems are discussed thoroughly in this section. A rectangular domain initially filled with dry saturated vapor at reduced temperature $T_R = 0.9$ is taken for the simulations of the condensation problem on the rough surface. The schematic diagram for the problem is shown in Fig. 31. The boundary conditions used for the present numerical computations are as follows: no-slip, isothermal wall are considered as the bottom boundary of the channel. Following the work of Cheng et al.[82], periodic boundaries are considered at the left and right edges of the domain. The top boundary is assumed as a free surface where pressure and temperature values are constant. For a quick understanding of the reader, all the boundary conditions are mentioned in the schematic diagram depicted in Fig. 31. The surface inclination is realized through the inclination angle θ. The surface becomes vertical when $\theta = 90^0$ and it becomes horizontal at $\theta = 0^0$. Single or multiple cold spots of various lengths related to the specific problems are considered at the bottom wall. The sections with different temperature values at the bottom wall are represented by different colors. Their corresponding length, distance from origin and temperature values are different for separate problems, and they will be provided in the relevant sections.

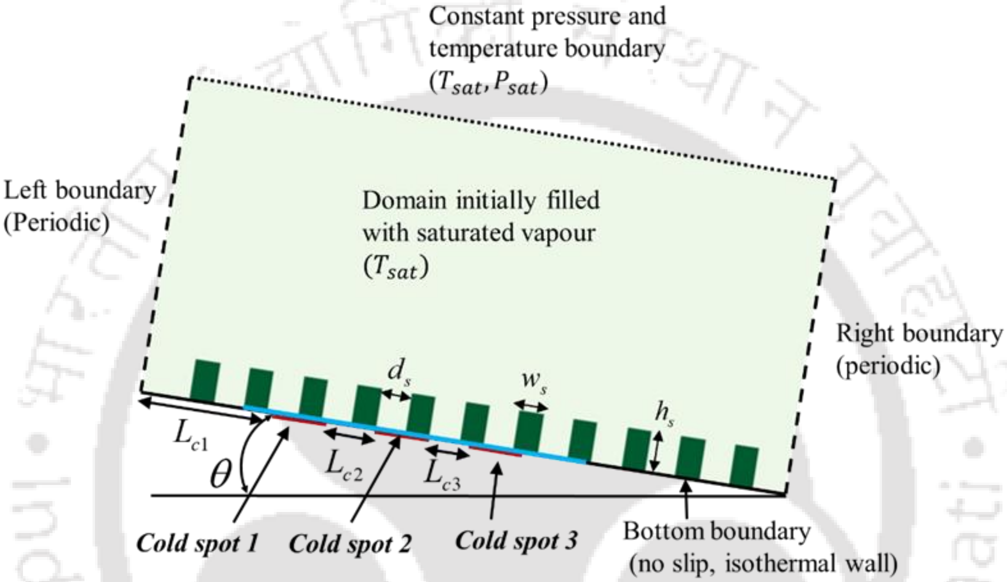

Fig. 31 Schematic diagram of the computational domain

To mimic a rough surface, microscale rectangular texture posts are placed on the bottom wall, whose width, height and spacing are taken as w_s, h_s and d_s respectively. Two surfaces with disparate roughness parameters, i.e. different sizes and spacing of texture posts are considered to study condensation of vapour into Cassie or Wenzel droplets. The two surfaces are designated as GS1 and GS2, and their corresponding roughness parameters are – GS1: $w_s = 2, d_s = 3, h_s = 15$ and GS2: $w_s = 2, d_s = 6, h_s = 5$. The conduction through the solid posts are neglected as considering them makes insignificant changes in the final results. It is described in the formulation section through Eq.(36) that surface wettability force can be tuned by changing the false wall density (ρ_w) value. Relevant literature in the area of wettability modification of rough surfaces[129] suggests that with the available manufacturing technology, the highest contact angle of a properly engineered smooth surface can be modified upto 120^0. Beyond that, proper tuning of the pillars of a rough surface is the most convenient way to make a surface superhydrophobic where the value of the contact angle can be as high as 150^0-160^0. Keeping this data in mind, the false wall density value is taken as $\rho_w = 1.75$ in the present work, which sets the static contact angle at $\theta_s = 124^0$. It is worth mentioning here that if a static isothermal droplet is placed on the surface with roughness configuration GS1, the static contact angle becomes higher than that of the smooth surface. The value of the contact angle is measured as $\theta_s = 150^0$. All the fluid properties are taken for R-134a at initial temperature.

5.3 Cassie and Wenzel State

Querre[129] explained that surface roughness topology of a homogeneous rough surface, i.e. the height, spacing and width of the pillars situated on the surface could modify the apparent wettability of the surface, which results in the change of behavior of a drop sitting on the surface. Zhang et al. [130] showed that if a rough surface has larger pillar height and smaller spacing, the vapor starts nucleating at the top of the texture posts, as it can't penetrate the gap between the surface grooves and remain at Cassie. The behavior of the condensate liquid follows the opposite trend if the post height becomes lower and their gap becomes wider, the liquid starts nucleating from the bottom of the surface, and it conforms to the roughness posts. Ultimately it grows into a larger drop with a low contact angle.

The first snapshot [Fig. 32(a)] represents the initial condition of the domain, where the domain is filled with saturated vapor at temperature $T_R = 0.9$. Li et al.[142] showed that when the situation is favorable for droplet achieving Cassie state, vapor starts condensing at the top of the micropillars. Present results follow the same trend, which can be observed in Fig. 32(b). Pillar height is more and spacing is low for GS1 roughness configuration, and according to the work of Zhang et al.[130], this is the most favorable condition for Cassie droplets. It can be easily observed from the current figure that at time level $t = 7200$ vapor phase has started nucleating on the top of the texture posts. The next figure [Fig. 32(c),] is plotted for temporal instant $t = 50000$, which demonstrates the subsequent growth of the small nucleus into a larger Cassie droplet.

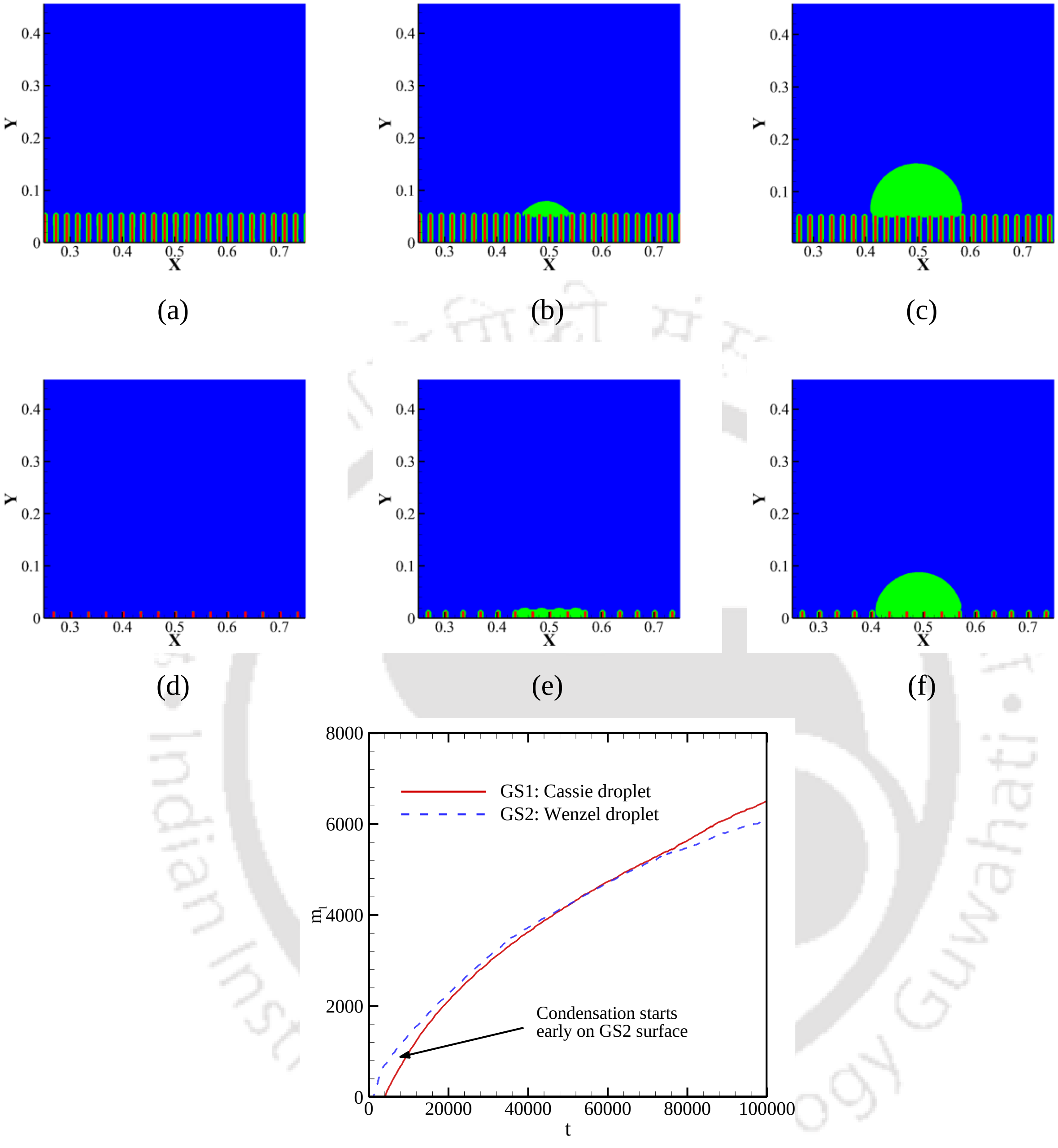

(a) (b) (c)

(d) (e) (f)

(g)

Fig. 32 Sequential temporal snapshots of the simulation domain with surface roughness GS1 $(GS1: w_s = 2, d_s = 3, h_s = 15)$ at time levels (a) $t = 0$ (b) $t = 7200$ (c) $t = 50000$; snapshots of the simulation domain with surface roughness GS2 $(GS2: w_s = 2, d_s = 6, h_s = 5)$ at time levels (d) $t = 0$ (e) $t = 1000$ (f) $t = 48000$; (g) comparison of liquid condensate accumulation rate for two rough surfaces with different roughness parameters

Fig. 32(d) plots the domain with surface roughness configuration GS2 at $t = 0$. Note that, the pillar height is much lower and the gaps between the pillars are much wider for GS2 surface. Accordingly, the vapor starts condensing at the pillar gaps on the bottom wall, which is evident from Fig. 31(e). As more and more vapor condenses into liquid, the gaps between the posts fill up and liquid nuclei merge into one big single droplet with a lower contact angle. The next figure is plotted at $t = 48000$, where a merged large droplet can be seen conforming to the structure of the surface.

The last figure [Fig. 32(g)] demonstrates the comparative mass condensation rate of both GS1 and GS2 surfaces. According to relevant literatures[129,130], due to the difference in surface energy, liquid accumulation starts early on the surface with a lower contact angle. Accordingly, a Wenzel droplet starts condensing earlier than a Cassie droplet. This trend can be identified from Fig. 32(g), where it can be seen clearly that condensation has started earlier on GS2 surface in comparison to GS1 surface. As the droplets are not removed from the nucleation site due to the absence of imposition of any body force, they cover the cold spot, and their growth rate decreases eventually. As the Wenzel drop covers all the cold spot areas, no heat is directly transferred to the vapor. In comparison to that, cold spot area coverage is lower, and as a result vapor remains in contact with the rough surface directly in some places. This phenomenon is also reflected in Fig. 32(g), as it can be seen that after a certain time growth rate of cassie droplet is higher than Wenzel droplet.

5.4 Filmwise and Dropwise Condensation

Cheng et al.[82] studied the movement of a single condensate droplet on a hydrophobic surface under the action of gravitational force using LBM in 2013. As the vapor condenses on a cold spot, a single droplet grows at its nucleating spot and remains motionless until the gravitational pull overcomes the surface tension force. Once gravity wins the competition, the droplet starts moving; eventually, a thin neck forms and the droplet detaches from the nucleation site keeping a small part at the nucleation site.

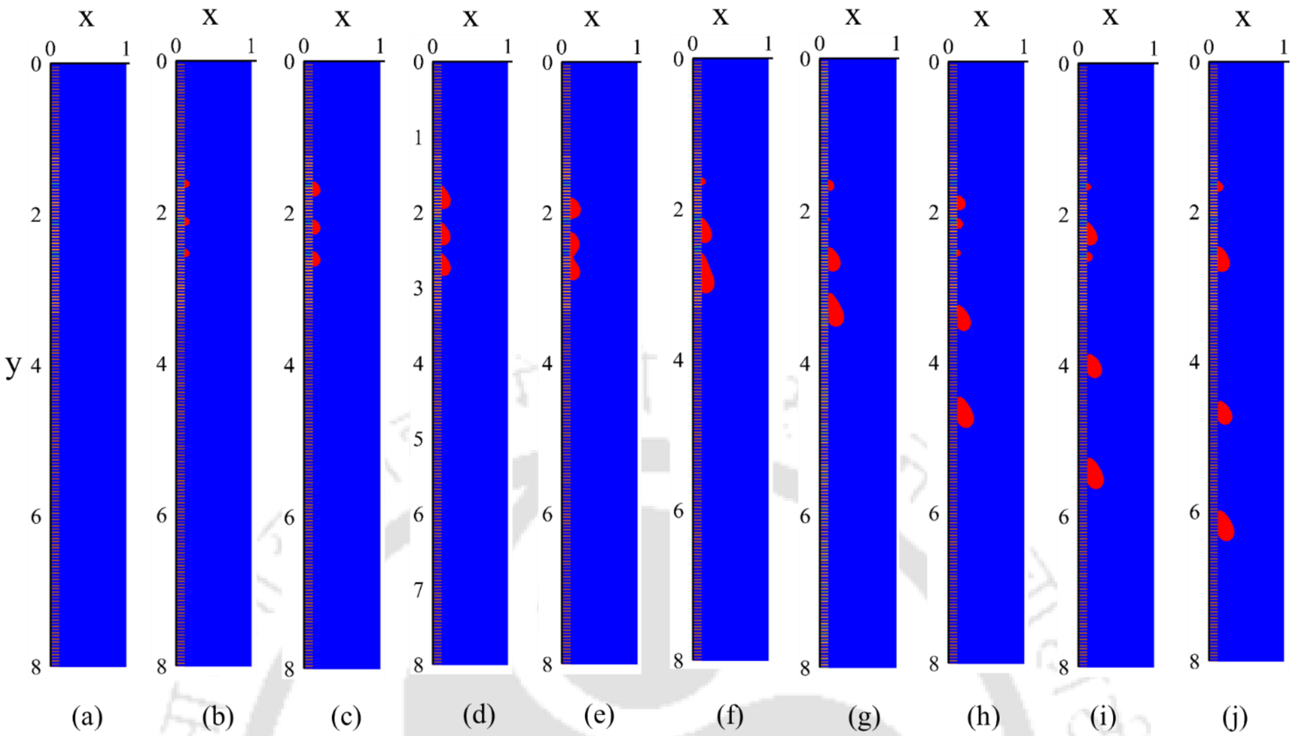

Fig. 33 Sequential snapshots for condensing droplet growth, coalescence, departure and movement in dropwise condensation mode $\left(GS1: w_s = 2, d_s = 3, h_s = 15\right)$ at different time levels (a) $t = 0$ (b) $t = 12000$ (c) $t = 24000$ (d) $t = 36000$ (e) $t = 38400$ (f) $t = 48000$ (g) $t = 62400$ (h) $t = 67200$

In reality, when vapor condenses on a cold surface, several nucleation sites are activated on the surface[129,175]. That is why, assuming one single nucleation site does not provide a wholesome picture of droplet growth, coalescence, subsequent detachment, and movement under the effect of the gravitational force. In the present work, to study the complete process, three separate cold spots are assumed as active nucleation sites on a cold wall. The blue colored part on the bottom wall in Fig. 31 represents the cold wall which is positioned at a distance of 150 lattice points from the origin and has 250 lattice points width. The temperature of the cold wall is maintained at $T_{cold,R} = 0.86$. Red patches in Fig. 31 represent the active nucleation sites with a width of 10 lu and are assumed to be maintained at temperature $T_{cold,R} = 0.8$. Other boundary conditions and the initialization process for the simulation of this problem have already been explained through Fig. 30. The size of the rectangular domain is assumed as - $L_x = 1, L_y = 15$. Two different surfaces with roughness parameter set GS1 and GS2 are used to study the dropwise and filmwise condensation process, which are depicted in Fig. 33 and 34 respectively.

Fig. 33(a) shows the vertical rectangular domain (with roughness parameter GS1) at the time $t = 0$ when the domain is completely filled with saturated vapor at $T_R = 0.9$. Fig. 33(b) shows the snapshot of the domain at $t = 12000$, where three separate small nuclei can be seen at three cold spots. It was already explained in the previous section through Fig. 32 that, when the height of texture posts is higher and the width between them is lower, condensate droplet grows into Cassie state. Accordingly, the surface with roughness parameter set GS1 produces Cassie droplets. These three nuclei can be seen to become growing droplets in Fig. 33(c), and it is also perceptible that they could not penetrate the gaps between the grooves, which indicates that they remain in Cassie state. It can also be observed from the same figure that they haven't started moving from their original spots as surface tension force still dominates over gravitational force. The next illustration [Fig. 33(d), $t = 36000$] shows that gravitational force has finally started to overcome the wettability, and the droplets have started moving downwards.

Coalescence of two drops has been a crucial research topic in the past few years. When two drops come in contact, they first form a bridge amongst them and subsequently merge into one larger drop. This same behavior can be observed in Fig. 33(e) $(t = 38400)$, which shows the start of droplet coalescence, where the front end of the second droplet merges with the rear end of the third droplet and form the liquid bridge among them. The next figure is plotted at $t = 48000$, which shows that two droplets are sliding down the rough surface, while one small droplet is growing at the top cold spot (cold spot 1). The droplet at the front is actually the combined second and third droplet, and the rear one is the first droplet. As the first one is the combination of two droplets, its size is larger than the second one.

Fig. 33(g) depicts the start of the next nucleation cycle where two growing nuclei can be seen at the top two cold spots. The bottom cold spot (cold spot 3) is still covered with the sliding droplet which is coming down from the first cold spot from the first condensation cycle. As it glides through the surface downward, this droplet sweeps away any small condensate liquid growing from the bottom nucleation site. This sweeping mechanism of the smaller droplet by comparatively larger droplet is a key process of creation of new active nucleation sites on the cold spots which enhances the heat transfer rate substantially. Subsequently drops grown from the first nucleation cycle moves away from the cold spot [Fig. 32(i), $t = 62400$] and three new growing nuclei can be observed at the spot. The droplet at the top is larger as it has been started growing earlier. Eventually, this larger droplet detaches from its nucleation spot and sweeps the other two growing droplets on its way downwards. This phenomenon can be seen in Fig 33(j), which is plotted at temporal instant $t = 67200$. This condensate liquid droplet growth, detachment, coalescence, sliding off, and sweeping continue to happen with time and DWC prevails through the whole process.

If the spacing between the micropillars is higher and height is lower, condensate droplet grows into Wenzel state. At the time of coalescence, the merged larger droplets conform to the structured surface to generate a liquid film. This phenomenon is evident in Fig. 34(a)-(f), where sequential temporal snapshots are plotted for condensation on a surface with roughness configuration GS2.

Fig. 34(a) shows the initial state of the domain where the physical domain is occupied with saturated vapor and cooling process has not been started yet. The next figure, plotted at $t = 12000$, displays that three Wenzel type droplets have grown from three nucleation sites, and bent downwards due to the effect of gravitational force. Eventually, all these three droplets start moving downwards and merge to form a liquid film which takes the shape of the rough structure. This phenomenon can be observed from Fig. 34 (c)-(e), which shows the downwards droplet movement subsequent droplet merge into a liquid film. The last snapshot is plotted at $t = 60000$ which shows the vertically downward movement of the condensate liquid film as well as more amount of condensation of vapor into liquid. Due to the liquid-cold surface contact, vapor phase and active nucleation site contact have been broken. As a consequence, heat can’t be transferred from vapor to the surface, as it goes through the liquid film at first. This situation will prevail through the whole condensation process, and it is the principal drawback of FWC, which is primarily responsible for less condensate liquid mass accumulation and heat transfer rate.

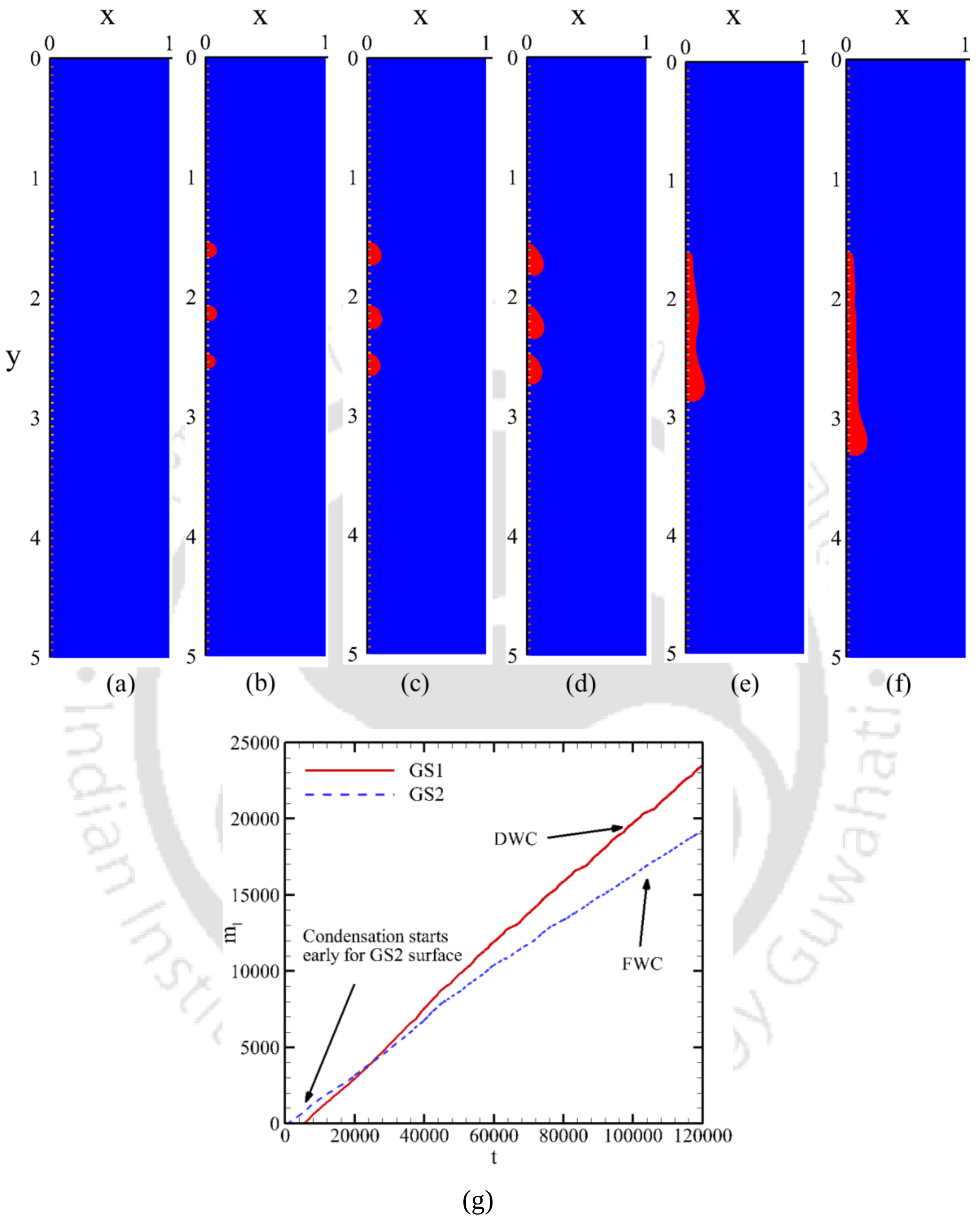

Fig. 34 Sequential snapshots for condensing droplets, growth, coalescence and resulting condensation film movement $\left(GS2 : w_s = 2, d_s = 6, h_s = 5\right)$ at different time levels (a) $t = 0$ (b) $t = 12000$ (c) $t = 24000$ (d) $t = 36000$ (e) $t = 48000$ (f) $t = 60000$; (g) comparison of liquid condensate accumulation rate for dropwise and filmwise condensation for two rough surfaces with different roughness parameters

To facilitate the condensate mass accumulation rate of both condensation cases, the total condensate liquid mass accumulation rate (m_l) for the two separate surfaces are plotted against time in Fig. 34(g). Due to the difference in surface energy, liquid accumulation starts early on a surface with a lower contact angle. Accordingly, a Wenzel droplet starts condensing earlier than a Cassie droplet. This trend can be identified from Fig. 33(f), where it is seen that condensation has started earlier on GS2 surface in comparison to GS1 surface. Despite the early start of condensation, gradually the mass accumulation rate of GS1 surface becomes higher, and the corresponding line on the graph crosses the mass accumulation line of GS2 surface. Figs. 33 and 34 illustrate that droplets will grow, detach and move away from the nucleation site to maintain the vapor-cold spot contact throughout the whole condensation process, while the film will cover cold spots for the entire condensation process. So the growth rate will always be higher for DWC than FWC. This feature is also prominent in the figure under current focus which shows a steeper slope of the GS1 accumulation line than the GS2 line. In the present work, the simulations have been done upto time level $t = 120000$. Within this time the total condensate mass (m_l) has become higher for DWC, and the graph indicates that as long as the process will continue the difference of mass accumulation rate between DWC and FWC will increase due to variation in their slope.

5.5 Surface Heat Transfer Rate

To illustrate the heat transferred through the surface as it comes in contact with vapor or liquid periodically, the surface heat transfer rate $\left(q = -k \int_{-L_c}^{L_c} \left. \frac{\partial T}{\partial y} \right|_{y=0} dx \right)$ is plotted against time for the three cold spots for both surfaces. Fig. 35 (a) represents the heat transfer through surface GS1, where the initial part (around $t = 36000$) is almost the same for all the three cold spots. It is already shown through Fig. 33(d) that upto this time, droplets have not started merging, and their growth and movement patterns are almost the same with one another. Afterward, the droplets at cold spot 2 and 3 start merging [see Fig.33(e)]. It is a very well-known fact that the conductivity of liquid is much higher than vapor. As a result, heat transfer through the surface is higher when the surface comes in contact with the liquid instead of vapor. For DWC, the periodic droplet formation and removal mechanism enable the surface to come in contact with liquid and vapor periodically. That is why periodic crests and troughs are visible for all the three cold spots in Fig. 35 (a). At first, the droplet from cold spot 2 moves to cold spot 3 to merge, and due to this reason cold spot 3 achieves its heat transfer peak first. Later, the droplet from cold spot 1 moves to cold spot 2 to give it the heat transfer peak. In this way, all these spots have their peaks and bottoms of the heat transfer rate, which is the most prominent feature of DWC. Fig. 35(b) plots the heat transfer rate for the cold spots on the GS2 surface. This surface promotes FWC, and as a result, the heat transfer rates through the three cold spots become constant after they achieve their peak at the time of coalescence.

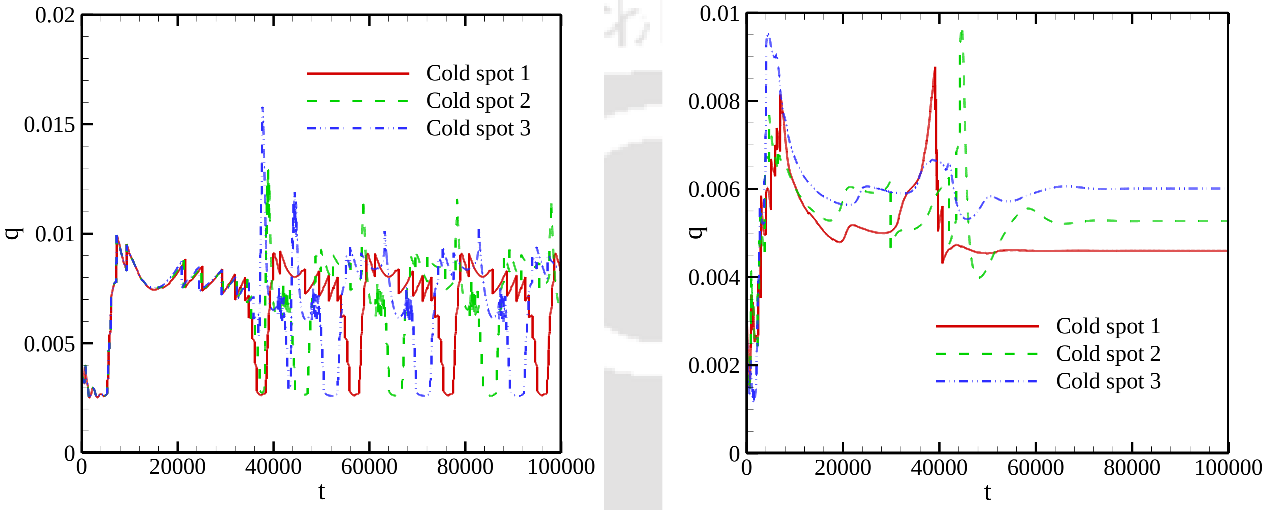

(a) (b)

Fig. 35 Surface heat transfer rate with time for all three cold spots for (a) dropwise condensation case (b) filmwise condensation case

5.6 Condensate Droplet Movement on an Inclined Plane

The condenser surface does not remain precisely vertical in many practical cases. To study the condensation process and corresponding mass accumulation and heat transfer rate, six different surface inclinations $\left(\theta = 15^0, 30^0, 45^0, 60^0, 75^0, 90^0\right)$ are considered in this section for simulation for both GS1 and GS2 surfaces. Fig. 35 shows the snapshots of condensation on GS1 surface with inclination $\theta = 15^0$. It is described in the previous sections that the GS1 surface promotes Cassie droplet formation which ultimately leads to dropwise condensation on a vertical surface. The domain is initially filled with saturated vapor only. Fig. 36(a) shows that at $t = 12000$, three separate droplets have been nucleated on the three cold spots. For an inclined surface, the gravitational pull decreases with decreasing the inclination angle(θ). If the condensing surface is inclined at $\theta = 15^0$, the condensate liquid will experience a much lower amount of gravitational force and droplets will move much slower. As a consequence, the coalescence and movement mechanism of the droplet will be changed drastically, which is reflected in Fig. 36(b)-(d). Fig. 36(b) is plotted at $t = 36000$ which depicts the growth of the three droplets. Due to the low amount of body force, the large droplets have still not started moving from their original position. Eventually, at $t = 48000$ the droplets start moving from their corresponding nucleation sites. As they grow in their respective places continuously with very slow movement they come close to one another and merge into one large droplet.

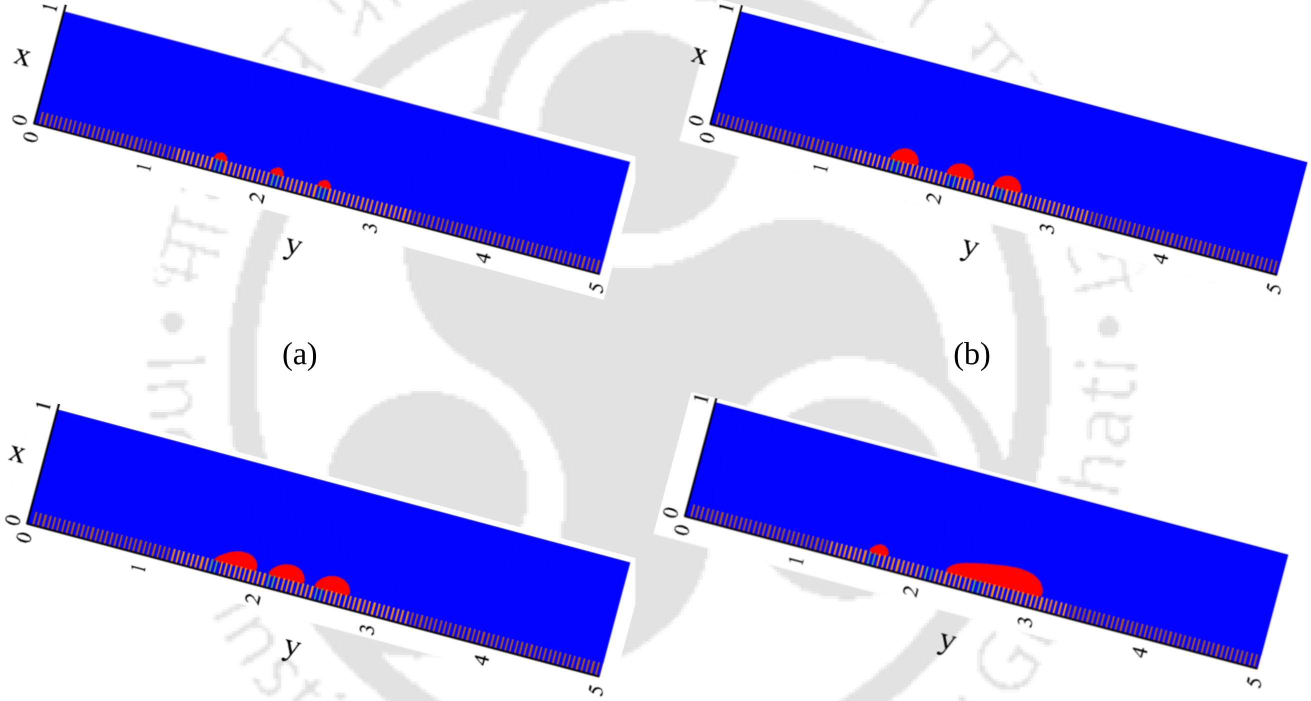

(a) (b)

(c) (d)

Fig. 36 Sequential snapshots for condensing droplets, growth, coalescence and resulting condensation film movement on an inclined surface $\left(\theta = 15^0\right)$ $(GS1: w_s = 2, d_s = 3, h_s = 15)$ at different time levels (a) $t = 12000$ (b) $t = 36000$ (c) $t = 48000$ (d) $t = 67200$

Fig. 36(d) is plotted at $t = 67200$ which shows one large droplet sliding away from the cold spots, while one new droplet has started condensing on the cold spot 1. The large moving droplet is actually formed from the coalescence of three droplets grown from three separate cold spots from the first condensation cycle. Note that, though gravitational force is low, DWC prevails throughout the simulation due to the surface roughness topology. The whole condensation cycle is already illustrated in Fig. 33. For this problem, the same process will be followed over the entire condensation process. As the droplets will move away from the cold spots, new sites will be activated where nucleation of new droplets will start. Eventually, those droplets will grow, merge, coalesce and slide away from the cold wall to initiate another condensation cycle.

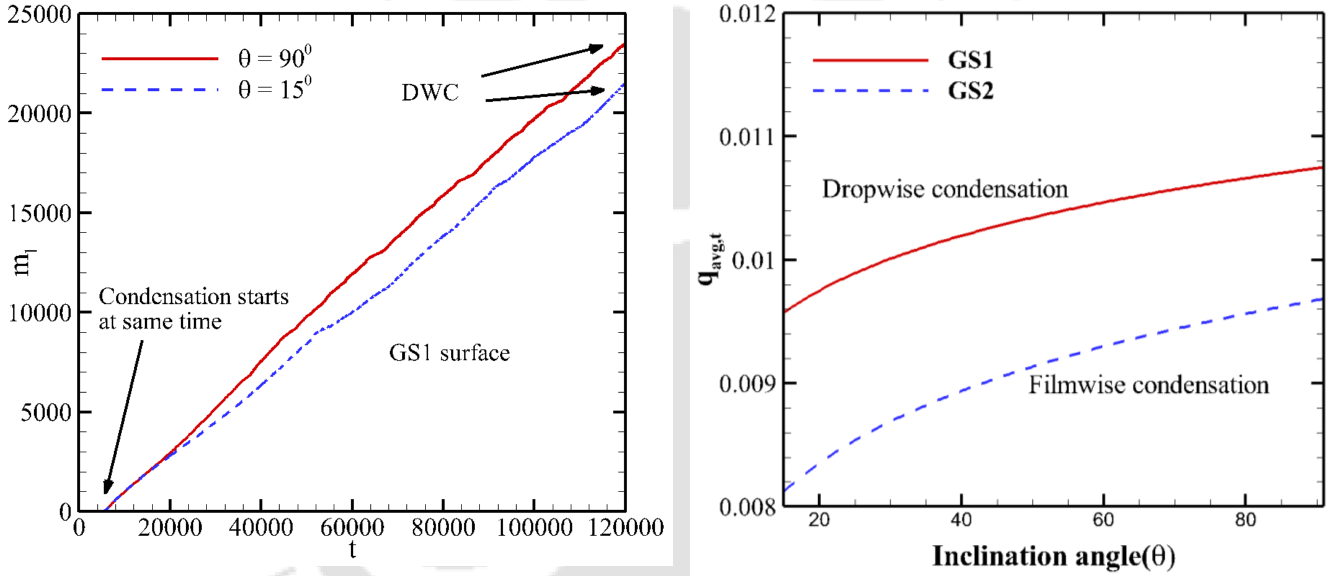

(a) (b)

Fig. 37 (a) Comparison of liquid condensate accumulation rate for two rough surfaces with same roughness parameters but different inclination angles $\left(\theta = 15^0, 90^0\right)$ (b) Time averaged heat transfer rates for surfaces with different inclination angles and roughness parameters

Fig. 36(a) plots the condensate liquid mass accumulation rate for two surfaces with the same texture but different inclination $\left(\theta = 15^0, 90^0\right)$. It can be seen from this figure that nucleation has started at the exact same time for both cases as their surface wettability and roughness configuration is identical.

Afterward, the condensation rate for the inclined surface becomes lower in comparison to the vertical surface due to the slower movement of the condensate liquid, and delayed activation of nucleation sites as the gravitational force is reduced substantially.

Latent heat release $\left(q_{avg,t} = \dot{m}_l h_{fg}\right)$ is the principal contributing factor of overall heat transfer for condensation of vapor into liquid. This heat transfer rate is plotted in Fig. 36(b) for the six angles mentioned previously for two different surfaces. The increment in time-averaged heat transfer with the surface inclination can be clearly identified from the figure under present focus. Also, the higher amount of heat transfer for DWC for each inclination angle can be identified from this figure.

5.7 Summary

We have investigated the growth and subsequent movement of liquid droplets generated from saturated vapor on a cold microstructured surface. Two disparate surfaces are used having rectangular columns to mimic the roughness, whose geometrical dimensions are quite different. In a gravity-free environment, one of them (GS1 surface) produces Cassie droplet, while the other (GS2 surface) promotes Wenzel drop formation which conforms to the rough surface.

The main objective of this work is the study of droplet movement on rough surfaces under the action of gravitational force. Two surfaces (GS1 and GS2) are assumed to be in vertical orientation at first, and droplet formation, merger, and movement on those surfaces are discussed through sequential snapshots. It was observed that the surface with narrow spacing between the columns (GS1) supports Cassie droplet formation in a gravity-free environment and DWC while oriented vertically for the consideration of the gravity force. The exact opposite behavior can be observed for a rough surface with larger spacing between the pillars. The GS2 surface promotes Wenzel droplet formation in a gravity-free environment and FWC for a vertical surface. Though the mass accumulation and heat transfer rate are higher initially on GS2 surface due to lower apparent wettability of the surface, eventually prevailing FWC obstructs the direct thermal contact between cold spot and vapor, and accordingly, both mass accumulation and heat transfer rate for FWC becomes lower than DWC on GS1 surface.

To study the effect of the gravitational force, six different surface inclinations are considered. It was observed that a vertically oriented surface removed the drop faster due to a larger gravitational force. Also, the heat transfer rate is higher for a vertical surface as the liquid drops move away quickly from the cold spots creating places for new nucleation sites. Finally, it can be summarized that a surface with narrower inter-pillar spacing supports DWC and will be ideal for industrial applications requiring high heat transfer rates.

Chapter 6

Algorithmic Augmentation of LBM to Simulate Pool Boiling

6.1 Introduction

The inability of the SC-SRT-LBM method in simulating high-density ratio thermal multiphase problems has already explained in chapter 1. The objective of the present work is to devise an improved SC-LBM algorithm capable of simulating pool boiling scenarios involving higher density ratios. The algorithm proposed to achieve higher density ratio is explained in chapter 2 (formulation section). It is essential to test the proposed model for various simple and complex geometries. Before embarking on such case studies, an attempt is made to envisage the extent of improvements possible with the current framework by comparing its output with the same from existing ones, and the static droplet problem quoted earlier is selected accordingly.

6.2 Improvement over the Existing Model

Insufficient isotropy of the existing algorithms produces false velocity currents near the curved interface during multiphase simulations, yielding nonzero velocity magnitude even in the vicinity of a static droplet, as already demonstrated in Fig. 38(a). Here simulation is performed by initiating a droplet inside a periodic domain and continuing the numerical procedure until the completion of natural phase separation. False velocity currents are clearly visible in the figure, with an enhanced level of spuriousness close to the curved interface, gradually diminishing with increasing distance from the same. Formation of small local vortices is also evident. The magnitude of such spurious velocity steeply rises with the density ratio [Fig. 38(c)], making the solution unstable as the system moves away from the critical temperature.

To illustrate the improvement with the modified discretization scheme, we have performed simulations with both the methods, so that a direct comparison with the earlier model of Gong et al.[45] can be facilitated, and concerned observations are summarized in Fig. 38(c). Here the existing model is denoted as scheme A, whereas the updated discretization scheme [Eq. (39)] is marked as scheme B.

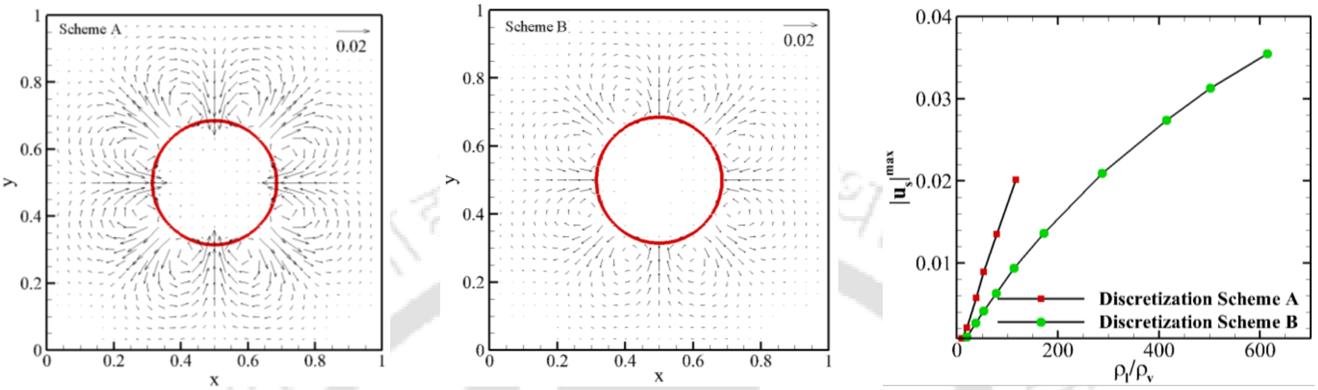

(a) (b) (c)

Fig. 38 Appearance of spurious velocity currents around a static liquid droplet being stabilized in a periodic domain at $T_R = 0.73$, following (a) discretization scheme A and (b) discretization scheme B, and (c) variation of maximum false velocity with density ratio following both schemes. Proposed scheme B offers substantial suppression in spurious velocity, while also enabling simulation at much higher-density ratios.

Adopting a computational domain similar to Fang et al.[114], and adhering to the original formulation of Gong et al.[45] (scheme A), we could achieve a maximum density ratio of only about 174, which corresponds to a reduced temperature (T_R) of 0.7 for R134a, as shown in Fig. 38(c). The maximum velocity magnitude yielded by scheme B for any given density ratio is noticeably lower than the predictions from scheme A. For example, at $T_R = 0.73$, the largest amplitude of spurious velocity with scheme A is about 113% greater than the same predicted with scheme B, despite dealing with near-identical density ratios. The same can also be substantiated by visually comparing the velocity vectors depicted in Figs. 38(a) and (b). More importantly, stable simulation with substantially higher density ratio is also feasible. Continuing with the simulation setup of Fang et al.[114] and employing the proposed SRT-LB discretization (scheme B), we have successfully computed the static droplet at a density ratio of about 600 $(T_R \approx 0.63)$ which is a considerable improvement over the existing literature ($T_R = 0.7$ in Fang et al.[114]). They were able to attain such temperature levels only with the MRT-LB framework[114], which is definitely more computation-intensive. It is also interesting to note that, despite a higher level of spuriousness beyond a density ratio of 300, the proposed algorithm is capable of sustaining the simulation, which is an apt demonstration of the enhancement in isotropy of the discretized form.

We must, however, admit that the contribution from the second nearest neighbor in the discretized force term is not consistent with the strictly local nature of the spatial discretization in classical LBM. Any multiphase LB algorithm has a bit of nonlocality ingrained in the formulation, and consideration of the second nearest neighbor appends to that. The collision operation with both momentum and thermal distribution function, though, maintains locality, and there is no requirement of explicitly evaluating pressure unlike Tanaka et al.[77] . The modified scheme B requires only about 15% more computational time compared to scheme A while simulating pool boiling, which is quite reasonable considering the improvement achieved in suppressing the spurious velocities. The increase in computational cost with the formulation of Tanaka et al.[77] was substantially greater, as per their own admission. Primary contribution towards the increased time requirement with scheme B in our paper is expectedly from the SC force calculation, as the concerned CPU time rises from about 8.82 to 19.26%. Consequently, the CPU times for the momentum and thermal collision operations descend from 15.55 and 15.74%, respectively, to 13.93 and 14.11%, despite no significant change in their values. One possible penalty may, however, have to be incurred with the current scheme in terms of the enhanced complexity in parallelization owing to the nonlocality. One of the most alluring features of LBM is easy amenability to parallelization, and the intrusion of nonlocality in any multiphase LB algorithm can affect that, the SC force itself being nonlocal in nature, which can be more sizable with the inclusion of the additional layer of nodes in SC force calculation

6.3 Numerical Validation

The pseudopotential-based LB multiphase model does not require any specific interface-tracking algorithm, which is one of its most notable advantages. It allows natural separation of phases based on the density differential and hence it is logical to employ the traditional Laplace test for an indirect validation, which demands a precise interface conceptualization. Consequently, simulations are performed to stabilize a static liquid droplet in a vapor domain in the absence of any body force for three different reduced temperatures. Resultant variations in pressure differential across the interface $(\delta p = p_{in} - p_{out})$ are plotted with respect to the inverse of droplet radius in Fig. 39(a). A clear linear relationship is conspicuous, which is sufficient testimony towards successful diagnosis of surface tension at the interface.

As discussed earlier, another important facet to secure during any multiphase simulation is the compliance of simulated phasic densities with the analytical value obtained from the Maxwell area construction rule[4,5] This is a critical constraint towards thermodynamic consistency of any multiphase LB model. Accordingly, the static droplet problem is revisited over a range of reduced temperatures with both the discretization schemes, referred to earlier as scheme A and B. As presented in Fig. 39(b), both yield satisfactory reproduction of the analytical value of the saturated liquid density. There is, however, deviation on the vapor side, with scheme A noticeably veering away from the theoretical curve. The proposed scheme B is able to extend the simulation to significantly lower saturation temperature and hence much lower-density ratio, albeit at the expense of degraded accuracy for $T_R < 0.66$.

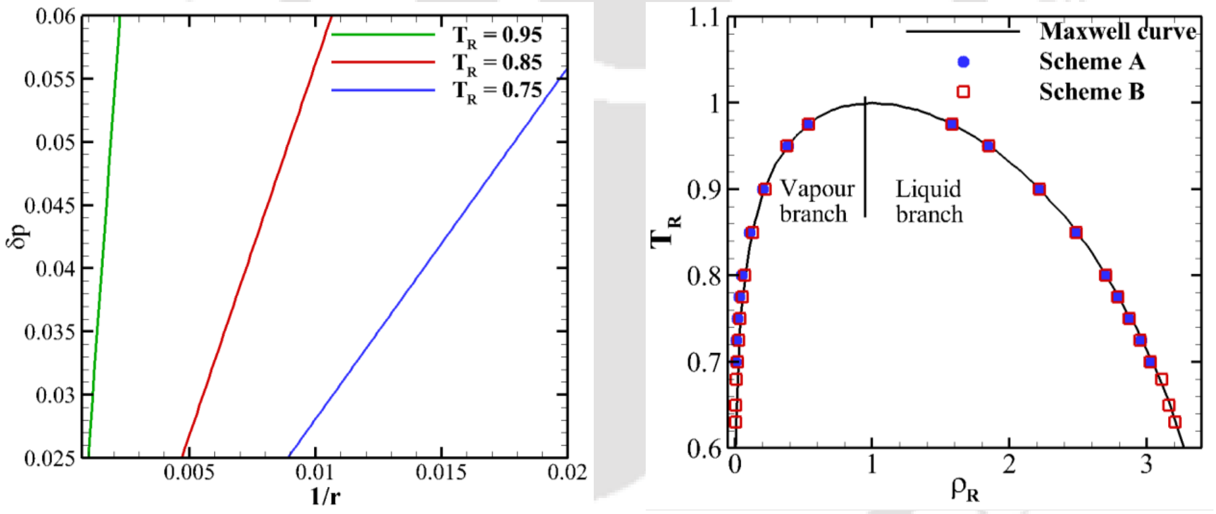

(a) (b)

Fig. 39 Qualitative validation of the proposed algorithm: (a) The pressure differential across the interface of a static droplet exhibits a linear relationship with the reciprocal of droplet radii for three different saturation temperatures; (b) liquid and vapor coexisting densities predicted with scheme B referred to earlier demonstrate excellent conformity with the Maxwell area construction rule[4,5] at significantly lower reduced temperatures

6.4 Problem Definition

Four different geometric configurations are selected to envisage the bubble dynamics and heat transport characteristics during pool boiling with the proposed algorithm, gradually advancing from simple to complicated domains. Corresponding schematic representations are available in Fig. 40, and the associated initial and boundary conditions are delineated below.

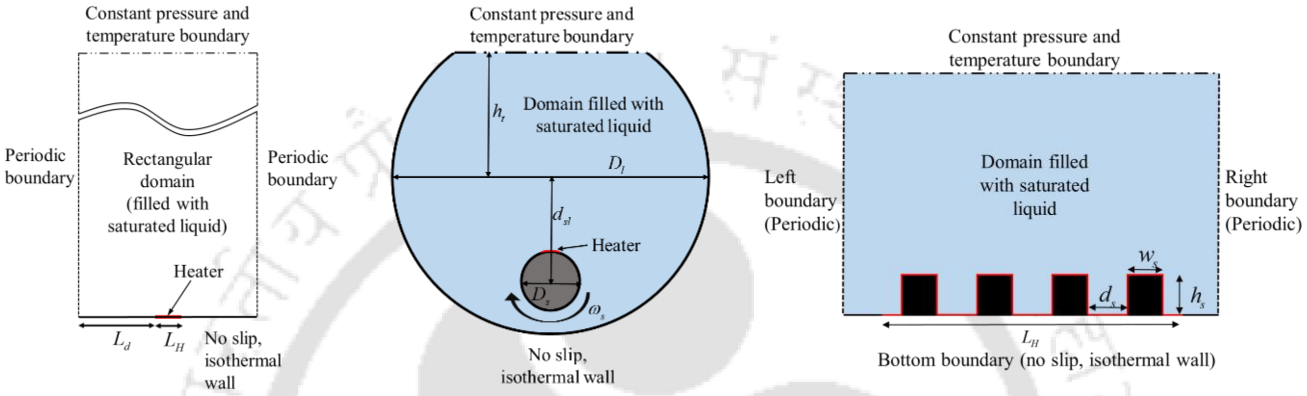

(a) (b) (c)

Fig 40. Schematics of the geometric configurations considered for the present paper: (a) an open rectangular domain with micro or distributed heater at the bottom surface; (b) an open fluid-filled cylinder housing a noncoaxial rotating solid cylinder, which embeds a microheater at the top surface; and (c) a structured heater composed of four identical columns mounted along the bottom surface of an open rectangular domain.

The first test case concerns nucleate pool boiling in a rectangular domain [Fig. 40(a)], composed of 150 × 600 lattices.The domain is initially filled with saturated liquid maintained at $T_R = 0.75$. The synthetic refrigerant R134a is selected as the working fluid and the relevant thermophysical properties are initialized with the corresponding saturated liquid properties. PR-EOS predicts a corresponding lattice-level liquid density value of 7.68 and vapor density of 0.099, which conforms to a density ratio of about 77.6. It is considerably higher than comparable literature, where hardly any study exits for $T_R \leq 0.85$. As mentioned earlier, the surface wettability force is realized in Eq. (36a) by tuning the false wall density at the solid node neighboring to the solid-fluid interface. Unless stated otherwise, we adhere to a fixed magnitude of $\rho_w = 4.0$, which concedes a contact angle of 56.97^0. The vertical boundaries are periodic in nature, while the top boundary is identified as a free surface, characterized by saturation temperature and pressure, i.e., $T_R = 0.75$ for the present configuration. The bottom surface houses a microheater, portrayed by an isothermal section of five lattice unit (L_H) length with elevated temperature. The unheated part of the bottom surface is maintained at the initial temperature. All the reported computations are performed with $\beta = 1.185$ and $g = 5\times10^{-5}$ unless mentioned otherwise. Magnitudes of the relaxation times are obviously dependent on the prevailing fluid properties. For $T_R = 0.75$, the relaxation parameters for momentum conservation (τ_f) for liquid and vapor phases are found to be 0.75 and 1.33, respectively, while the same in relation to energy conservation (τ_g) are 0.57 and 1.47, respectively.

The second problem adopts a curvilinear geometry in the shape of a cylindrical fluid-filled container with an open face at the top, as shown in Fig. 40(b). It includes a smaller solid cylinder, with the centers of both the cylinders having a vertical offset (d_{sl}) of 100 lattice units. The diameters of the larger (D_l) and smaller (D_s) cylinders are 300 and 40 lattice units, respectively. The inner one rotates with a constant angular velocity of $\omega_s = 7.5\times10^{-3}$, while the other remains stationary. A microheater stretching across seven lattice units is mounted on the surface of the smaller cylinder, the surface of which is subjected to a certain controlled amount of superheat. The wall of the outer cylinder is isothermal, while the top opening is contemplated as a free surface.

The geometry of the third problem resembles the first one, with the primary difference being the incorporation of a wider heater. A plain heater of 400 lattice unit width is symmetrically emplaced on the bottom boundary of the computational domain measuring 600 × 800 lattice units. This configuration is modified in the fourth problem to inlay a structured heater, embodied by four identical solid columns [Fig. 40(c)]. The horizontal expanse of the heater, as well as the domain dimensions, remain unchanged. We have selected the width and height of the columns, as well as the intercolumn distance, to be the same, with $w_s = h_s = d_s = 40$ lattice units. The selected sections along the bottom wall, as well as the surface of all the columns, constitute the heater and are maintained at the elevated temperature to instigate bubble nucleation. The initial and thermal boundary conditions stand similar to the first configuration in all the others.

It is pertinent to acknowledge that the grid structures embraced for each of the geometric configurations have been identified through a systematic mesh-convergence study, which can be detailed here with the first one as an example. We consider three different mesh structures, namely, 120 × 480, 150 × 600, and 180 × 720. Initially, the rectangular domain is assumed to be filled with saturated liquid at $T_R = 0.9$, and a microheater having a width of five lattice units is placed centered at the bottom wall with $\Delta T_{\text{sup}} = 0.4$. Lattice-level magnitude of the gravitational acceleration is adjusted according to the imposed length scale, which varies with the adopted mesh structure. All the three nodal arrangements yield near-identical profiles of fluid density along the vertical centerline, which can be visualized to reveal the thickness of the diffused interface, with density changing from vaporlike to the liquidlike level as we move upward. That establishes the mesh-independent nature of the reported results, and, accordingly, we have converged on 150 × 600 to perform all the subsequent simulations. A similar procedure has been followed for the other three configurations as well.

6.5 Rectangular Domain with a Microheater

The modified discretization scheme is employed first to explore the bubble dynamics during nucleation from a microheater submerged in an initially isothermal liquid pool [Fig. 41(a)]. Conventional multiphase algorithms cannot spontaneously instigate the process of heterogeneous nucleation and subsequent dynamics, owing to their ineptitude in destabilizing the phase equilibrium, and popularly require a microbubble at the simulated nucleation site, in complete contrast to real experiments. One of the distinct merits of phase-change LB models is the nonrequirement of any artificial vapor injection or assumed nucleus. In the present algorithm, the liquid-vapor coexistence density is controlled by the adopted non-ideal-gas equation of state (PR-EOS) embedded into the modified pressure tensor. On addition of a sufficient amount of energy ($\geq$ enthalpy of vaporization) to the superheated liquid, PR-EOS estimates the nodal density to be equal to or less than saturated vapor density, allowing direct categorization of phases. This particular feature allows us to replicate true experimental conditions into the numerical framework, stimulating nucleation on the microheater surface on the addition of energy to the saturated liquid and ensuing bubble dynamics.

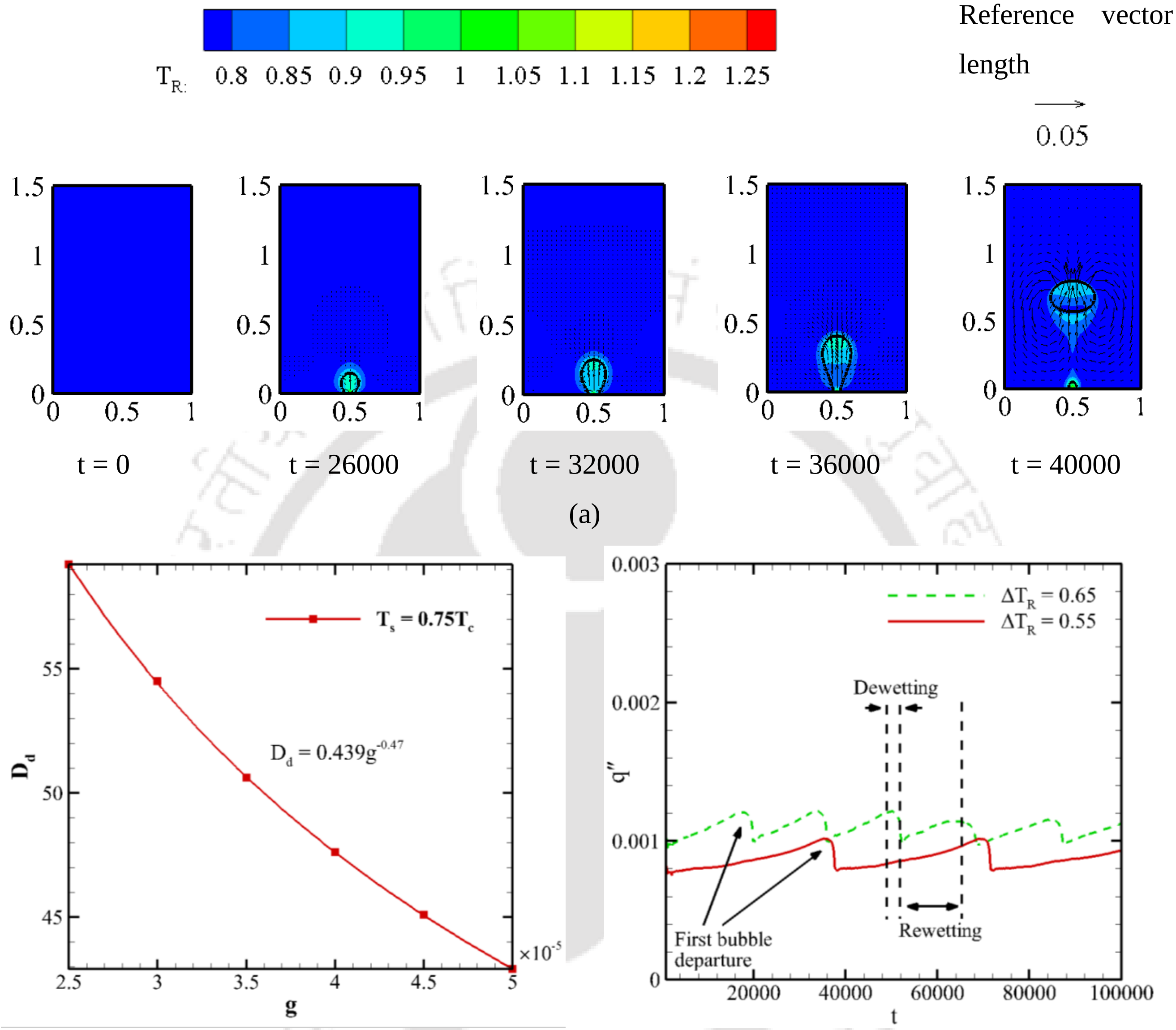

(a)

(b)

Fig. 41 Numerical characterization nucleate boiling from a microheater in an open rectangular domain: (a) snapshots of one bubble ebullition cycle presenting temperature contours, velocity vectors, and bubble contour (thick black line); (b) validation of Fritz's correlation[6] to prove that the bubble departure diameter is inversely proportional to g; and (c) temporal variation in wall heat flux for two different wall superheat values, demonstrating periodic dewetting and rewetting of the heated surface.

A series of snapshots is presented in Fig. 41(a) to demonstrate the ebullition cycle during pool boiling with the microheater, when the heater surface is subjected to a wall superheat of $\Delta T_{\sup} = 0.55$. The first picture in Fig. 40(a) depicts the initial status of the domain, where it is filled with quiescent liquid at saturation temperature. Continuous energy addition gradually induces natural convective motion in the domain, along with the development of a superheated liquid layer on the heater surface. A minuscule bubble appears slightly before $t = 26000$, marking that as the instant of the first nucleation. As the energy injection is continued, the bubble grows in size, increasing the contact area. A significantly larger bubble is visible at $t = 32000$. The expansion of the interface also forces the liquid away from the heated surface, inducing some liquid motion, as is evident from the small velocity vectors appearing around the bubble. Being proportional to the bubble volume, the buoyancy force rapidly enhances with such bulging and attempts to tear the bubble away from the surface, confronting the surface tension force, which is reciprocal to the length of the contact line. The size of the bubble at the instant of departure is decided by the interplay of these two forces. The snapshot corresponding to $t = 40000$ displays the domain immediately after the departure of the first bubble, where a small vapor embryo is left behind, which can expedite the appearance of the next one. The void left by the departure creates a low pressure zone, and surrounding liquid rushes in to fill that up, as demonstrated by noticeably large velocity vectors. It is, therefore, very much evident that the present algorithm is able to emulate the entire ebullition cycle for the selected configuration.

A correlation was proposed by Fritz[6] to identify an analytical expression for bubble departure diameter from a balance between surface tension and buoyancy, which is of the following form - $D_d = 0.0208\sqrt{\frac{\sigma}{g\left(\rho_l - \rho_v\right)}} = 0.0208 l_0$. Variation in thermophysical properties can be neglected within such a pool because of inconsequential change in the hydrostatic head. Consequently, the departure diameter can be viewed to be inversely proportional to the gravitational acceleration $\left(D_d \propto g^{-0.5}\right)$, which is a widely used medium for code validation within the LB community[80,112,114]. Concerned predictions from our paper are available in Fig. 41(b) for $T_R = 0.75$, demonstrating a very reasonable prediction with an exponent of 0.47, which can be considered to be an indirect validation for the present algorithm. A comparison is also drawn here with scheme A, which predicts an exponent value of 0.45 with identical sets of operating conditions, thereby substantiating the superiority of scheme B over itself.

The temporal variation in heat flux at the nucleation site for two different wall superheat values are presented in Fig. 41(c). A periodic pattern is quite evident, with the heat flux attaining the peak at the moment of bubble departure. The residual embryo promptly starts expanding on the surface, pushing the liquid away from it. Thermal conductivity of vapor being significantly lower than liquid, a drastic plunge in heat flux results, and this phenomenon is referred to as dewetting. Once the vapor grows reasonably in size, the necking process is initiated, with swift decrease in the vapor-solid contact area and liquid rushing in to fill the void. Heat flux noticeably increases during such rewetting, reaching the maxima on departure, followed by another dewetting and hence completing one ebullition cycle. A larger wall superheat imparts a greater amount of energy into the fluid domain and hence escalates the departure process by reducing the time period of ebullition. Raising the superheat from 0.55 to 0.65 nearly doubles the frequency, with substantial rise (≈19%) in the peak heat flux as well.

6.6 Cylindrical Domain with Microheater

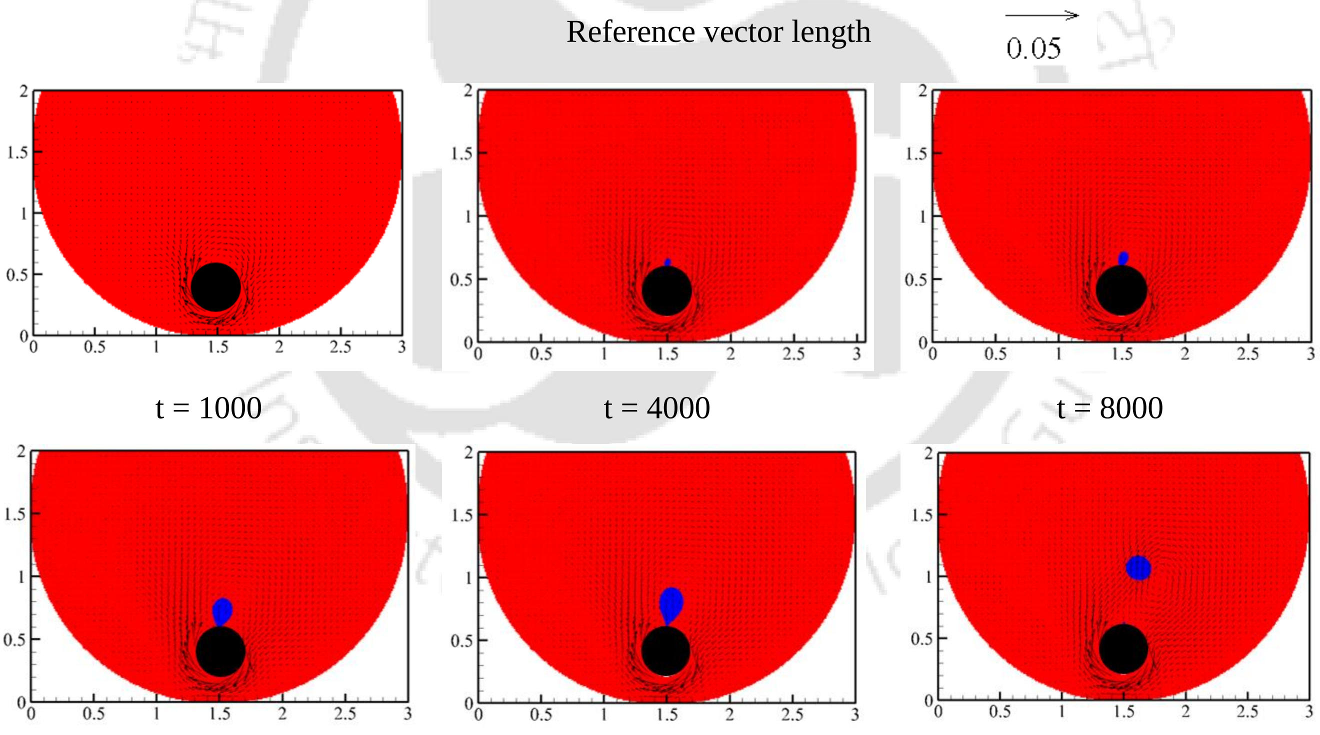

t = 1000 t = 4000 t = 8000

t = 14000 t = 19000 t = 22000

Fig. 42 Snapshots of one bubble ebullition cycle from a microheater in an open cylindrical domain presenting velocity vectors and phase contour; here red and blue colors, respectively, symbolize liquid and vapor phases.

Our next focus is on analyzing the nucleation characteristics in a non-grid-aligned geometry and consequently the fluid domain bounded by two non-co-axial cylinders is selected, the schematic of which is available in Fig. 40(b). Here the inner cylinder is assumed to be rotating in clockwise direction, imposing motion to the initially stagnant fluid. A wall superheat $\left(\Delta T_{\text{sup}}\right)$ of 0.55 is imposed on the microheater surface and prospective developments in the flow domain are presented through a series of snapshots in Fig. 42. The first instant corresponds to $t=1000$, where no vapor nucleus is present, while the fluid adjacent to the smaller cylinder follows its motion. Such forced flow, however, remains restricted only within a narrow zone around the inner cylinder, with the bulk exhibiting negligible velocity. The first instance of nucleation appears at $t=4000$, as a small vapor nucleus is visible on the heater surface. Because of the inflicted motion of the neighboring fluid layer, the bubble is pushed in the clockwise direction, emanating asymmetry to the liquid-vapor interface, with the vertical axis increasingly tilting right with time. Subsequent growth of the vapor nucleus is depicted in the next three snapshots, along with gradual rightward inclination. With rise in bubble size, buoyancy and liquid inertia progressively become stronger in comparison to surface tension, and the necking process is initiated. A very thin neck can be seen around $t=19000$, signifying that the bubble is about to depart. The bubble rises quickly postdeparture, driven by buoyancy, and also gets pushed further right by the moving liquid $(t=22000)$. A small vapor embryo can be on the heater surface, which leads to the next nucleation, an observation similar to the rectangular domain. The present algorithm can, therefore, claim to have successfully reproduced the ebullition cycle even in cylindrical configuration, despite a staircase representation of the curved surface.

6.7 Boiling Regimes with a Distributed Heater

With the presence of multiple nucleation sites in the form of a distributed heater, it is possible to identify two distinct regimes of pool boiling[6,81], namely, nucleate and film boiling, separated by a span of transition. Nucleate boiling is characterized by periodic growth of isolated bubbles in distinct nucleation sites at low wall superheat. With rise in wall temperature, such bubbles can merge in the vertical direction, resembling a columnar structure. That causes a sharp ascent in surface heat flux during temperature-controlled experiment and also hinders the movement of liquid rushing in to fill the void, helping the nucleating bubble to grow larger.

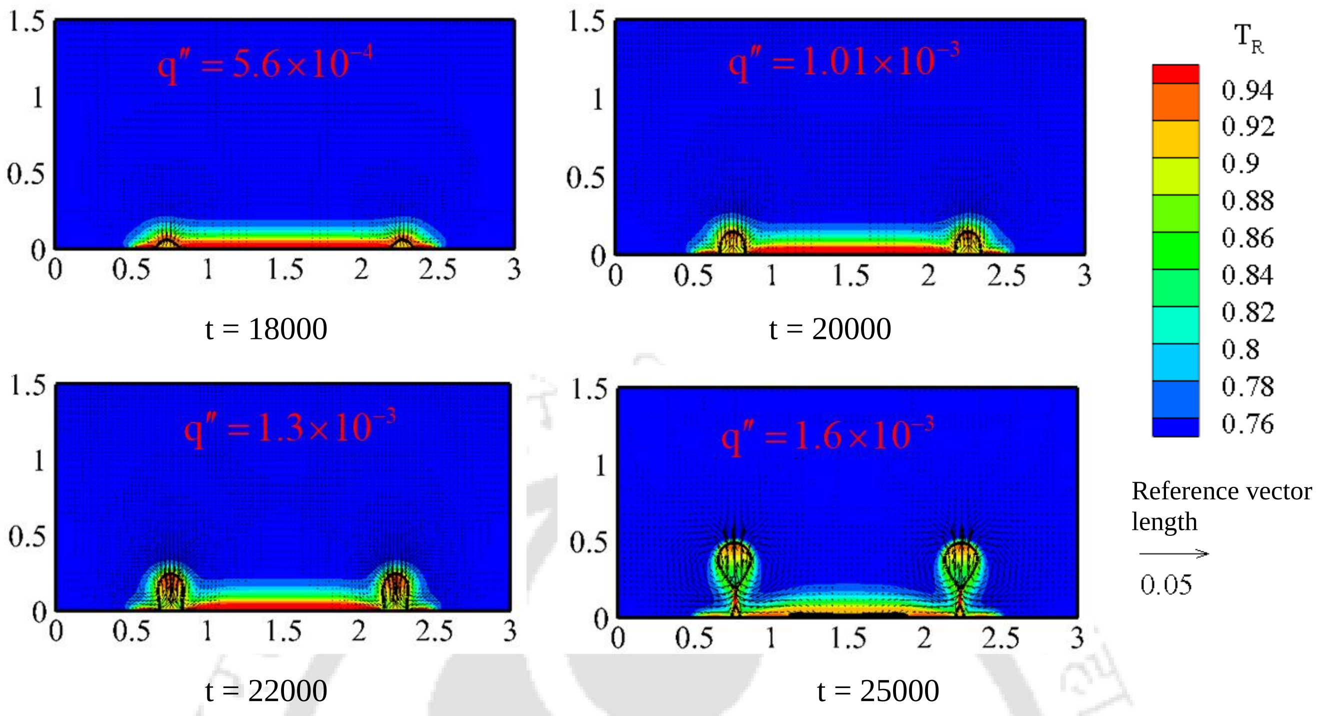

(a)

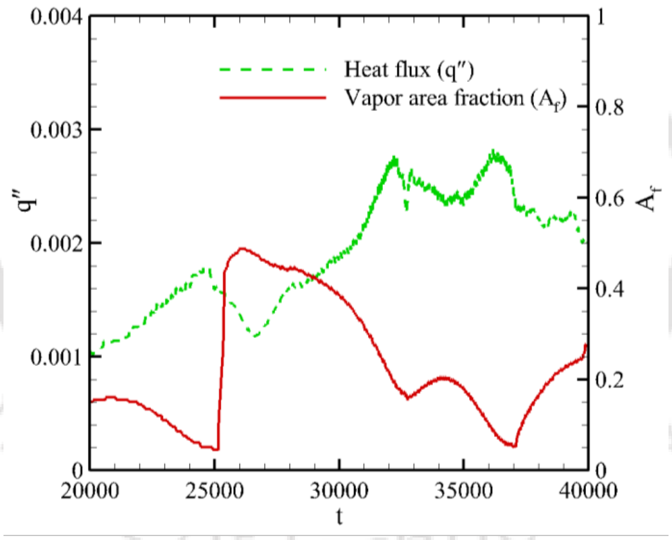

(b)

Fig. 43 Characterization of nucleate boiling from a distributed plain heater in an open rectangular domain with $\Delta T_{\text{sup}} = 0.21$; (a) snapshots of bubble nucleation and growth from discrete nucleation sites, where existence of the superheated liquid layer and bubble-induced liquid motion can clearly be seen, and (b) temporal variations in wall heat flux and vapor area fraction, showing considerable rise in heat transmission following departure of a bubble.

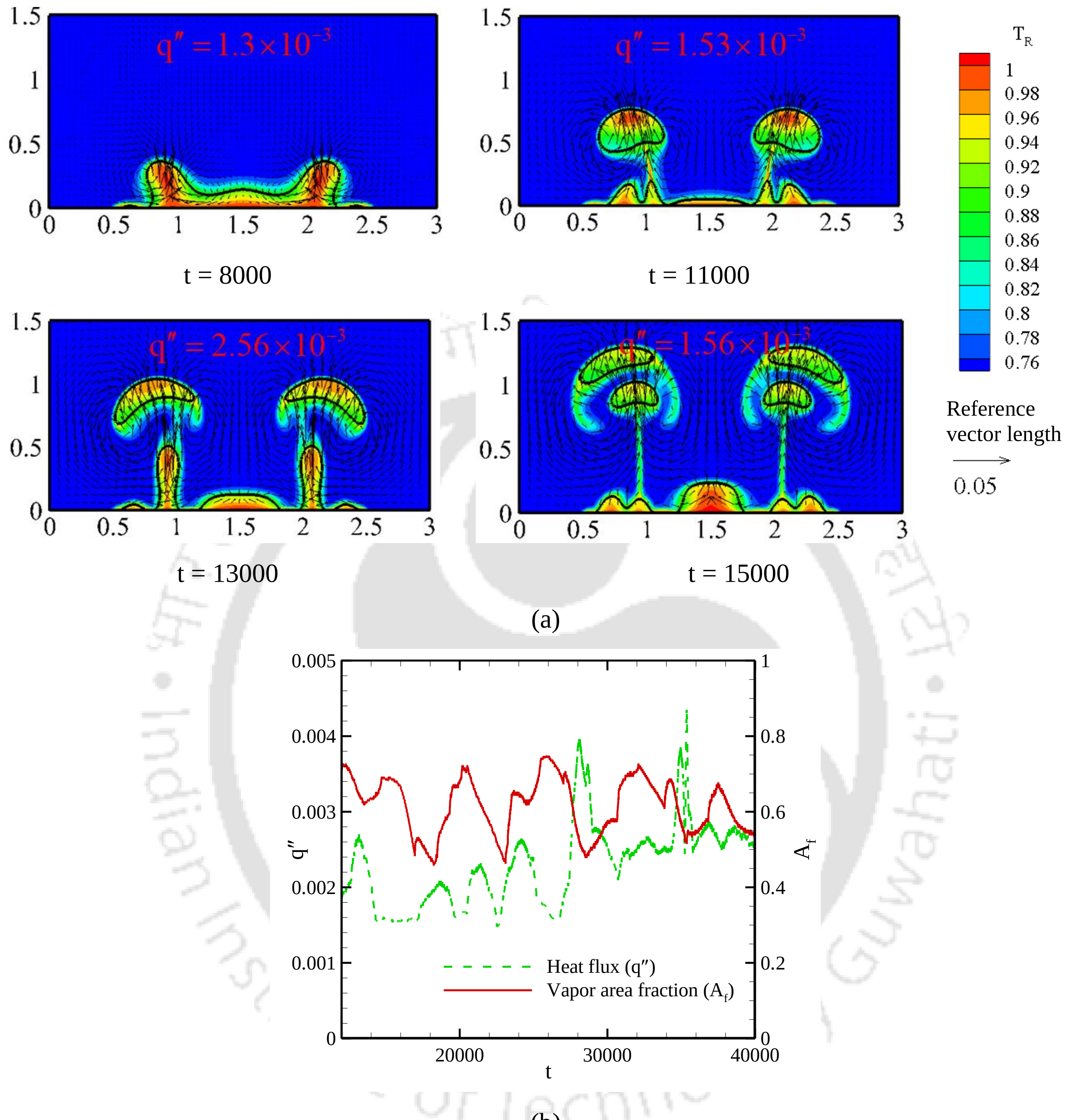

(a)

(b)

Fig. 44 Characterization of transition boiling from a distributed plain heater in an open rectangular domain with $\Delta T_{\text{sup}} = 0.27$; (a) snapshots of bubble nucleation from an unstable vapor film, the expanse of which keeps on changing with time and the superheated liquid layer of which is also unstable, and (b) temporal variations in wall heat flux and vapor area fraction, signifying the quite chaotic nature of the phenomenon.

The number of active nucleation sites also increases with the wall superheat, the consequence of which is the merging of bubbles along the surface and subsequent development of a vapor film. Stable film boiling is feasible only at substantially high wall superheat, where radiation is a major contributor towards overall heat transfer and poor conductivity of vapor limits the conduction counterpart. The transition regime is symbolized by wavering between bubble nucleation and unstable film formation in a nonregular manner, showing glimpses of both the regimes. While a conventional finite-volume simulation requires the assumption of single or multiple vapor embryos to instigate the numerical procedure[176], Li et al.[81] have shown that the LB multiphase model can produce all three modes of pool boiling without any such precondition. So our next objective is to illustrate different regimes of pool boiling using the third geometric orientation the observations with three representative wall superheat values are detailed below.

Figure 43 shows the snapshots for four different time instants with a wall superheat of 0.21. The first set of nucleation appears slightly before $t = 18000$, with two sites getting activated close to either edge of the heater. While both these embryos grow into larger bubbles and necking gets initiated, the presence of the superheated liquid layer on the heater surface is quite prominent. Both the antecedent bubbles depart around $t = 25000$, leaving a respective minuscule embryo on the surface. Similar to the point heater, the departure of the vapor bubble induces substantial liquid motion, which introduces an additional inertial effect into the domain. The departed bubbles approach spherical shape while rising (not shown), which is an indicator of the dominance of the surface tension over inertial force, owing to the smaller velocity level involved here. This particular pattern of vapor nucleation, growth, and departure is repeated in a periodic sequence, with new nucleation sites getting activated over time around the heater center. Still, for the imposed wall superheat, the number of active nucleation sites remains low enough to restrict the dynamics to the isolated bubble rising mode of the nucleate boiling regime.

The local heat flux, with a specified degree of wall superheat, is reliant on the thermal conductivity of the no-slip layer in contact with the heater surface. As the composition of that layer teeters between liquid and vapor, with massive disparity among their respective thermal conductivities, instantaneous area-averaged heat flux is strongly dependent on the relative fraction of heater surface being covered by the vapor phase $\left(A_f = {A_{vapour}} \big/ {A_{heater}} \right)$, and can be defined as

$$\left(q'' = -\frac{1}{L_H} \int_{-L_H/2}^{L_H/2} k \left.\frac{\partial T_R}{\partial y}\right|_{y=0} dx \right) \tag{57}$$

Temporal variations in both these parameters are presented in Fig. 43(b), where the span is selected after the first set of nucleation and domain attaining periodicity. It must also be noted that, for a two-dimensional domain, the dimension normal to the plane of the figure can be assumed to be unity, and hence $A_{bubble} = L_H$. The visual pattern of heat flux (q'') alteration is quite similar to Fig. 41(c). The heat flux also shows an inverse relationship with the area fraction covered by vapor $\left(A_f\right)$, which is very much logical considering the ratio of liquid-to-vapor thermal conductivity $k_l / k_v = 10.1$ for the selected conditions.

A noticeable change in the domain thermal hydraulics can be observed on increasing the wall superheat to 0.27, as demonstrated in Fig. 44. A larger temperature differential at the heater surface infuses energy to the fluid domain at a faster rate, inducing earlier nucleation, despite initial conditions being the same. At $t = 8000$, the heater surface is partially covered by a thin vapor film, owing to the faster rate of vapor generation and merging of neighboring nuclei along the surface, with two prominent bubbles protruding from either end of the film. These bubbles gradually attain their respective critical volumes because of the continuous energy addition and repudiate the surface to rise upwards $(t = 13000)$. It is interesting to observe the oblate shape of these bubbles during their upsurge, which hints towards a balance between inertial and surface tension forces. Compared to the previous case, here the liquid velocity level around the upsurging bubble is noticeably greater, enhancing the inertial effects. Another set of bubbles can be observed over the next two snapshots. Periodic growth and departure of bubbles destabilize the film, which remains to be capricious and discontinuous. The fraction of heater surface shrouded by the vapor film frequently changes without following any pattern, which is the primary attribute of the transition regime of pool boiling, displaying traits of both nucleate and film boiling simultaneously. The fickle nature of the phenomenon is clearly evident following the irregular appearance of spikes and dips from Fig. 44(b). Any peak in surface heat flux corresponds to a trough in the vapor area fraction, indicating a shrink in the length of vapor film. Such erratic fluctuations are consistent with the observations from Li et al.[81], authorizing the transitory nature of the flow regime. Still the fraction of surface covered by vapor is significantly larger compared to pure nucleate boiling, which is the consequence of the formation of an unstable film.

A more stable vapor film is established with even higher wall superheats, as can be seen from Fig. 45 for $\Delta T_{\sup} = 0.31$. The film covers the entire heater surface, preventing liquid from coming in contact with the heater surface and hence any direct energy addition. The only possible way for the liquid to acquire energy is via conduction through the vapor film, which is naturally a weak process. The thin vapor film present in the first snapshot grows significantly by $t = 5000$, with the primary mode of phase conversion being evaporation at the liquid-vapor interface and subsequent diffusion of molecules across it. With an increase in thickness, the growth of two vapor bubbles can be seen around $t = 8000$, which leaves the film in the next snapshot. Gradual thickening of the film and thermal convection in liquid in the vicinity of the film introduces substantially larger velocity on the liquid side of the interface. Corresponding shearing action may be the reason behind ripping off bubbles from the interface. However, the degree of superheat not being very high, the role of viscosity cannot be ignored either. Accordingly, we are presently not in a position to categorize the vapor formation from the film as a Rayleigh-Taylor instability, originating because of the presence of a lighter phase below the heavier one, or Taylor-Helmholtz instability induced by velocity shear, which demands more focused exploration. In fact, that is not the objective of the present work as well. While the thickness of the film changes with time, it continues to be stable over the heater surface, as it is being substantiated by the magnitude of area fraction steadily hovering around 1. The heat flux also constantly persisted with a level much lower than nucleate boiling, compatible with the poor thermal conductivity of vapor.

In conventional multiphase simulations, it is customary to assume the saturation temperature to prevail interior to the bubbles, which is in contrast to the experimental knowledge. The microthermocouple measurement of Wagner and Stephan[177] revealed significant super heating inside the embryo, which was later reproduced through LB simulations[81,112]. The same has successfully been emulated in the present paper. A substantial temperature gradient exists within the vapor phase, particularly for the ones getting ripped off the film. A thin superheated liquid layer can also be seen around the growing and rising bubbles. So we can claim that the present scheme is competent in capturing both the bubble dynamics and thermofluidic pattern quite realistically

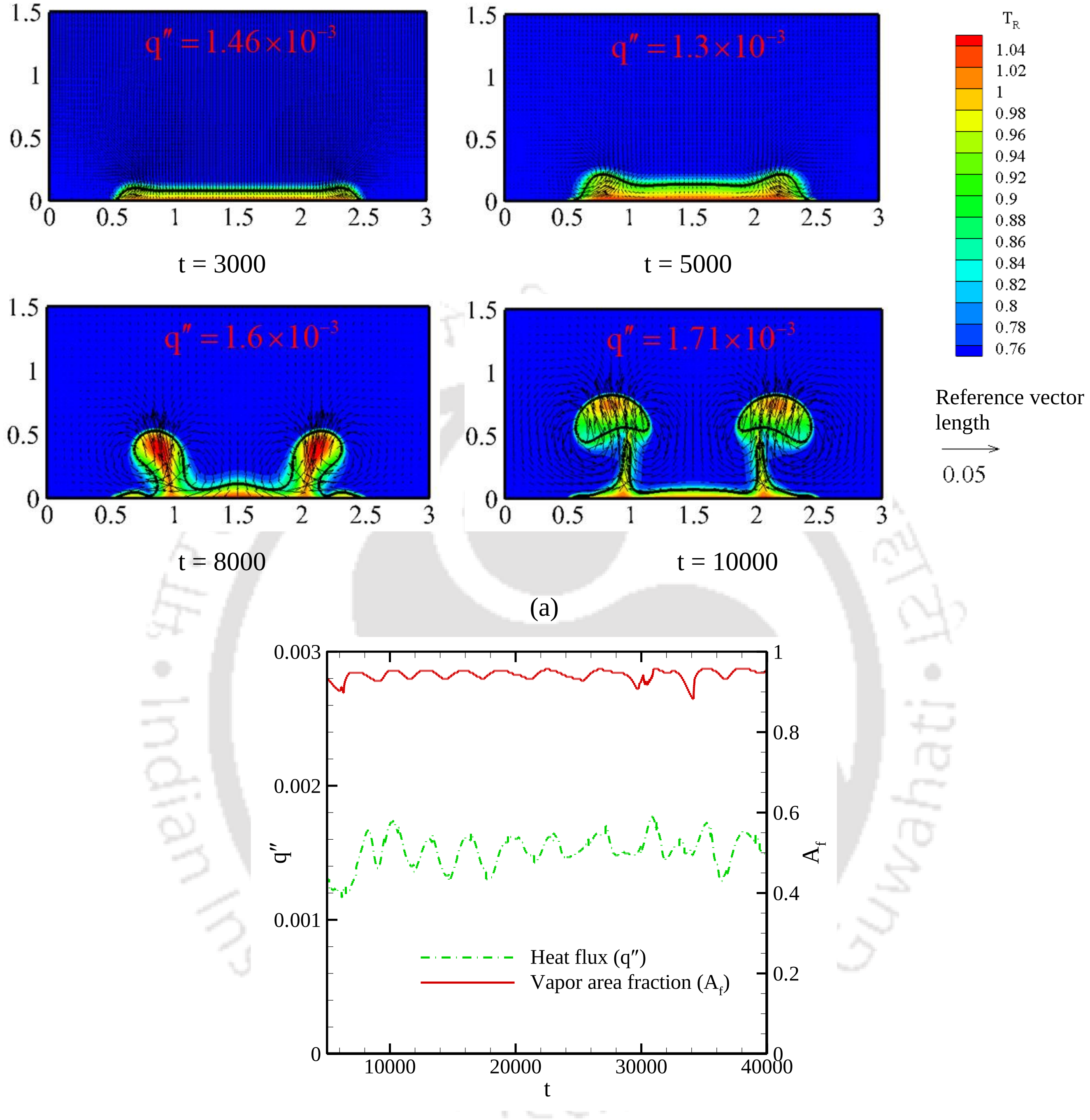

(a)

(b)

Fig. 45 Characterization of transition boiling from a distributed plain heater in an open rectangular domain with $\Delta T_{\text{sup}} = 0.27$; (a) snapshots of bubble nucleation from an unstable vapor film, the expanse of which keeps on changing with time and the superheated liquid layer of which is also unstable, and (b) temporal variations in wall heat flux and vapor area fraction, signifying the quite chaotic nature of the phenomenon.

It is pertinent to mention here that radiation can have a significant role in overall heat transfer during film boiling owing to the rise in absolute surface temperature, and absence of any such model can be recognized as a limitation of our work. However, the prime objective here is to test the modified discretization scheme for several pool boiling scenarios and the proposed algorithm is definitely successful on that count. Further, the highest absolute surface temperature considered here with R134a is a mere 411.6 K, which is not really high to render radiation significant.

6.8 Boiling Regimes with a Structured Heater

Appraisal of boiling heat transfer with engineered surfaces is of great practical relevance, as no real surface is perfectly flat in nature and structured surfaces have been reported to enhance the rate of heat transmission[156,178–180]. There are two possible reasons behind such augmentation in heat transfer. Along with an obvious increase in surface area with columnar structures, thereby directly raising the number of available nucleation sites, the gap between adjacent structures can also house a preexisting nucleus by trapping vapor. The obstructions also induce larger liquid advection, offering a quite dissimilar scenario compared to the plain heater. Therefore, we employ the SC-LBM algorithm with the modified discretization scheme to explore pool boiling with the structured heater shown in Fig. 40(c), and corresponding observations are summarized in Fig. 46 in terms of bubble profiles.

Snapshots presented in Fig. 46(a) refer to the nucleate boiling regime, with distinct bubble generation on different locations of the heater. As mentioned above, the gaps between the columns act as large rectangular cavities and are always occupied by the vapor phase, therefore consistently providing vapor embryos. The corners of the columns appear to be the most active nucleation site, owing to the structural discontinuity, and embryos appearing on the adjacent corners of neighboring columns can easily merge with each other, producing bigger bubbles. The boiling mechanism from rectangular cavities was explained by Mu et al.[181] for a low-density ratio of 10. Despite the density ratio adopted in our paper being about eight times that, the physics remain the same. Significantly higher liquid velocity beneath the departing bubbles has also been noted, which accelerates the upward motion of the bubble.

Transition boiling can be found from Fig. 46(b) for a wall superheat of 0.27. All the structures are covered by vapor film at $t = 6000$, which is definitely not the case at $t = 12000$. A couple of bubbles have already left the surface, completely destroying the film. The film remains unstable over the entire duration of computation. More stable film formation is possible with $\Delta T_{\text{sup}} = 0.31$ [Fig. 46(c)]. Even after the departure of several bubbles, the film continues to cover the entire heater, affirming the fully developed film boiling regime. The concerned physics is well established and the presented numerical results are consistent with the ones reported by Chang et al.[156], albeit for a substantially lower-density ratio of 10. Our modified discretization scheme, therefore, is able to successfully reproduce the pool boiling phenomenon on structured surfaces for higher-density ratios.

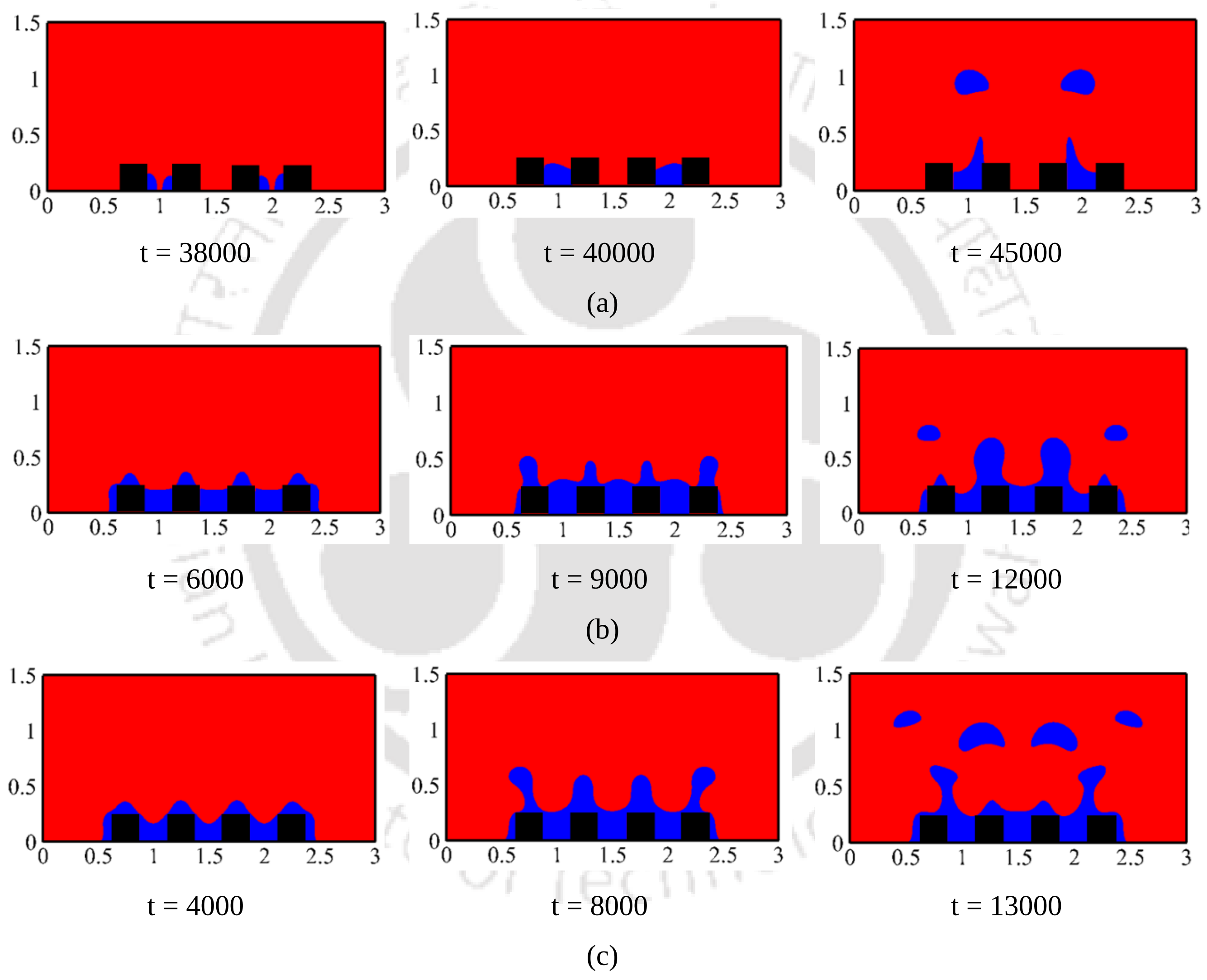

t = 38000 t = 40000 t = 45000

(a)

t = 6000 t = 9000 t = 12000

(b)

t = 4000 t = 8000 t = 13000

(c)

Fig. 46. Snapshots of pool boiling from a distributed plain heater in an open rectangular domain during (a) the nucleate regime with $\Delta T_{\text{sup}} = 0.21$, (b) transition boiling with $\Delta T_{\text{sup}} = 0.27$, (c) film boiling with $\Delta T_{\text{sup}} = 0.31$. Here red and blue colors, respectively, symbolize liquid and vapor phases. Nucleation can clearly be seen to initiate from the corners of the columnar structures.

6.9 Boiling Curves

As we have already observed, it is possible to experience different regimes of pool boiling with a change in wall superheat, with each having its own thermal characteristics. The presence of liquid in contact with the heated surface and enhanced bubble-induced fluid motion steeply increases the wall heat flux during nucleate boiling with rise in superheat. However, for a very high rate of vapor generation leading to the formation of bubble jets, movement of liquid to the heater is hindered, which affects the heat flux and results in a more moderate variation. The number of active nucleation sites also increases with surface temperature, which aids horizontal spreading of the vapor film through merging of bubbles, and consequent evolution to the transient regime. While the vapor area fraction during nucleate boiling remains restricted between 0.1 and 0.5 during the nucleate boiling [Fig. 43(b)], it hovers around 0.7 in the transition regime [Fig. 44(b)] and approaches unity once the film is fully developed. Vapor being a poor thermal conductor, the wall heat flux suffers drastically with such break in thermal communication during film boiling, as has already been observed from Fig. 45(b). After stabilization of the film, however, the heat flux starts climbing again, mostly as a linear function of the degree of superheat.

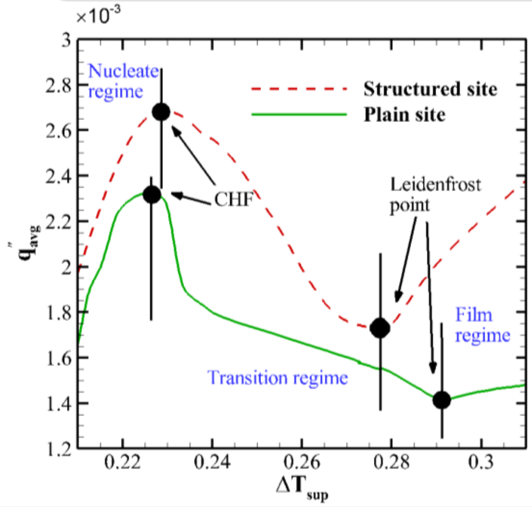

Fig. 47 Boiling curves with plain and structured distributed heaters in an open rectangular domain. The transition regime with the structured heater is noticeably shorter, with CHF getting shifted towards the right and the Leidenfrost point shifted towards the left. The heat flux level with the structured heater is also consistently higher than that with the plain heater, yielding a greater CHF value.

The above discussion is traditionally conceived in terms of the boiling curve[6] and the same approach is followed in Fig. 47, where we have plotted the time-average wall heat flux against the degree of superheat. Following Ma et al. [23], the average flux is defined as

$$\left(q''_{avg} = -\frac{1}{L_H \left(t_2 - t_1\right)} \int_{t_1}^{t_2} \int_{-L_H/2}^{L_H/2} k \left.\frac{\partial T_R}{\partial y}\right|_{y=0} dxdt \right) \tag{58}$$

where $(t_2 - t_1)$ is a very long time interval, which starts after the initiation of vapor generation. The culmination of the nucleate boiling regime is identified in terms of the critical heat flux (CHF), whereas the onset of film boiling corresponds to the Leidenfrost point. All the three modes of pool boiling, along with the transformation points, have nicely been represented for both plain and structured surfaces. As postulated earlier, the structured surface consistently enjoys greater heat flux for any specified superheat. The CHF value with the structured surface is also noticeably higher, as the peaks of the columns are more likely to remain in contact with the liquid than the plain surface. A higher rate of heat transfer also allows a stable film formation at comparatively lower superheat, thereby shifting the Leidenfrost point to the left and substantially limiting the extent of transition boiling.

A quantitative validation is attempted by allegorizing the CHF predicted for the plain surface with correlations from literature, and the well-known Zuber relation[2] is employed for the same, which has the following form:

$$q''_{CHF} = K h_{fg} \rho_v \left[\frac{\sigma g \left(\rho_l - \rho_v\right)}{\rho_v^2} \right] \tag{59}$$

Sun and Lienhard (from Ghiaasian[2]) suggested a value of 0.149 for the constant K, which yields a theoretical CHF value of 2.079 × 10^{-3} lattice units for R134a with the present domain, whereas our simulation produces an anticipated CHF value of 2.33×10^{-3} lattice units, which is within 10% accuracy level, and hence can be considered to be satisfactory.

6.10 Effect of Surface Wettability

The numerical approach of incorporating the surface wettability force in our algorithm is one final aspect to be discussed. The false wall density appearing in Eq. (36a) is a direct representation of the contact angle effective at the three-phase interface, as can be comprehended from Fig. 48. It is definite that a value of

ρ_w closer to liquid density yields a low contact angle, whereas the reverse is true for a value approaching vapor density. A higher contact angle refers to a reduction in surface wettability, which allows the vapor to accumulate over the heated surface more easily, causing a decline in the heat transfer rate and hence a greater penchant towards film boiling. The same can be substantiated from Fig. 49, where two different contact angles have been explored, namely, 39.22^0 to 56.97^0, with the configuration probed earlier. It can be seen from the figures that, for the same wall superheat and at the same time instants, the fluid with greater contact angle is able to spread wider over the heater. Variations in vapor area fraction and surface heat flux with time are presented in Fig. 49(c) for the sake of quantification, and that firmly supports our earlier discussion.

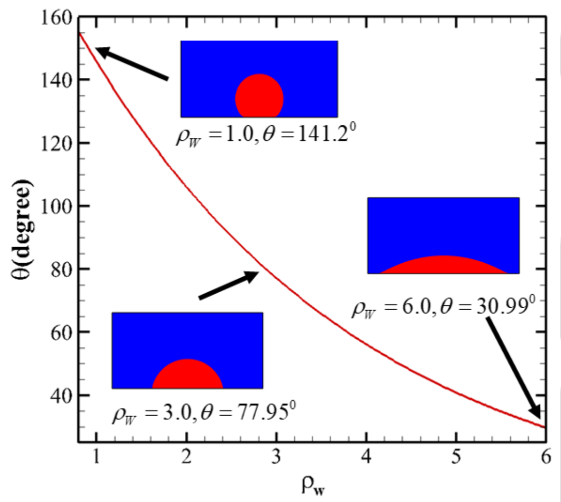

Fig. 48 The static contact angle inversely varies with the false wall density and approaches the theoretical extremes of 0^0 and 180^0 on assuming the limiting density values corresponding to vapor and liquid, respectively, as shown within the insets.

The boiling curve is also strongly affected by the contact angle, as is illustrated in Fig. 49(d). Heat transfer rate for a fluid with a lower contact angle being relatively higher, the effect of vapor accumulation owing to the vertical merging of bubbles is delayed quite noticeably. Around the point of onset of nucleate boiling, the surface is mostly in contact with the liquid and hence there is no prominent effect of the contact angle on the boiling curves. However, the curves veer from each other with rise in wall superheat. The difference in respective CHF values is quite remarkable, considering the change in selected contact angles is not very large.

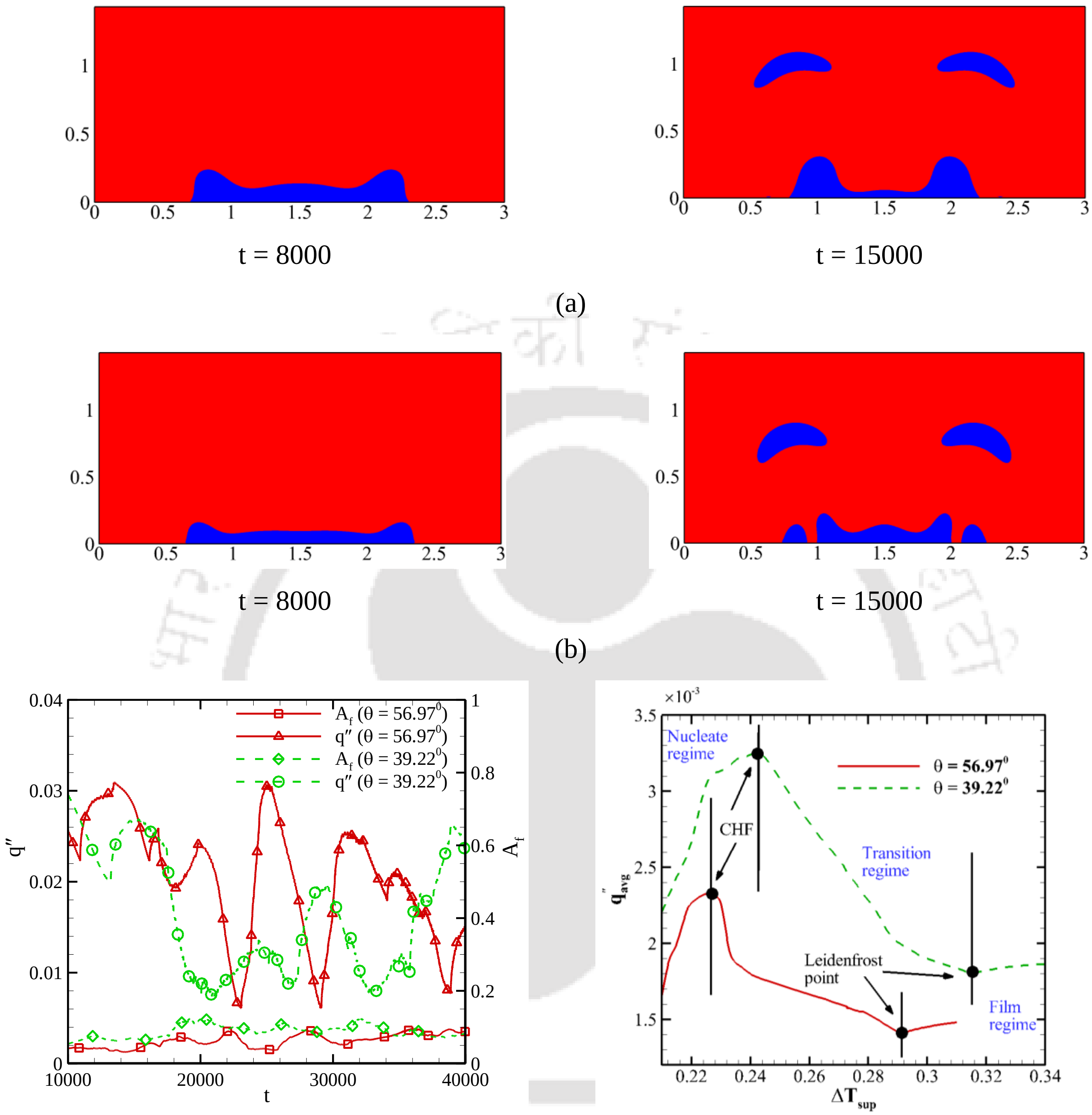

(c)

(d)

Fig. 49 Effect of contact angle on the nature of bubble nucleation demonstrated for (a) $\theta = 39.22^0$ and (b) $\theta = 56.97^0$, with red and blue colors, respectively, symbolizing liquid and vapor phases; (c) temporal variations in wall heat flux and vapor area fraction for $\Delta T_{\text{sup}} = 0.25$; and (d) boiling curves for the same contact angles. Fluid with higher contact angle clearly shows a greater inclination towards stable film formation, resulting in a substantial reduction in CHF under identical operating conditions.

This particular observation of reduction in CHF with enhancement in contact angle is well documented in literature[182–184]. So we can conclude that the modified discretization scheme is successful in capturing the effect of contact angle and surface wettability on pool boiling.

6.11 Summary

A detailed discussion regarding the deployment of the pseudopotential-based lattice Boltzmann method for simulation of pool boiling is presented here. While it has received conspicuous recognition in literature over the last couple of decades, inherent thermodynamic inconsistency of the basic algorithm has limited its application to low-density ratios and hence only around the critical point of a fluid. We, therefore, attempt to reinforce the existing approach, through simultaneous enhancement of isotropy of the discrete equation and thermodynamic consistency of the overall formulation, by reshaping the interparticle interaction term and extending its discretization to the eighth order. The immediate consequence of such augmentation can be envisaged following the stabilization of a static liquid droplet in a periodic domain. The proposed algorithm is able to coax about 113% reduction in the largest spurious velocity around the curved interface for comparable density ratios, while sustaining the simulation at a density ratio of 620, which is a substantial improvement over about 174 for the existing schemes. Predicted phasic densities also complied well with the Maxwell area reconstruction rule, thereby providing an indirect validation.

Several pool boiling scenarios have been explored to demonstrate the capability of the proposed algorithm. Consistent with earlier SC-LB procedures, it successfully simulates the nucleation on the superheated surface, without necessitating any assumed nucleus. A complete ebullition cycle is produced using a microheater on both rectangular and cylindrical configurations, as well as with distributed planar and structured heater surfaces. All three regimes of pool boiling, namely, nucleate, transition, and film boiling, have been captured with precision, along with their standard characteristics in terms of heat transfer coefficient and vapor area fraction, facilitating the development of a complete boiling curve. The CHF value predicted for the planar heater matches within 10% with the well-celebrated relation of Zuber, which substantiates its proficiency in simulation of pool boiling. To our knowledge, such an attempt of correlating a computational inference with an empirical relation is rare in the LB community, particularly for multiphase models, and that speaks volumes about the diligence of the proposed augmentation in the SRT-SC-LB algorithm.

Chapter 7

Major Contributions and Scope of Future Research

A numerical solver based on pseudopotential based thermal multiphase model is developed in this work, which is capable of simulating phase-change heat transfer problems like boiling and condensation in complex geometries. Both SRT and MRT based approaches are taken into consideration while developing the in-house code. The SRT-SC-LB method is used to simulate a flow boiling problem in a two-dimensional rectangular channel, whereas the MRT-SC-LB model is used to analyze condensate droplet formation and movement on nano/microstructured rough surfaces. An algorithmic modification of the SRT-SC-LB method has also been proposed to enhance its capability in simulating high density ratio phase change heat transfer problems. The Major contributions from this thesis are summarized in the following section.

7.1 Major contributions

The applicability of the SRT-SC-LBM has been successfully extended to simulate flow boiling in a narrow horizontal channel. Bubble dynamics and the involved two-phase flow physics are investigated, and the effect of different parameters like wall superheat, inlet velocity, and surface wettability on the bubble departure diameter, release period, and pressure drop are investigated in detail. It has been found that an increase in the wall superheat increases the bubble departure diameter, while the bubble release period decreases. If the mass flux is decreased at the inlet, both the average bubble departure diameter and average bubble release period increase. A flow regime map based on wall superheat and inlet mass flux is generated using several datapoints, which indicates that an increase in the wall superheat or decrease in the mass flux tends to change the flow pattern from single-phase to bubbly to slug flow. Effect of surface wettability has also been demonstrated through two different cases. If the contact angle is increased, bubble departure diameter and average bubble release period increase, though the effect is comparatively smaller than the effect of inlet mass flux or wall superheat. Finally, from the inferences of this study, it can be concluded that LBM can be used to solve the nucleate boiling problem and capture the flow physics involved with the underlying thermal hydraulics.

MRT-SC-LBM based multiphase model is used to study condensation on rough nanostructured surfaces with a cold spot on the bottom surface. Different nucleation modes and final states of condensate droplets are elaborated in detail through sequential snapshots. Four types of droplet nucleation modes and final state have been observed in our simulation based on different roughness topology – Cassie state with top nucleation mode, Cassie state with side nucleation mode, Wenzel state with side nucleation mode and Wenzel state with bottom nucleation mode. A phase diagram is plotted by varying the geometric parameters of the nanopillars to demonstrate the combined effect of pillar dimensions which indicates that the variation of height, width and spacing of the pillars reveal that a substrate with larger height and closely packed pillars will support the formation of Cassie droplet, whereas increment in the interpillar spacing and reduction in pillar height destroy the superhydrophobicity of the surface by generating Wenzel droplet. Also, the nucleation initiation time, heat transfer, and mass condensation rate for different surface roughness parameters are aptly demonstrated. The initial mass condensation rate is higher for surfaces forming Wenzel droplets, though the amount of surface heat transfer is almost the same. Also, droplet nucleation starts earlier in the surfaces with larger pillar spacing and shorter pillars as the apparent wettability of those surfaces is higher. Consideration of varying cold spot temperatures to analyze the effect of thermal perturbation is a novelty of this work, which has not been studied numerically yet. It has been observed that a change of cold spot temperature can convert the condensate droplet state from Cassie to Wenzel state. Finally, it can be concluded that a surface with larger pillar height, smaller interpillar spacing and optimal temperature difference between cold surface and the saturated vapor will be most beneficial to maintain the superhydrophobicity of the surface and most useful for industrial application where superhydrophbic surfaces are needed for condensation.

The same numerical framework (MRT-SC-LB) is employed to analyzed condensate droplet formation and movement on vertical and inclined microstructured rough surfaces. Two surfaces with disparate roughness configurations are used for this purpose, one of which generates Cassie droplet upon condensation on a horizontal surface, while a Wenzel droplet is formed on the other surface with higher interpillar spacing and short height pillars. When the orientations of the same surfaces are vertical, DWC and FWC can be observed. The rough surface responsible for a Cassie droplet formation promotes DWC, whereas FWC prevails on the other one. The heat transfer rate and the mass condensation rate for both surfaces are compared. It has been observed that the heat transfer rate for DWC is much higher than FWC. The effect of surface inclination has been studied in detail considering six different inclinations. As the gravity force reduces due to surface inclination, the droplet removal procedure becomes slower and covers the cold surface for a higher amount of time, though DWC is maintained. This reduces the mass condensation and heat transfer rate as expected. Finally, it can be said that a surface with lower interpillar spacing and taller pillars in vertical orientation will have a better chance to prevail DWC and suitable industrial applications.

A novel algorithm based on SRT-SC-LB model is proposed which can reduce the spurious current around a curved two-phase interface and increase numerical stability. With the help of this new-found model, we have been able to simulate high density ratio boiling simulations which were not possible earlier with the SRT-SC-LB multiphase model. The proposed algorithm has been tested for several cases involving pool boiling in a domain filled with saturated liquid. It has been successfully simulated nucleate boiling in a rectangular domain with a microheater at the bottom wall at a density ratio around 80. A cylindrical domain with a small rotating cylinder kept inside a big one is also considered as a test case. A microheater is mounted on the top of the small cylinder, which is rotating with a constant angular velocity. Temporal sequential snapshots of periodically generating and departing vapor bubble has ensured that the algorithm can capture the physics correctly. A distributed heater is positioned in place of the microheater in a larger sized domain to simulate different boiling regimes. It has been observed that the model works perfectly to simulate the nucleate, transition and film boiling regimes with the use of a wide heater at the bottom wall, and predict the trends of the heat transfer rate at each zone for different degrees of wall superheat at plain and structured heater sites. Finally, from the inferences of the present analysis, it can be concluded that the present developed model works well for high density ratio boiling problems.

7.2 Future Scope

The developed numerical solver can be extended and used for several phase change heat transfer problems. The future works that can be done with this model are detailed below –

- The developed pseudopotential based in-house LB code can be used for the exploration of boiling and condensation related problems in different physical scenarios.

- Different kinds of external field forces like electric and magnetic fields can be incorporated into the numerical framework to explore complex multiphysics problems.
- Applicability of the model can be extended to solve fluid dynamics and heat transfer problems with variable properties. With the help of this extension problems related to supercritical fluids can be simulated.
- The proposed multirange SC-LB model can be combined with the MRT model which can enhance the stability of the scheme, and it may simulate much larger density ratio-based multiphase problems.

Appendix A

In this appendix discretized form of the modified SC force (Eq. 39) in both x and y direction $\left(F_x, F_y\right)$ for $D2Q9$ lattice are given in detail :

$$
\begin{aligned}
F_{x_{i,j}} = &-G\beta\psi_{i,j}\Delta t\left[\begin{array}{l}
\varphi_1\left(\psi_{i+1,j}-\psi_{i-1,j}\right)+\varphi_2\left(\psi_{i+1,j+1}-\psi_{i-1,j+1}+\psi_{i+1,j-1}-\psi_{i-1,j-1}\right)+\varphi_4\left\{2\left(\psi_{i+2,j}-\psi_{i-2,j}\right)\right\} \\
+\varphi_5\left\{2\left(\psi_{i+2,j+1}-\psi_{i-2,j+1}+\psi_{i+2,j-1}-\psi_{i-2,j-1}\right)+\psi_{i+1,j+2}-\psi_{i-1,j+2}+\psi_{i+1,j-2}-\psi_{i-1,j-2}\right\} \\
+\varphi_8\left\{2\left(\psi_{i+2,j+2}-\psi_{i-2,j+2}+\psi_{i+2,j-2}-\psi_{i-2,j-2}\right)\right\}
\end{array}\right] \\
&+-G\left(\frac{1-\beta}{2}\right)\Delta t\left[\begin{array}{l}
\varphi_1\left(\psi^2_{i+1,j}-\psi^2_{i-1,j}\right)+\varphi_2\left(\psi^2_{i+1,j+1}-\psi^2_{i-1,j+1}+\psi^2_{i+1,j-1}-\psi^2_{i-1,j-1}\right)+\varphi_4\left\{2\left(\psi^2_{i+2,j}-\psi^2_{i-2,j}\right)\right\} \\
+\varphi_5\left\{2\left(\psi^2_{i+2,j+1}-\psi^2_{i-2,j+1}+\psi^2_{i+2,j-1}-\psi^2_{i-2,j-1}\right)+\psi^2_{i+1,j+2}-\psi^2_{i-1,j+2}+\psi^2_{i+1,j-2}-\psi^2_{i-1,j-2}\right\} \\
+\varphi_8\left\{2\left(\psi^2_{i+2,j+2}-\psi^2_{i-2,j+2}+\psi^2_{i+2,j-2}-\psi^2_{i-2,j-2}\right)\right\}
\end{array}\right]
\end{aligned}
\qquad \text{(A1)}
$$

$$
\begin{aligned}
F_{y_{i,j}} = &-G\beta\psi_{i,j}\Delta t\left[\begin{array}{l}
\varphi_1\left(\psi_{i,j+1}-\psi_{i,j-1}\right)+\varphi_2\left(\psi_{i+1,j+1}-\psi_{i+1,j-1}+\psi_{i-1,j+1}-\psi_{i-1,j-1}\right)+\varphi_4\left\{2\left(\psi_{i,j+2}-\psi_{i,j-2}\right)\right\} \\
+\varphi_5\left\{2\left(\psi_{i+2,j+1}-\psi_{i+2,j-1}+\psi_{i-2,j+1}-\psi_{i-2,j-1}\right)+\psi_{i+1,j+2}-\psi_{i+1,j-2}+\psi_{i-1,j+2}-\psi_{i-1,j-2}\right\} \\
+\varphi_8\left\{2\left(\psi_{i+2,j+2}-\psi_{i+2,j-2}+\psi_{i-2,j+2}-\psi_{i-2,j+2}\right)\right\}
\end{array}\right] \\
&+-G\left(\frac{1-\beta}{2}\right)\Delta t\left[\begin{array}{l}
\varphi_1\left(\psi^2_{i,j+1}-\psi^2_{i,j-1}\right)+\varphi_2\left(\psi^2_{i+1,j+1}-\psi^2_{i+1,j-1}+\psi^2_{i-1,j+1}-\psi^2_{i-1,j-1}\right)+\varphi_4\left\{2\left(\psi^2_{i,j+2}-\psi^2_{i,j-2}\right)\right\} \\
+\varphi_5\left\{2\left(\psi^2_{i+2,j+1}-\psi^2_{i+2,j-1}+\psi^2_{i-2,j+1}-\psi^2_{i-2,j-1}\right)+\psi^2_{i+1,j+2}-\psi^2_{i+1,j-2}+\psi^2_{i-1,j+2}-\psi^2_{i-1,j-2}\right\} \\
+\varphi_8\left\{2\left(\psi^2_{i+2,j+2}-\psi^2_{i+2,j-2}+\psi^2_{i-2,j+2}-\psi^2_{i-2,j-2}\right)\right\}
\end{array}\right]
\end{aligned}
\qquad \text{(A2)}
$$

Values of $\varphi_1..\varphi_8$ are provided in Table 1. Value of G is not needed as it is cancelled out when the value of ψ is inserted in the above equations from Eq. (31). Gong et al. [45] concluded that using $\beta = 1.16$ for PR EOS gives the optimal result. But, it is found that with this new form of the discretized force $\beta = 1.19$ provides the best match with the coexistence curve.

Appendix B

Following the work of Gong et al.[112], capillary length scale of a fluid is used for the LB and physical unit conversion procedure in this work. The capillary length of a fluid can be written as - $l_0 = \sqrt{\sigma / g\left(\rho_l - \rho_v\right)}$

The capillary length of a fluid can be calculated in physical and LB units, and unit conversion factor can be obtained by equating them as:

$$l_0^{lu} = \sqrt{\frac{\sigma^{lu}}{g^{lu}\left(\rho_l^{lu} - \rho_v^{lu}\right)}} = l_0^{real} = \sqrt{\frac{\sigma^{real}}{g^{real}\left(\rho_l^{real} - \rho_v^{real}\right)}} \tag{B1}$$

The real physical values of coexisting densities $\left(\rho_{l,}\rho_v\right)$ and surface tension (σ) for a specific reduced temperature (T_R) is taken form REFPROP. The analytical values of those parameters for a specific reduced temperature can be calculated with the help of Maxwell area construction curve. The characteristic time scale is defined as - $t_0 = \sqrt{l_0 / g_0}$. The time conversion can be calculated by equating characteristic time scales for LB and physical units.

$$t_0^{lu} = \sqrt{\frac{l^{lu}}{g^{lu}}} = t_0^{real} = \sqrt{\frac{l^{real}}{g^{real}}} \tag{B2}$$

Table 1: Discretization coefficients $(\varphi_1, \varphi_2 ....\varphi_8)$ upto 8th order approximation of SC force for $D2Q9$ lattice[162]

Tensor	φ_1	φ_2	φ_3	φ_4	φ_5	φ_6	φ_8
$E^{(4)}$	$1/3$	$1/12$	0	0	0	0	0
$E^{(8)}$	$4/21$	$4/45$	0	$1/60$	$2/315$	0	$1/5040$

References

1. Zu, Y. Q., Yan, Y. Y., Gedupudi, S., Karayiannis, T. G. & Kenning, D. B. R. Confined bubble growth during flow boiling in a mini-/micro-channel of rectangular cross-section part II: Approximate 3-D numerical simulation. *Int. J. Therm. Sci.* **50**, 267–273 (2011).

2. Ghiaasiaan, S. M. *Two-Phase Flow, Boiling and Condensation: In Conventional and Miniature Systems*. (Cambridge University Press, 2007).

3. Rykaczewski, K., Landin, T., Walker, M. L., Scott, J. H. J. & Varanasi, K. K. Direct imaging of complex nano- to microscale interfaces involving solid, liquid, and gas phases. *ACS Nano* **6**, 9326–9334 (2012).

4. Yuan, P. & Schaefer, L. Equations of state in a lattice Boltzmann model. *Phys. Fluids* **18**, 042101 (2006).

5. Kruger, T. *et al. The Lattice Boltzmannn Method: Principles and Practices*. (Spirnger, 2017). doi:10.1007/978-3-319-44649-3.

6. Collier, J. G. & Thome, J. R. Convective Boiling and Condensation. (1994).

7. Hardy, J., Pomeau, Y. & Pazzis, O. d. Time Evolution of a Two Dimensional Classical Lattice System. *Phys. Rev. Lett.* **31**, 276–279 (1975).

8. Sarkar, P. A brief history of cellular automata. *ACM Comput. Surv.* **32**, 80–107 (2000).

9. Frisch, U., Hasslacher, B. & Pomeau, Y. Lattice-gas automata for the Navier-Stokes equation. *Phys. Rev. Lett.* **56**, 1505–1508 (1986).

10. D'Humières, D., Lallemand, P. & Frisch, U. Lattice Gas models for 3D hydrodynamics. *Europhys. Lett.* **2**, 291–297 (1986).

11. McNamara, G. R. & Zanetti, G. Use of the Boltzmann Equation to Simulate Lattice-gas Automata. *Phys. Rev. Lett.* **61**, 2332–2335 (1988).

12. Higuera, F. & Jiménez, J. Boltzmann Appraoch to Lattice Gas Simulations. *Europhys. Lett.* **9**, 663–668 (1989).

13. Bhatnagar, P. L., Gross, E. M. & Krook, M. A Model for Collision Processes in Gases. I. Small

Amplitude Processes in Charged and Neutral One-Component Systems. *Phys. Rev.* **94**, 511–525 (1954).

14. Chen, S., Chen, H., Martnez, D. & Matthaeus, W. Lattice Boltzmann model for simulation of magnetohydrodynamics. *Phys. Rev. Lett.* **67**, 3776–3779 (1991).

15. Koelman, J. A Simple Lattice Boltzmann Scheme for Navier-Stokes Fluid Flow. *Europhys. Lett.* **15**, 603 (1991).

16. Lallemand, P. & Luo, L.-S. Theory of the lattice Boltzmann method: dispersion, dissipation, isotropy, Galilean invariance, and stability. *Phys. Rev. E* **61**, 6546–6562 (2000).

17. He, Y. L., Liu, Q., Li, Q. & Tao, W. Q. Lattice Boltzmann methods for single-phase and solid-liquid phase-change heat transfer in porous media: A review. *Int. J. Heat Mass Transf.* **129**, 160–197 (2019).

18. Alexander, F. J., Chen, S. & Sterling, J. D. Lattice Boltzmann thermohydrodynamics. *Phys. Rev. E* **47**, (1993).

19. Bartoloni, A. *et al.* LBE simulations of the Rayleigh-Benard Convection on the APE100 Parallel Processor. *Int. J. Mod. Phys. C* **04**, 993–1006 (1993).

20. Eggels, J. G. M. & Somers, J. A. Numerical simulation of free convective flow using the lattice-Boltzmann scheme. *Int. J. Heat Fluid Flow* **16**, 357–364 (1995).

21. He, X., Chen, S. & Doolen, G. D. A Novel Thermal Model for the Lattice Boltzmann Method in Incompressible Limit. *J. Comput. Phys.* **146**, 282–300 (1998).

22. Peng, Y., Shu, C. & Chew, Y. T. Simplified thermal lattice Boltzmann model for incompressible thermal flows. *Phys. Rev. E - Stat. Physics, Plasmas, Fluids, Relat. Interdiscip. Top.* **68**, 8 (2003).

23. Guo, Z., Zheng, C., Shi, B. & Zhao, T. S. Thermal lattice Boltzmann equation for low Mach number flows: Decoupling model. *Phys. Rev. E - Stat. Nonlinear, Soft Matter Phys.* **75**, 1–15 (2007).

24. Filippova, O. & Hanel, D. Lattice-BGK models for low Mach number combustion. *Int. J. Mod. Phys. C* **9**, 1439–1445 (1998).

25. Filippova, O. & Hänel, D. A Novel Lattice BGK Approach for Low Mach Number Combustion.

J. Comput. Phys. **158**, 139–160 (2000).

26. Lallemand, P. & Luo, L. S. Theory of the lattice Boltzmann method: Acoustic and thermal properties in two and three dimensions. *Phys. Rev. E - Stat. Physics, Plasmas, Fluids, Relat. Interdiscip. Top.* **68**, 25 (2003).

27. Rothman, D. H. & Keller, J. M. Immiscible cellular-automaton fluids. *J. Stat. Phys.* **52**, 1119–1127 (1988).

28. Gunstensen, A. K., Rothman, D. H., Zaleski, S. & Zanetti, G. Lattice Boltzmann model of immiscible fluids. *Phys. Rev. A* **43**, 4320–4327 (1991).

29. Grunau, D., Chen, S. & Eggert, K. A lattice Boltzmann model for multiphase fluid flows. *Phys. Fluids A* **5**, 2557–2562 (1992).

30. Lishchuk, S. V., Care, C. M. & Halliday, I. Lattice Boltzmann algorithm for surface tension with greatly reduced microcurrents. *Phys. Rev. E - Stat. Physics, Plasmas, Fluids, Relat. Interdiscip. Top.* **67**, 5 (2003).

31. Reis, T. & Phillips, T. N. Lattice Boltzmann model for simulating immiscible two-phase flows. *J. Phys. A Math. Theor.* **40**, 4033 (2007).

32. Liu, H., Valocchi, A. J. & Kang, Q. Three-dimensional lattice Boltzmann model for immiscible two-phase flow simulations. *Phys. Rev. E - Stat. Nonlinear, Soft Matter Phys.* **85**, 1–14 (2012).

33. Huang, H., Huang, J. J. & Lu, X. Y. Study of immiscible displacements in porous media using a color-gradient-based multiphase lattice Boltzmann method. *Comput. Fluids* **93**, 164–172 (2014).

34. Wu, L., Tsutahara, M., Kim, L. S. & Ha, M. Y. Three-dimensional lattice Boltzmann simulations of droplet formation in a cross-junction microchannel. *Int. J. Multiph. Flow* **34**, 852–864 (2008).

35. Leclaire, S., Reggio, M. & Trépanier, J. Y. Numerical evaluation of two recoloring operators for an immiscible two-phase flow lattice Boltzmann model. *Appl. Math. Model.* **36**, 2237–2252 (2012).

36. Leclaire, S., Reggio, M. & Trépanier, J. Y. Isotropic color gradient for simulating very high-density ratios with a two-phase flow lattice Boltzmann model. *Comput. Fluids* **48**, 98–112 (2011).

37. Huang, H., Sukop, M. C. & Lu, X.-Y. *Multiphase lattice Boltzmann methods: theory and*

application. (John Wiley and Sons Ltd., 2015).

38. Shan, X. & Chen, H. Lattice Boltzmann model for simulating flows with multiple phases and components. *Phys. Rev. E* **47**, 1815–1819 (1993).

39. Shan, X. Pressure tensor calculation in a class of nonideal gas lattice Boltzmann models. *Phys. Rev. E - Stat. Nonlinear, Soft Matter Phys.* **77**, 1–6 (2008).

40. Chen, L., Kang, Q., Mu, Y., He, Y. L. & Tao, W. Q. A critical review of the pseudopotential multiphase lattice Boltzmann model: Methods and applications. *Int. J. Heat Mass Transf.* **76**, 210–236 (2014).

41. Sbragaglia, M. *et al.* Generalized lattice Boltzmann method with multirange pseudopotential. *Phys. Rev. E - Stat. Nonlinear, Soft Matter Phys.* **75**, 1–13 (2007).

42. Zhang, J. & Tian, F. A bottom-up appraoch to non-ideal fluids in the lattice Boltzmann methods. *Europhys. Lett.* **81**, 66005 (2008).

43. Kupershtokh, A. L., Medvedev, D. A. & Karpov, D. I. On equations of state in a lattice Boltzmann method. *Comput. Math. with Appl.* **58**, 965–974 (2009).

44. Kupershtokh, A. L. & Medvedev, D. A. Lattice Boltzmann equation method in electrohydrodynamic problems. *J. Electrostat.* **64**, 581–585 (2006).

45. Gong, S. & Cheng, P. Numerical investigation of droplet motion and coalescence by an improved lattice Boltzmann model for phase transitions and multiphase flows. *Comput. Fluids* **53**, 93–104 (2012).

46. Mccracken, M. E. & Abraham, J. Multiple-relaxation-time lattice-Boltzmann model for multiphase flow. *Phys. Rev. E* **71**, 036701 (2005).

47. Yu, Z. & Fan, L. S. Multirelaxation-time interaction-potential-based lattice Boltzmann model for two-phase flow. *Phys. Rev. E - Stat. Nonlinear, Soft Matter Phys.* **82**, 1–14 (2010).

48. Li, Q., Luo, K. H. & Li, X. J. Lattice Boltzmann modeling of multiphase flows at large density ratio with an improved pseudopotential model. *Phys. Rev. E* 053301 (2013) doi:10.1103/PhysRevE.87.053301.

49. Swift, M. R., Osborn, W. R. & Yeomans, J. M. Lattice Boltzmann Simulation of Nonideal Fluids.

Phys. Rev. Lett.* **75**, 830–834 (1995).

50. Swift, M. R., Orlandini, E., Osborn, W. R. & Yeomans, J. M. Lattice Boltzmann simulations of liquid-gas and binary fluid systems. *Phys. Rev. E - Stat. Physics, Plasmas, Fluids, Relat. Interdiscip. Top.* **54**, 5041–5052 (1996).

51. Luo, L.-S. Unified Theory of Lattice Boltzmann Models for Nonideal Gases. *Phys. Rev. Lett.* **81**, 1618–1621 (1998).

52. Holdych, D., Georgiadis, J. G. & Buckius, R. An improved hydrodynamics formulation for multiphase flow lattice-Boltzmann models. *Int. J. Mod. Phys. C* **9**, 1393–1404 (1998).

53. Frank, X., Funfschilling, D., Midoux, N. & Li, H. Z. Bubbles in a viscous liquid: Lattice Boltzmann simulation and experimental validation. *J. Fluid Mech.* **546**, 113–122 (2006).

54. Hao, L. & Cheng, P. Lattice Boltzmann simulations of liquid droplet dynamic behavior on a hydrophobic surface of a gas flow channel. *J. Power Sources* **190**, 435–446 (2009).

55. Gonnella, G., Orlandini, E. & Yeomans, J. M. Spinodal decomposition to a lamellar phase: Effects of hydrodynamic flow. *Phys. Rev. Lett.* **78**, 1695–1698 (1997).

56. Kendon, V. M., Cates, M. E., Pagonabarraga, I., Desplat, J. C. & Bladon, P. Inertial effects in three-dimensional spinodal decomposition of a symmetric binary fluid mixture: A lattice Boltzmann study. *J. Fluid Mech.* **440**, 147–203 (2001).

57. Suppa, D., Kuksenok, O., Balazs, A. C. & Yeomans, J. M. Phase separation of a binary fluid in the presence of immobile particles: A lattice Boltzmann approach. *J. Chem. Phys.* **116**, 6305–6310 (2002).

58. Holdych, D. J., Georgiadis, J. G. & Buckius, R. O. Migration of a van der Waals bubble: Lattice Boltzmann formulation. *Phys. Fluids* **13**, 817–825 (2001).

59. Hao, L. & Cheng, P. Lattice Boltzmann simulations of water transport in gas diffusion layer of a polymer electrolyte membrane fuel cell. *J. Power Sources* **195**, 3870–3881 (2010).

60. Inamuro, T., Ogata, T., Tajima, S. & Konishi, N. A lattice Boltzmann method for incompressible two-phase flows with large density differences. *J. Comput. Phys.* **198**, 628–644 (2004).

61. Zheng, H. W., Shu, C. & Chew, Y. T. A lattice Boltzmann model for multiphase flows with large

density ratio. **218**, 353–371 (2006).

62. Fakhari, A. & Rahimian, M. H. Phase-field modeling by the method of lattice boltzmann equations. *Phys. Rev. E - Stat. Nonlinear, Soft Matter Phys.* **81**, 1–16 (2010).

63. He, X., Chen, S. & Zhang, R. A Lattice Boltzmann Scheme for Incompressible Multiphase Flow and Its Application in Simulation of Rayleigh-Taylor Instability. *J. Comput. Phys.* **152**, 642–663 (1999).

64. Lee, T. & Lin, C. L. A stable discretization of the lattice Boltzmann equation for simulation of incompressible two-phase flows at high density ratio. *J. Comput. Phys.* **206**, 16–47 (2005).

65. Lee, T. & Fischer, P. F. Eliminating parasitic currents in the lattice Boltzmann equation method for nonideal gases. *Phys. Rev. E - Stat. Nonlinear, Soft Matter Phys.* **74**, 1–15 (2006).

66. Amaya-Bower, L. & Lee, T. Single bubble rising dynamics for moderate Reynolds number using Lattice Boltzmann Method. *Comput. Fluids* **39**, 1191–1207 (2010).

67. Lee, T. & Liu, L. Lattice Boltzmann simulations of micron-scale drop impact on dry surfaces. *J. Comput. Phys.* **229**, 8045–8063 (2010).

68. He, X. & Doolen, G. D. Thermodynamic foundations of kinetic theory and Lattice Boltzmann models for multiphase flows. *J. Stat. Phys.* **107**, 309–328 (2002).

69. Hou, S., Shan, X., Zou, Q., Doolen, G. D. & Soll, W. E. Evaluation of two lattice Boltzmann models for multiphase flows. *J. Comput. Phys.* **138**, 695–713 (1997).

70. Huang, H., Wang, L. & Lu, X. Y. Evaluation of three lattice Boltzmann models for multiphase flows in porous media. *Comput. Math. with Appl.* **61**, 3606–3617 (2011).

71. Dong, Z., Li, W. & Song, Y. Lattice Boltzmann simulation of growth and deformation for a rising vapor bubble through superheated liquid. *Numer. Heat Transf. Part A Appl.* **55**, 381–400 (2009).

72. Dong, Z., Li, W. & Song, Y. A numerical investigation of bubble growth on and departure from a superheated wall by lattice Boltzmann method. *Int. J. Heat Mass Transf.* **53**, 4908–4916 (2010).

73. Sun, T. & Li, W. Three-dimensional numerical simulation of nucleate boiling bubble by lattice Boltzmann method. *Comput. Fluids* **88**, 400–409 (2013).

74. Safari, H., Rahimian, M. H. & Krafczyk, M. Extended lattice Boltzmann method for numerical simulation of thermal phase change in two-phase fluid flow. *Phys. Rev. E - Stat. Nonlinear, Soft Matter Phys.* **88**, 1–12 (2013).

75. Safari, H., Rahimian, M. H. & Krafczyk, M. Consistent simulation of droplet evaporation based on the phase-field multiphase lattice Boltzmann method. *Phys. Rev. E - Stat. Nonlinear, Soft Matter Phys.* **90**, 1–13 (2014).

76. Begmohammadi, A., Farhadzadeh, M. & Rahimian, M. H. Simulation of pool boiling and periodic bubble release at high density ratio using lattice Boltzmann method. *Int. Commun. Heat Mass Transf.* **61**, 78–87 (2015).

77. Tanaka, Y., Yoshino, M. & Hirata, T. Lattice Boltzmann simulation of nucleate pool boiling in saturated liquid. *Commun. Comput. Phys.* **9**, 1347–1361 (2011).

78. Zhang, R. & Chen, H. Lattice Boltzmann method for simulations of liquid-vapor thermal flows. *Phys. Rev. E - Stat. Physics, Plasmas, Fluids, Relat. Interdiscip. Top.* **67**, 6 (2003).

79. Hazi, G. & Markus, A. On the bubble departure diameter and release frequency based on numerical simulation results. *Int. J. Heat Mass Transf.* **52**, 1472–1480 (2009).

80. Gong, S. & Cheng, P. A lattice Boltzmann method for simulation of liquid-vapor phase-change heat transfer. *Int. J. Heat Mass Transf.* **55**, 4923–4927 (2012).

81. Li, Q., Kang, Q. J., Francois, M. M., He, Y. L. & Luo, K. H. Lattice Boltzmann modeling of boiling heat transfer: The boiling curve and the effects of wettability. *Int. J. Heat Mass Transf.* **85**, 787–796 (2015).

82. Liu, X. & Cheng, P. Lattice Boltzmann simulation for dropwise condensation of vapor along vertical hydrophobic flat plates. *Int. J. Heat Mass Transf.* **64**, 1041–1052 (2013).

83. Zhang, C., Hong, F. & Cheng, P. Simulation of liquid thin film evaporation and boiling on a heated hydrophilic microstructured surface by Lattice Boltzmann method. *Int. J. Heat Mass Transf.* **86**, 629–638 (2015).

84. Házi, G. & Márkus, A. Modeling heat transfer in supercritical fluid using the lattice Boltzmann method. *Phys. Rev. E - Stat. Nonlinear, Soft Matter Phys.* **77**, 1–10 (2008).

85. Li, Q. *et al.* Lattice Boltzmann methods for multiphase flow and phase-change heat transfer. *Prog. Energy Combust. Sci.* **52**, 62–105 (2016).

86. Li, Q. *et al.* History, Advances, and Challenges in Liquid Flow and Flow Boiling Heat Transfer in Microchannels: A Critical Review. *Int. J. Multiph. Flow* **134**, 034001 (2017).

87. Prosperetti, A. & Tryggvason, G. *Computational methods for multiphase flow*. (Cambridge University Press, 2009).

88. H., Y. J. & Tu, J. *Computational techniques for multiphase flow*. (Butterworth-Heinemann, 2019).

89. Banerjee, S. & Chan, A. Seperated flow models-I. Analysis of the averaged and local instantaneous formulations. *Int. J. Multiph. Flow* **6**, 1–24 (1980).

90. Drew, D. A. Mathematical modeling of two-phase flow. *Annu. Rev. Fluid Mech.* **15**, 261–291 (1983).

91. Drew, D. A. & Passman, S. L. *Theory of Multicomponent Fluids*. (Springer Science and Business Media, 2006).

92. Kolev, N. I. *Multiphase flow Dynamics I, Fundamentals*. (Spirnger, 2007).

93. Ishhii, M. & Hibiki, T. *Thermo-fluid dynamics of two phase flow*. (Springer Science and Business Media, 2010).

94. Zuber, N. On the dispersed two-phase flow in the laminar flow regime. *Chem. Eng. Sci.* **19**, 897–917 (1964).

95. Ryskin, G. & Leal, L. G. Numerical Solution of Free-Boundary Problems in Fluid Mechanics. Part 2. Buoyancy-Driven Motion of a Gas Bubble Through a Quiescent Liquid. *J. Fluid Mech.* **148**, 19–35 (1984).

96. Shopov, P. J., Minev, P. D., Bazlekhov, I. V. & Zapryanov, Z. D. Interaction of a deformable bubble with a rigid wall at moderate Reynolds numbers. *J. Fluid Mech.* **219**, 241–271 (1990).

97. Fukai, J. *et al.* Wetting effects on the spreading of a liquid droplet colliding with a flat surface : Experiment and modeling. *Phys. Fluids* **236**, 1995 (2005).

98. Harlow, F. H. & Welch, J. E. Numerical Calculation of Time-Dependent Viscous Incompressible Flow of Fluid with Free Surface. *Phys. Fluids* **8**, 2182 (2005).

99. Son, G. & Dhir, V. K. Numerical Simulation of Saturated Film Boiling on a Horizontal Surface. *J. Heat Transfer* **119**, 519–533 (1997).

100. Hirt, C. . W. & Nichols, B. D. Volume of Fluid (VOF) Method for the Dynamics of Free Boundaries. *J. Comput. Phys.* **39**, 201–225 (1981).

101. Welch, S. W. J. & Wilson, J. A Volume of Fluid Based Method for Fluid Flows with Phase Change. *J. Comput. Phys.* **160**, 662–682 (2000).

102. Jacqmin, D. Calculation of Two-Phase Navier – Stokes Flows Using Phase-Field Modeling. *J. Comput. Phys.* **155**, 96–127 (1999).

103. Guo, D. Z. *et al.* Phase Change Heat Transfer Simulation for Boiling Bubbles Arising from a Vapor Film by the VOSET Method. *Numer. Heat Transf. Part A Appl.* **59**, 857*881 (2011).

104. Deka, H., Biswas, G., Chakraborty, S. & Dalal, A. Coalescence dynamics of unequal sized drops. *Phys. Fluids* **31**, 012105 (2019).

105. Mukherjee, A. & Kandlikar, S. G. Numerical simulation of growth of a vapor bubble during flow boiling of water in a microchannel. *Microfluid. Nanofluidics* **1**, 137–145 (2005).

106. Mukherjee, A. & Kandlikar, S. G. The effect of inlet constriction on bubble growth during flow boiling in microchannels. *Int. J. Heat Mass Transf.* **52**, 5204–5212 (2009).

107. Zhuan, R. & Wang, W. Simulation of subcooled flow boiling in a micro-channel. *Int. J. Refrig.* **34**, 781–795 (2011).

108. Gedupudi, S., Zu, Y. Q., Karayiannis, T. G., Kenning, D. B. R. & Yan, Y. Y. Confined bubble growth during flow boiling in a mini/micro-channel of rectangular cross-section part I: Experiments and 1-D modelling. *Int. J. Therm. Sci.* **50**, 250–266 (2011).

109. Magnini, M., Pulvirenti, B. & Thome, J. R. Numerical investigation of hydrodynamics and heat transfer of elongated bubbles during flow boiling in a microchannel. *Int. J. Heat Mass Transf.* **59**, 451–471 (2013).

110. Magnini, M. & Thome, J. R. Computational Study of Saturated Flow Boiling Within a

Microchannel in the Slug Flow Regime. *J. Heat Transfer* **138**, 021502 (2015).

111. Kharangate, C. R. & Mudawar, I. Review of computational studies on boiling and condensation. *Int. J. Heat Mass Transf.* **108**, 1164–1196 (2017).

112. Gong, S. & Cheng, P. Lattice Boltzmann simulation of periodic bubble nucleation, growth and departure from a heated surface in pool boiling. *Int. J. Heat Mass Transf.* **64**, 122–132 (2013).

113. Gong, S. & Cheng, P. Lattice Boltzmann simulations for surface wettability effects in saturated pool boiling heat transfer. *Int. J. Heat Mass Transf.* **85**, 635–646 (2015).

114. Fang, W. Z., Chen, L., Kang, Q. J. & Tao, W. Q. Lattice Boltzmann modeling of pool boiling with large liquid-gas density ratio. *Int. J. Therm. Sci.* **114**, 172–183 (2017).

115. Gong, S. & Cheng, P. Numerical investigation of saturated flow boiling in microchannels by the lattice boltzmann method. *Numer. Heat Transf. Part A Appl.* **65**, 644–661 (2014).

116. Sun, T., Gui, N., Yang, X., Tu, J. & Jiang, S. Numerical study of patterns and influencing factors on flow boiling in vertical tubes by thermal LBM simulation. *Int. Commun. Heat Mass Transf.* **86**, 32–41 (2017).

117. Sun, T., Gui, N., Yang, X., Tu, J. & Jiang, S. Effect of contact angle on flow boiling in vertical ducts: A pseudo-potential MRT-thermal LB coupled study. *Int. J. Heat Mass Transf.* **121**, 1229–1233 (2018).

118. Zhang, C. *et al.* Lattice Boltzmann mesoscopic modeling of flow boiling heat transfer processes in a microchannel. *Appl. Therm. Eng.* **197**, 117369 (2021).

119. Basu, N., Warrier, G. R. & Dhir, V. K. Wall Heat Flux Partitioning During Subcooled Flow Boiling : Part 1 — Model Development. *J. Heat Transfer* **127**, 131–140 (2005).

120. Li, Y. & Ren, W. Numerical study of vapor condensation on patterned hydrophobic surfaces using the string method. *Langmuir* **30**, 9567–9576 (2014).

121. Lee, H., Kharangate, C. R., Mascarenhas, N., Park, I. & Mudawar, I. Experimental and computational investigation of vertical downflow condensation. *Int. J. Heat Mass Transf.* **85**, 865–879 (2015).

122. Da Riva, E. & Del Col, D. Effect of gravity during condensation of R134a in a circular

minichannel: VOF simulation of annular condensation. *Microgravity Sci. Technol.* **23**, 87–97 (2011).

123. Rose, J. W. Dropwise condensation theory and experiment: A review. *Proc. Inst. Mech. Eng. Part A J. Power Energy* **216**, 115–128 (2002).

124. Vemuri, S. & Kim, K. J. An experimental and theoretical study on the concept of dropwise condensation. *Int. J. Heat Mass Transf.* **49**, 649–657 (2006).

125. Park, K. C. *et al.* Nanotextured silica surfaces with robust superhydrophobicity and omnidirectional broadband supertransmissivity. *ACS Nano* **6**, 3789–3799 (2012).

126. Guo, P. *et al.* Icephobic/anti-icing properties of micro/nanostructured surfaces. *Adv. Mater.* **24**, 2642–2648 (2012).

127. Lee, S. *et al.* Heat transfer measurement during dropwise condensation using micro/nano-scale porous surface. *Int. J. Heat Mass Transf.* **65**, 619–626 (2013).

128. Ghosh, A., Beaini, S., Zhang, B. J., Ganguly, R. & Megaridis, C. M. Enhancing dropwise condensation through bioinspired wettability patterning. *Langmuir* **30**, 13103–13115 (2014).

129. Quéré, D. Wetting and roughness. *Annu. Rev. Mater. Res.* **38**, 71–99 (2008).

130. Zhang, Q., Sun, D., Zhang, Y. & Zhu, M. Lattice Boltzmann modeling of droplet condensation on superhydrophobic nanoarrays. *Langmuir* **30**, 12559–12569 (2014).

131. Jung, Y. C. & Bhushan, B. Wetting behaviour during evaporation and condensation of water.pdf. *J. Microsc.* **229**, 127–140 (2008).

132. Shin, B., Lee, K. R., Moon, M. W. & Kim, H. Y. Extreme water repellency of nanostructured low-surface-energy non-woven fabrics. *Soft Matter* **8**, 1817–1823 (2012).

133. Starostin, A. *et al.* Drop-wise and film-wise water condensation processes occurring on metallic micro-scaled surfaces. *Appl. Surf. Sci.* **444**, 604–609 (2018).

134. Boreyko, J. B. & Chen, C. H. Restoring superhydrophobicity of lotus leaves with vibration-induced dewetting. *Phys. Rev. Lett.* **103**, 1–4 (2009).

135. Narhe, R. D. & Beysens, D. A. Growth dynamics of water drops on a square-pattern rough

hydrophobic surface. *Langmuir* **23**, 6486–6489 (2007).

136. Liu, X. & Cheng, P. Lattice Boltzmann simulation of steady laminar film condensation on a vertical hydrophilic subcooled flat plate. *Int. J. Heat Mass Transf.* **62**, 507–514 (2013).

137. Li, X., Zhao, J. & Cheng, P. A lattice Boltzmann model for condensation and freezing of dry saturated vapor about a cryogenic spot on an inclined hydrophobic surface. *Int. J. Heat Mass Transf.* **114**, 628–639 (2017).

138. Li, X. & Cheng, P. Lattice Boltzmann simulations for transition from dropwise to filmwise condensation on hydrophobic surfaces with hydrophilic spots. *Int. J. Heat Mass Transf.* **110**, 710–722 (2017).

139. Zheng, S., Eimann, F., Fieback, T., Xie, G. & Gross, U. Numerical investigation of convective dropwise condensation flow by a hybrid thermal lattice Boltzmann method. *Appl. Therm. Eng.* **145**, 590–602 (2018).

140. Fu, X., Yao, Z. & Hao, P. Numerical simulation of condensation on structured surfaces. *Langmuir* **30**, 14048–14055 (2014).

141. Vasyliv, Y. *et al*. Modeling condensation on structured surfaces using lattice Boltzmann method. *Int. J. Heat Mass Transf.* **136**, 196–212 (2019).

142. Li, M., Huber, C., Tao, W. & Wei, J. Study on nucleation position and wetting state for dropwise condensation on rough structures with different wettability using multiphase lattice Boltzmann method. *Int. J. Heat Mass Transf.* **131**, 96–100 (2019).

143. Sikarwar, B. S., Muralidhar, K. & Khandekar, S. Effect of Drop Shape on Heat Transfer During Dropwise Condensation Underneath Inclined Surfaces. *Interfacial Phenom. Heat Transf.* **1**, 339–356 (2013).

144. Dong, J., Jin, Y., Dong, H., Liu, J. & Ye, S. Numerical Study for a Large-Volume Droplet on the Dual-Rough Surface: Apparent Contact Angle, Contact Angle Hysteresis, and Transition Barrier. *Langmuir* **34**, 8119–8127 (2018).

145. Yang, J., Chen, J. C., Huang, K., Yeh, J. A. & Angle, A. C. Droplet Manipulation on a Hydrophobic Textured Surface With Roughened Patterns. *IEEE Explor.* **15**, 697–707 (2006).

146. Lee, H., Kharangate, C. R., Mascarenhas, N., Park, I. & Mudawar, I. International Journal of Heat and Mass Transfer Experimental and computational investigation of vertical downflow condensation. *HEAT MASS Transf.* **85**, 865–879 (2015).

147. Guo, Q. & Cheng, P. 3D lattice Boltzmann investigation of nucleation sites and dropwise-to-filmwise transition in the presence of a non-condensable gas on a biomimetic surface. *Int. J. Heat Mass Transf.* **128**, 185–198 (2019).

148. Vasyliv, Y. *et al.* International Journal of Heat and Mass Transfer Modeling condensation on structured surfaces using lattice Boltzmann method. *Int. J. Heat Mass Transf.* **136**, 196–212 (2019).

149. Nukiyama, S. Memories of my reasearch on boiling. *Int. J. Heat Mass Transf.* **27**, 955–957 (1986).

150. Kim, J. Review of nucleate pool boiling bubble heat transfer mechanisms. *Int. J. Multiph. Flow* **35**, 1067–1076 (2009).

151. Dhir, V. K., Warrier, G. R. & Atkinol, E. Numerical Simulation of Pool Boiling: A Review. *J. Heat Transfer* **135**, 061502 (2013).

152. Sun, D. L. & Tao, W. Q. A coupled volume-of-fluid and level set (VOSET) method for computing incompressible two-phase flows. *Int. J. Heat Mass Transf.* **53**, 645–655 (2010).

153. Pandey, V., Biswas, G., Dalal, A. & Welch, S. W. J. Bubble Lifecycle During Heterogeneous Nucleate Boiling. *J. Heat Transfer* **140**, 121503 (2018).

154. Ma, X., Cheng, P., Gong, S. & Quan, X. Mesoscale simulations of saturated pool boiling heat transfer under microgravity conditions. *Int. J. Heat Mass Transf.* **114**, 453–457 (2017).

155. Li, Q., Yu, Y., Zhou, P. & Yan, H. J. Enhancement of boiling heat transfer using hydrophilic-hydrophobic mixed surfaces: A lattice Boltzmann study. *Appl. Therm. Eng.* **132**, 490–499 (2018).

156. Chang, X., Huang, H., Cheng, Y. P. & Lu, X. Y. Lattice Boltzmann study of pool boiling heat transfer enhancement on structured surfaces. *Int. J. Heat Mass Transf.* **139**, 588–599 (2019).

157. Li, W. X., Li, Q., Yu, Y. & Wen, Z. X. Enhancement of nucleate boiling by combining the effects of surface structure and mixed wettability: A lattice Boltzmann study. *Appl. Therm. Eng.* **180**, 1–

11 (2020).

158. Shan, X. & Chen, H. Simulation of nonideal gases and liquid-gas phase transitions by the lattice Boltzmann equation. *Phys. Rev. E* **49**, 2941–2948 (1994).

159. Guo, Z., Zheng, C. & Shi, B. Discrete lattice effects on the forcing term in the lattice Boltzmann method. *Phys. Rev. E - Stat. Physics, Plasmas, Fluids, Relat. Interdiscip. Top.* **65**, 6 (2002).

160. Benzi, R., Biferale, L., Sbragaglia, M., Succi, S. & Toschi, F. Mesoscopic modeling of a two-phase flow in the presence of boundaries: The contact angle. *Phys. Rev. E - Stat. Nonlinear, Soft Matter Phys.* **74**, 1–14 (2006).

161. Kang, Q., Zhang, D. & Chen, S. Displacement of a two-dimensional immiscible droplet in a channel. *Phys. Fluids* **14**, 3203–3214 (2002).

162. Shan, X. Analysis and reduction of the spurious current in a class of multiphase lattice Boltzmann models. *Phys. Rev. E* **73**, 047701 (2006).

163. Kuzmin, A., Mohammad, A. A. & Succi, S. Multi-Relaxation Time Lattice Boltzmann Model for Multiphase Flows. *Int. J. Mod. Phys. C* **19**, 875–902 (2008).

164. Zou, Q. & He, X. On pressure and velocity flow boundary conditions and bounceback for the lattice Boltzmann BGK model. *Phys. Fluids* **9**, 1591–1598 (1997).

165. Du, J., Zhao, C. & Bo, H. Investigation of bubble departure diameter in horizontal and vertical subcooled flow boiling. *Int. J. Heat Mass Transf.* **127**, 796–805 (2018).

166. Sun, T., Li, W. & Yang, S. Numerical simulation of bubble growth and departure during flow boiling period by lattice Boltzmann method. *Int. J. Heat Fluid Flow* **44**, 120–129 (2013).

167. Yoo, J., Estrada-Perez, C. E. & Hassan, Y. A. Experimental study on bubble dynamics and wall heat transfer arising from a single nucleation site at subcooled flow boiling conditions – Part 2: Data analysis on sliding bubble characteristics and associated wall heat transfer. *Int. J. Multiph. Flow* **84**, 292–314 (2016).

168. Yoo, J., Estrada-Perez, C. E. & Hassan, Y. A. Experimental study on bubble dynamics and wall heat transfer arising from a single nucleation site at subcooled flow boiling conditions – Part 1: Experimental methods and data quality verification. *Int. J. Multiph. Flow* **84**, 315–324 (2016).

169. Edel, Z. J. & Mukherjee, A. Experimental investigation of vapor bubble growth during flow boiling in a microchannel. *Int. J. Multiph. Flow* **37**, 1257–1265 (2011).

170. Harirchian, T. & Garimella, S. V. Effects of channel dimension, heat flux, and mass flux on flow boiling regimes in microchannels. *Int. J. Multiph. Flow* **35**, 349–362 (2009).

171. Mukherjee, A., Kandlikar, S. G. & Edel, Z. J. International Journal of Heat and Mass Transfer Numerical study of bubble growth and wall heat transfer during flow boiling in a microchannel. *Int. J. Heat Mass Transf.* **54**, 3702–3718 (2011).

172. Lv, C., Hao, P., Zhang, X. & He, F. Dewetting Transitions of Dropwise Condensation on Nanotexture- Enhanced Superhydrophobic Surfaces. 12311–12319 (2015).

173. Aili, A. How Nanostructures Affect Water Droplet Nucleation on Superhydrophobic Surfaces. **139**, 1–10 (2017).

174. David, R. & Neumann, A. W. Colloids and Surfaces A : Physicochemical and Engineering Aspects Energy barriers between the Cassie and Wenzel states on random , superhydrophobic surfaces. *Colloids Surfaces A Physicochem. Eng. Asp.* **425**, 51–58 (2013).

175. Wu, Y., Yang, C. & Yuan, X. Drop distributions and numerical simulation of dropwise condensation heat transfer. **44**, 4455–4464 (2001).

176. Garg, D. & Dhir, V. K. A unified three-dimensional numerical model for boiling curve in a temperature controlled mode. *J. Heat Transfer* **141**, 011504 (2019).

177. Wagner, E. & Stephan, P. High-resolution measurements at nucleate boiling of pure FC-84 and FC-3284 and its binary mixtures. *J. Heat Transfer* **131**, 1–12 (2009).

178. Wei, J. J., Guo, L. J. & Honda, H. Experimental study of boiling phenomena and heat transfer performances of FC-72 over micro-pin-finned silicon chips. *Heat Mass Transf. und Stoffuebertragung* **41**, 744–755 (2005).

179. Cooke, D. & Kandlikar, S. G. Pool boiling heat transfer and bubble dynamics over plain and enhanced microchannels. *J. Heat Transfer* **133**, 052902 (2011).

180. Chu, K. H., Enright, R. & Wang, E. N. Structured surfaces for enhanced pool boiling heat transfer. *Appl. Phys. Lett.* **100**, 241603 (2012).

181. Mu, Y. T., Chen, L., He, Y. L., Kang, Q. J. & Tao, W. Q. Nucleate boiling performance evaluation of cavities at mesoscale level. *Int. J. Heat Mass Transf.* **106**, 708–719 (2017).

182. Kandlikar, S. G. A theoretical model to predict pool boiling CHF incorporating effects of contact angle and orientation. *J. Heat Transfer* **123**, 1071–1079 (2001).

183. Takata, Y. *et al.* Effect of surface wettability on boiling and evaporation. *Energy* **30**, 209–220 (2005).

184. Chen, R. *et al.* Nanowires for enhanced boiling heat transfer. *Nano Lett.* **9**, 548–553 (2009).

Publications

International Journals

- A. Mukherjee, D.N. Basu, P. K. Mondal, Algorithmic augmentation in the pseudopotential-based lattice Boltzmann method for simulating the pool boiling phenomenon with high-density ratio, *Physical Review E*, 103(5), 053302 (2021).
- A. Mukherjee, D.N. Basu, P. K. Mondal, Mesoscopic characterization of bubble dynamics in subcooled flow boiling following a pseudopotential-based approach, *International Journal of Multiphase Flow*, 148. 103923, (2022).
- A. Mukherjee, D.N. Basu, P. K. Mondal, L. Chen, Characterization of condensation on nano-structured surfaces and associated thermalhydraulics using thermal lattice Boltzmann method, *Physical Review E*, 105(4), 045308 (2022).
- A. Mukherjee, D.N. Basu, P. K. Mondal, Numerical simulation of condensate droplet movement under the effect of gravity on microstructured rough inclined surfaces using lattice Boltzmann method *(under preparation)*

International Conferences

- A. Mukherjee, D. N. Basu, P. K. Mondal; Lattice Boltzmann simulation of periodic bubble nucleation, growth and departure in nucleate pool boiling, *26th National and 3rd International ISHMT-ASTFE Heat and Mass Transfer Conference*, Roorkee, India, December 28-31, 2019.
- A. Mukherjee, D. N. Basu, P. K. Mondal; Numerical investigation of the effect of surface topology on droplet condensation following lattice Boltzmann methods, *8th International and 47th National Conference on Fluid Mechanics and Fluid Power*, December 2020.